A Study of the Tropospheric Oxidation of Volatile Organic Compounds Using Chemical Ionization Mass Spectrometry

by

Keith Edward Broekhuizen

B.S. Chemistry
Calvin College, 1996

Submitted to the Department of Chemistry
in partial fulfillment of the requirements for the degree of

Doctor of Philosophy in Chemistry

at the

MASSACHUSETTS INSTITUTE OF TECHNOLOGY

February, 2002

Signature of Author .....
Department of Chemistry
20 December 2001

Certified by .....
Mario J. Molina
Institute Professor
Thesis Supervisor

Accepted by .....
Robert W. Field
Chairperson, Department Committee on Graduate Students

This doctoral thesis has been examined by a committee of the Department of Chemistry as follows:

Professor Bruce Tidor .....

Chairman

Professor Mario J. Molina .....

Thesis Advisor

Professor Jeffrey I. Steinfeld .....

Department of Chemistry

A Study of the Tropospheric Oxidation of Volatile Organic Compounds Using Chemical Ionization Mass Spectrometry

by

Keith Edward Broekhuizen

Submitted to the Department of Chemistry
on 20 December 2001, in partial fulfillment of the
requirements for the degree of
Doctor of Philosophy in Chemistry

Abstract

The mechanisms and kinetics of reactions important to the troposphere have been investigated using a high pressure, turbulent, discharge-flow technique coupled to a chemical ionization mass spectrometer. The ability to accurately model tropospheric chemistry depends on kinetic and mechanistic information for a wide variety of species.

The gas-phase chemistry of the troposphere is dominated by the oxidation of trace species such as methane. One important intermediate in the oxidation of methane is the methylperoxy radical (CH_3O_2). The kinetic rate coefficient of the reaction of CH_3O_2 with NO was measured at 298 K and 100 Torr. The kinetics of the reaction of CH_3O_2 with HO_2 were then examined.

Aromatics are another important class of trace species found in the troposphere. The daytime oxidation of toluene is initiated by reaction with the OH radical. Rate coefficients and detailed mechanistic information for this oxidation pathway are poorly understood. The kinetics of the reaction of toluene with OH were measured at 298 K and 100 Torr. The detection of radical intermediates in this pathway was also accomplished using CIMS.

Biogenic hydrocarbons also have complex oxidation mechanisms which are poorly understood. Many of these compounds are cyclic alkenes or dienes with complicated oxidation mechanisms. Propylene (C_3H_6) is a very simple alkene and can be studied as a proxy to larger biogenic compounds. The rate coefficient for the reaction of propylene with OH was measured at 100 Torr for a range of temperatures (235-305 K). The rate coefficient for the reaction of the hydroxy-propylperoxy radical ($CH_3CH(OO)CH_2OH$) with NO was also measured at 100 Torr for a range of temperatures (235-305 K).

This technique was also extended to the study of the important reaction of NO with the β- or δ-hydroxy-peroxy radical formed in the oxidation of isoprene ($C_5H_8OHO_2$) at 100 Torr and 298 K.

Thesis Supervisor: Mario J. Molina
Title: Institute Professor

Contents

List of Figures

Acknowledgements

"*Therefore, since we are surrounded by so great a cloud of witnesses, let us also lay aside every weight and sin which clings so closely, and let us run with perseverance the race the race that is set before us, looking to Jesus, the pioneer and perfecter of our faith, who for the joy that was set before him endured the cross, despising the shame, and is seated at the right hand of the throne of God.*"

Hebrews 12:1-2

To God, the giver of all great gifts.

It is difficult to thank everyone who has helped me through these last five years or had an impact on who I am, but I will give it my best shot. Forgive me if I don't remember everyone.

To my parents, for the years of teaching, encouragement and love which gave me the courage and the ability to follow my dreams. I hope I can be the example to others that you were to me. Mom, despite what others in the family may think, thanks for your analytical mind. Dad, you showed me that being a teacher is a very good thing, and for that I thank you (but sixth graders??) Dan and Eric, thanks for being two great brothers all these years. 3-2-1 and wiffleball in the backyard will always stay with me. Thanks for pushing me and supporting me. I'm proud of you guys, and Eric, at least you get to touch the banner. I love all of you and I couldn't have asked for a better family.

To Mario, thanks for giving me a chance. It was a great experience working in your lab. I learned many things, but foremost that I have only really scratched the surface. Thanks for giving me the freedom to explore and take the research in a direction that interested me while giving me guidance and prodding when I needed it.

There are a number of people who are responsible for my desire to be a scientist and I thank them (although I admit there were times when I wanted to curse them). Ed Bosch, a man of seemingly limitless energy, who really set me on this road. Mark and Karen Muyskens, my mentors at Calvin, who taught me what research was all about and strengthened my desire to follow this through.

This work would have been impossible without the support of others in the lab. Geoff and Jen, thanks for teaching me the ropes, giving me a hard time, fantasy baseball, Siedler

(or Sieldlah), help when I needed it, and friendship when I needed it. You guys have been my greatest help and allies in the lab. Len Newton, "the man", I will miss coming into your office and asking you for stuff. Let's be honest, I would have spent most of my time standing next to a pile of rubble if it wasn't for Lenny. My ability to break things and his ability to fix them meshed well. Franz and Al, thanks for the advice, the discussions about science and life, the pints and the grace to accept the foosball humiliation you endured at my hands. Thomas Koop and Manjula, I really enjoyed working with you and wish you the best. Thanks to those who have put up with me in the last days, especially Faye and Matt. Good luck and I will miss you both. There are too many others to name, but I would like to thank Steph and Don for their friendship and giving me access to the Prinn group resources, Martin, Christophe, Rafael, Carl, Danna, Luisa, and everyone I've forgotten for their help and support.

One of my greatest joys was my life outside the lab and I have many people to thank for that. Brad and Julie, thanks for taking us under your wing when we were new in town and showing us the ropes. You guys have been great. Jim and Suze, it was great to have a kindred spirit at "the Institute". Stay strong and don't succumb to the NPC disease (I mean the Atticus, Katie, etc. disease). Hope and Jay, Andy, Doris, Bruce, Beth, Fred and Lenore and all the other NPCYAers, we enjoyed getting to know you and will miss you terribly. Our time together was too short. Wherever we end up, our door is always open to you all.

Finally, to my wife Joanne, what can I say. It is difficult to express what you have meant to me over the last nine years. You have been there for me through it all, the highs, the lows, the joy and the sorrow. You have shown patience, love, anger, and encouragement blended in just the right proportions at just the right times. You love me more than I deserve and have been my best friend and toughest critic, both of which I have needed. I promise that this I will catch up on my share of the dishes and laundry, although it may take a few years for me to do it. I love you more each day and dedicate this work to you since it is as much your labor of love as it is mine. We did it (finally).

"*I have fought the good fight, I have finished the race, I have kept the faith*"

II Timothy 4:7

Chapter 1

Introduction

1.1 Motivation for Research

The chemistry of the atmosphere is governed mainly by the reactions of a set of trace gas species. While the absolute concentrations of the species may be small, ranging from a few percent in the case of water vapor to hundredths of a part per trillion for the hydroxyl radical, the impact of these species on the atmosphere is profound. The removal processes of many species in the atmosphere are initiated by reaction with the hydroxyl radical, followed by subsequent oxidation reactions. These oxidation processes are important for many atmospheric phenomena such as photochemical smog and particle formation. The mechanisms for the conversion of many inorganic species such as SO_2 and NO_2 to H_2SO_4 and HNO_3 are well understood, however the detailed oxidation mechanisms for most organic molecules remain poorly characterized [*Finlayson-Pitts & Pitts*, 2001].

1.1.1 Methane oxidation

Methane is the most abundant hydrocarbon in the atmosphere. The relatively unreactive nature of methane towards OH ($k_{1.1(OH)} = 6.3 \times 10^{-15}$ cm^3 molecule^{-1} s^{-1}) [*DeMore et al.*, 1997] gives it a lifetime of years in the atmosphere. Removal of CH_4 by OH occurs on a longer timescale than normal mixing times, allowing methane to become well mixed in the troposphere with a global mean concentration of about 1700 ppb [*Finlayson-Pitts & Pitts*, 2001]. Methane is also important to the chemistry of the stratosphere, where it converts active chlorine into

the reservoir species, HCl. Due to its abundance and importance in the atmosphere, the fate of methane has been studied to a greater extent than any other hydrocarbon to date. Most of the gas-phase reaction rates of the oxidation mechanism of methane are known over a range of temperatures and pressures. The reaction is generally initiated by the hydroxyl radical, OH, or the chlorine atom, Cl:

$$CH_4 + OH/Cl \longrightarrow CH_3 + H_2O/HCl \tag{1.1}$$

$$CH_3 + O_2 \xrightarrow{M} CH_3O_2 \tag{1.2}$$

The fate of the methyl radical, CH_3, is reaction with oxygen, despite the relatively slow rate of reaction ($k_{1.2\,(\infty)} = 1.8 \times 10^{-12}$ cm^3 molecule^{-1} s^{-1}) [*DeMore et al.*, 1997]. The methylperoxy radical, CH_3O_2, may enter a number of different reaction channels, depending on the ambient NO_x concentration [*Tyndall et al.*, 2001]. In polluted air, or conditions of high NO_x concentrations, CH_3O_2 will undergo the following reactions [*Scholtens et al.*, 1999]:

$$CH_3O_2 + NO \longrightarrow CH_3O + NO_2 \tag{1.3}$$

$$\xrightarrow{M} CH_3ONO_2 \tag{1.4}$$

$$CH_3O + O_2 \longrightarrow HCHO + HO_2 \tag{1.5}$$

In this way methane is converted to formaldehyde, which may photodissociate or react further with HO_x [*Wayne*, 1994]. This pathway also converts NO to NO_2, leading to formation of ozone through the reactions:

$$HO_2 + NO \longrightarrow OH + NO_2 \tag{1.6}$$

$$NO_2 \xrightarrow{h\nu} NO + O(^3P) \tag{1.7}$$

$$O(^3P) + O_2 \xrightarrow{M} O_3 \tag{1.8}$$

Under more pristine conditions, such as in the marine boundary layer where NO_x concentrations are low, CH_3O_2 may undergo reactions with the HO_2 radical [*McAdam et al.*, 1987]

$$CH_3O_2 + HO_2 \longrightarrow CH_3OOH + O_2 \quad (1.9)$$

$$\longrightarrow HCHO + H_2O + O_2 \quad (1.10)$$

or other peroxy radicals [*Cox & Tyndall*, 1979]:

$$CH_3O_2 + CH_3O_2 \longrightarrow CH_3OH + HCHO + O_2 \quad (1.11)$$

$$\longrightarrow 2CH_3O + O_2 \quad (1.12)$$

$$\longrightarrow (CH_3O)_2 + O_2 \quad (1.13)$$

$$CH_3O_2 + RO_2 \longrightarrow Products \quad (1.14)$$

These elementary steps in the atmospheric oxidation of methane have been studied extensively, but there are several important questions remaining. The rate of formation of formaldehyde by reaction 1.10 is not well established, although there have been recent studies investigating this branching ratio [*Elrod et al.*, 2001]. The rate of reaction 1.9 is also uncertain due to discrepancies in the measured ultraviolet absorption cross-sections of HO_2 and CH_3O_2 [*Tyndall et al.*, 2001]. These discrepancies in the cross-sections result in uncertainties in the absolute concentrations of the peroxy radicals and subsequent uncertainty in the reaction rates.

1.1.2 Photochemical smog

The abundance of hydrocarbons and NO_x in urban air masses leads to the production of photochemical smog. Photochemical smog is characterized by high levels of oxidants such as ozone, peroxyacetylnitrate (PAN), nitric acid, and particulate matter [*Finlayson-Pitts & Pitts*, 2001]. These oxidants and particulate matter have many unwanted effects such as increased incidence of asthma, plant damage, and lung damage [*Teague & Bayer*, 2001]. The formation mechanisms of photochemical smog are complex and only generally understood. The formation mechanism

of ozone is described in the previous section on methane oxidation. In general, VOC oxidation mechanisms involve the conversion of NO to NO_2, followed by photolysis of NO_2 and formation of ozone. PAN ($CH_3C(O)OONO_2$ is formed in the oxidation of C_2 or higher hydrocarbons, such as acetaldehyde formed in the oxidation of ethane:

$$CH_3CHO + OH \longrightarrow CH_3CO + H_2O \tag{1.15}$$

$$CH_3CO + O_2 \xrightarrow{M} CH_3C(O)OO \tag{1.16}$$

$$CH_3C(O)OO + NO_2 \xrightarrow{M} CH_3C(O)OONO_2 \tag{1.17}$$

Detailed information on reaction rates and product distributions for most volatile organic compounds (VOC) is limited. Only for the most simple hydrocarbons, such as methane and ethane, are detailed mechanisms well known [*Atkinson*, 1994].

Important species of VOCs found in urban air masses are aromatic compounds such and benzene, toluene, and other more highly substituted benzenes. These compounds are found in concentrations reaching 100 ppb. The chemistry of these compounds is important due to their ability to form low volatility products upon oxidation. This oxidation leads to particle formation either by nucleation or by condensation on existing particles [*Hurley et al.*, 2001]. Many of these nitrated and oxidized products are also highly toxic or carcinogenic [*Tokiwa et al.*, 1998]. To date, the bulk of the studies on aromatic oxidation have been done in smog chamber experiments which have identified many products but have yet to achieve a carbon balance. Intermediate species have also been identified in only a few experiments [*Atkinson*, 1994].

1.1.3 Biogenic VOCs

Biogenic hydrocarbons account for up to 90% of the total global VOC emissions and these biogenic emissions can approach 1150 Tg/yr [*Guenther et al.*, 1995]. Although anthropogenic VOCs still dominate the chemistry of urban areas, biogenic VOCs are very important to the chemistry of more remote regions and can play a significant role in the chemistry of the urban

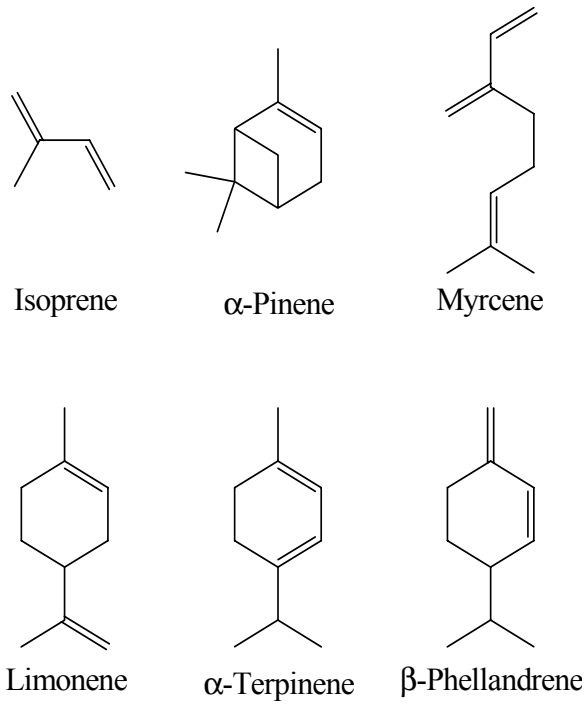

Figure 1-1: Chemical structures of some biogenically emitted hydrocarbons.

air shed as well [*Finlayson-Pitts & Pitts*, 2001]. The reaction rates of many biogenic VOCs with the hydroxyl radical are very fast ($10^{-11} \leq k \leq 10^{-10}$ cm^3 molecule^{-1} s^{-1}) [*Atkinson*, 1994], so that the atmospheric lifetimes are less than a day under most conditions. Figure 1-1 gives some examples of biogenic VOCs which have been observed in the atmosphere.

The state of knowledge with respect to biogenic VOCs is similar to that of aromatic VOCs. There is little known beyond the rate of the reactions with OH, NO_3, O_3, or Cl for most of these compounds. Most intermediate species have not been identified and only a limited number of final products have been identified. There have been some recent studies of isoprene which investigate reactions of the intermediates in the isoprene oxidation mechanism [*Zhang et al.*, 2001].

1.2 Experimental Techniques

1.2.1 Chemical ionization mass spectrometry

The technique of chemical ionization mass spectrometry (CIMS) was used for all the experiments described in this thesis. The basis for chemical ionization is not electron bombardment or laser based ionization techniques which are commonly used, but rather reactions between a parent ion and the neutral species of interest. Equation 1.18 is an example of a simple negative-ion charge transfer reaction from the parent ion, X^-, to the molecule of interest, M.

$$X^- + M \longrightarrow X + M^- \tag{1.18}$$

Chemical ionization has been used extensively in our group and has been well established in the literature [*Smith et al.*, 2000; *Lipson et al.*, 1999]. The ions are generated in these experiments by two methods, namely corona discharge and α-particle bombardment from a ^{210}Po source. A wide variety of both positive and negative parent ions were used (e.g. SF_6^-, F^-, O_2^-, O_2^+, and H_3O^+). Each parent ion has a particular set of species with which it reacts efficiently. Potential advantages of chemical ionization over other types of ionization include enhanced selectivity, sensitivity, and lack of fragmentation of the product ions. These advantages are necessary for the experiments for a variety of reasons. The lack of fragmentation traditionally prevalent with techniques such as electron impact ionization is especially important when working with organic molecules which can have complex and overlapping fragmentation patterns. The selectivity of the technique allows one to tailor the chemical ionization scheme to detect only reactants and products of interest, and the enhanced sensitivity was crucial for the detection of small concentrations of highly reactive organic radical intermediates [*Harrison*, 1992].

1.2.2 Flow-tube techniques

The reactions of interest were carried out in a discharge-flow system operating under turbulent flow, high pressure conditions. This flow system was coupled to the CIMS detection scheme described above. A detailed description of the turbulent flow technique has been described

previously [*Seeley*, 1994]. Briefly, the onset of turbulent flow conditions occurs when the Reynolds number describing the flow (Equation 1.19) becomes larger than 3000. The Reynolds number is defined as:

$$R_e = \frac{2a\overline{u}\rho}{\mu} \tag{1.19}$$

where a is the internal radius of the flow tube, $\bar{u}$ is the average flow velocity, ρ is the density of the gas, and μ is the gas viscosity. Turbulent flow conditions are characterized by a relatively flat velocity profile that allows the plug flow approximation to be used. This approximation greatly simplifies the calculation of reaction times. The laminar sublayer which forms at the wall inhibits diffusion to the walls and therefore reduces wall effects, allowing experiments to be conducted at low temperatures inaccessible under laminar flow conditions. A microwave discharge cavity operating at a frequency of 2.45 GHz was used to produce radical species used in the experiments.

1.3 Thesis Outline

The goal of the research presented in this thesis was the development of an experimental technique capable of both producing and detecting organic radical intermediates and stable products important to atmospheric oxidation processes. This work involved the development of methods for producing reactive organic intermediates with the discharge-flow technique and also developing a CIMS methodology capable of detecting these transient species with high sensitivities.

The second chapter of this thesis describes improvement of a commercially available UTI 100C residual gas analyzer. The instrument was modified from an electron impact instrument capable of detecting only positive ions to a chemical ionization instrument capable of detecting both positive and negative ions. Hardware modifications were required to complete this conversion. The sensitivity of this instrument was measured for a variety of gases and compared to other instruments in use in the laboratory.

Chapter 3 describes the initial experiments performed on the UTI 100C. The well known rate coefficient of the CH_3O_2 + NO reaction ($k_{1.3} = 7.7 \times 10^{-12}$ cm^3 molecule^{-1} s^{-1}) [*DeMore et al.*, 1997] was measured to establish the ability of the system to perform these measurements. A measurement of the rate coefficient of the CH_3O_2 + HO_2 was attempted using the UTI

100C CIMS system. This rate coefficient has large uncertainties due to difficulties in the measurements of the absolute concentrations of the reactants [*Tyndall et al.*, 2001]. This reaction proved inaccessible due to complications in the production of large concentrations of the reactants.

Chapter 4 details the experiments performed on aromatic molecules of interest, specifically toluene. The kinetics of the reaction of toluene with OH have been well established [*Atkinson*, 1994], but were verified using the CIMS technique. The focus of this study was on the OH addition pathway, which accounts for ∼90% of the total reaction. The initial product of the addition reaction, the methyl-hydroxycyclohexadienyl radical, was detected using CIMS, and the reactions of this adduct were explored.

The fifth chapter concerns the initial experiments in the study of the reactions of biogenic VOCs. Toluene proved to be a complicated system to study using the CIMS-flow tube methodology, so the initial step in the study of biogenic VOCs was the study of a simple alkene, propylene. Propylene is one of the smallest alkenes and can be used as a model for the study of more complex biogenic VOCs such as isoprene or α-pinene. The reaction of propylene with OH was studied at 100 Torr and temperatures representative of the troposphere (238-311 K). No previous studies of this reaction have been conducted in this temperature range. The reaction of the product of the propene + OH reaction, the hydroxy-propylperoxy radical, with NO was also studied in this same temperature and pressure regime. This is the first direct study to date of this reaction. Mass balance experiments were also performed to validate previous work [*Niki et al.*, 1978] which suggested that the major products of propylene oxidation in the troposphere are acetaldehyde and formaldehyde.

Chapter 6 details the extension of the techniques employed on the propylene system to a more complicated biogenic VOC, isoprene. Isoprene has been studied rigorously by a variety of groups [*Zhang et al.*, 2001; *Atkinson*, 1994], although much of the oxidation mechanism has not been directly studied. The reaction of the hydroxy-isoprylperoxy radical with NO was studied at 100 Torr and 298 K. This also represents the first direct study of this reaction.

References for Chapter 1

Atkinson, R., Gas-phase tropospheric chemistry of organic compounds, *Journal of Physical and Chemical Reference Data Monograph No. 2*, 1994.

Cox, R.A. and G.S. Tyndall, Rate constants for reactions of CH_3O_2 in the gas phase, *Chem. Phys. Lett.*, **65**, 357-360, 1979.

DeMore, W.B., S.P. Sander, C.J. Howard, A.R. Ravishankara, D.M. Golden, C.E. Kolb, R.F. Hampson, M.J. Kurylo, and M.J. Molina, *Chemical Kinetics and Photochemical Data for Use in Stratospheric Modeling*, JPL Publication 97-4, Jet Propulsion Laboratory, Pasadena, CA, 1997.

Elrod, M.J., D.L. Ranschaert, and N.J. Schneider, Direct kinetics study of the temperature dependence of the CH_2O branching channel for the $CH_3O_2 + HO_2$ reaction, *Int. J. Chem. Kinet.*, **33**, 363-376, 2001.

Finlayson-Pitts, B.J. and J.N. Pitts, Jr., *Chemistry of the Upper and Lower Atmosphere*, Academic Press, San Diego, 2000, pp. 4-8, 182-216, 225, 777.

Guenther, A., C.N. Hewitt, D. Erickson, R. Fall, C. Geron, T. Graedel, P. Harley, L. Klinger, M. Lerdau, W.A. McKay, T. Pierce, B. Scholes, R. Steinbrecher, R. Tallamraju, J. Taylor, and P. Zimmerman, A global model of natural volatile organic compound emissions, *J. Geophys. Res.*, **100**, 8873-8892, 1995.

Harrison, A.G., *Chemical Ionization Mass Spectrometry*, CRC Press, Boca Raton, 1992, pp. 82-84.

Hurley, M.D., O. Sokolov, T.J. Wallington, H. Takekawa, M. Karasawa, B. Klotz, I. Barnes, and K.H. Becker, Organic aerosol formation during the atmospheric degradation of toluene, *Environ. Sci. Technol.*, **35**, 1358-1366, 2001.

Lipson, J.B., T.W. Beiderhase, L.T. Molina, M.J. Molina, and M. Olzmann, Production of HCl in the OH plus ClO reaction: laboratory measurements and statistical rate theory calculations, *J. Phys. Chem. A*, **103**, 6540-6551, 1999.

McAdam, K., B. Veyret, and R.Lesclaux, UV absorption spectra of HO_2 and CH_3O_2 radicals and the kinetics of their mutual reactions at 298 K, *Chem. Phys. Lett.*, **133**, 39-44, 1987.

Niki, H., P.D. Maker, C.M. Savage, and L.P. Breitenbach, Mechanism for hydroxyl radical initiated oxidation of olefin-nitric oxide mixtures in parts per million concentrations, *J. Phys. Chem.*, **82**, 135-137, 1978.

Scholtens, K.W., B.M. Messer, C.D. Cappa, and M.J. Elrod, Kinetics of the $CH_3O_2 + NO$ reaction: temperature dependence of the overall rate constant and an improved upper limit for the CH_3ONO_2 branching channel, *J. Phys. Chem. A*, **103**, 4378-4384, 1999.

Seeley, J.V., *Experimental Studies of Gas Phase Reactions Using the Turbulent Flow Tube Technique*, Ph.D. Thesis, Massachusetts Institute of Technology, 1994.

Smith, G.D., L.T. Molina, and M.J. Molina, Temperature dependence of $O(^1D)$ quantum yields from the photolysis of ozone between 295 and 338 nm, *J. Phys. Chem. A*, **104**, 8916-8921, 2001.

Teague, W.G. and C.W. Bayer, Outdoor air pollution - asthma and other concerns, *Pediatric Clinics of North America*, **48**, 1167, 2001.

Tokiwa, H., Y. Nakanishi, N. Sera, N. Hara, and S. Inuzuka, Analysis of environmental carcinogens associated with the incidence of lung cancer, *Toxicol. Lett.*, **99**, 33-41, 1998.

Tyndall, G.S., R.A. Cox, C. Granier, R. Lesclaux, G.K. Moortgat, M.J. Pilling, A.R. Ravishankara, and T.J. Wallington, Atmospheric chemistry of small organic peroxy radicals, *J. Geophys. Res.*, **106**, 12157-12182, 2001.

Wayne, R.P., *Chemistry of Atmospheres*, Oxford University Press, Oxford, 1994, pp. 215-6.

Zhang, D., R.Y. Zhang, C. Church, and S.W. North, Experimental study of hydroxyalkyl peroxy radicals from OH-initiated reactions of isoprene, *Chem. Phys. Lett.*, **343**, 49-54, 2001.

Chapter 2

UTI 100C Upgrade

2.1 Introduction

The UTI 100C Precision Mass Analyzer (UTI) used in this work is a commercially available residual gas analyzer designed for use in a variety of applications. A diagram of the instrument is shown in Figure 2-1. The UTI instrument is designed for electron impact ionization (EI) and is equipped with an open-design dual-filament ion source with a nominal detection limit of 0.1 ppm [*UTI Operating Manual*, 1990]. The reflector assembly (Figure 2-2) is charged to negative potentials with respect to ground ranging from -5 to -90 V. Electrons are emitted from the filaments and accelerated toward the grid assembly which is charged to a positive potential with respect to both the reflector and ground (+10 to +24 V). The ions pass through the grid volume and decelerate as they approach the reflector. The electrons reaccelerate toward the grid and continue this cycle through the grid volume until they ionize the gas or are lost to the grid.

$$M + e^- \longrightarrow M^+ + 2e^- \tag{2.1}$$

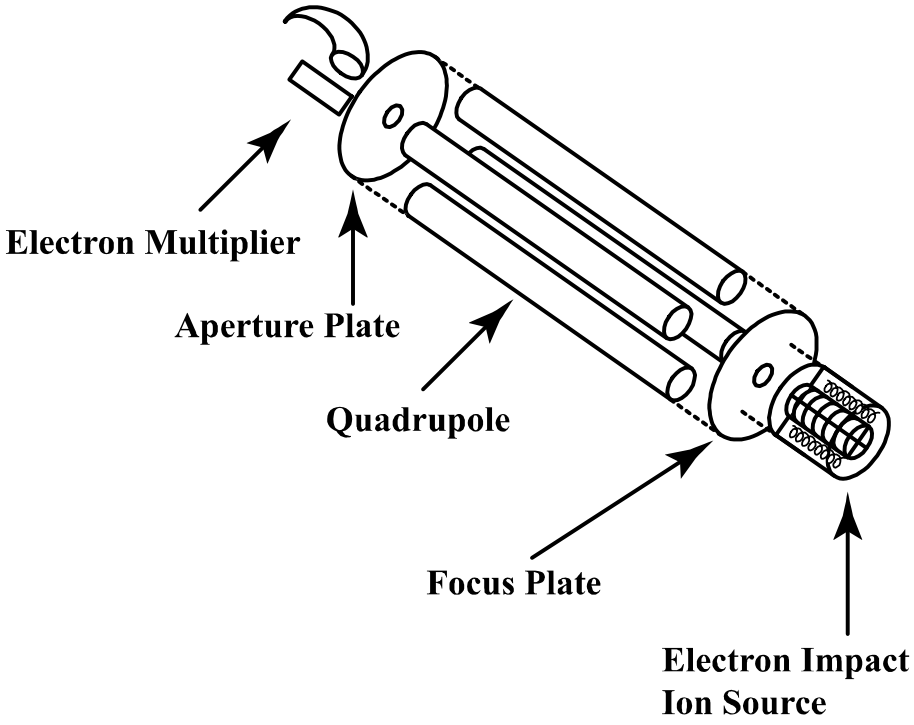

Figure 2-1: UTI 100C Precision Mass Analyzer

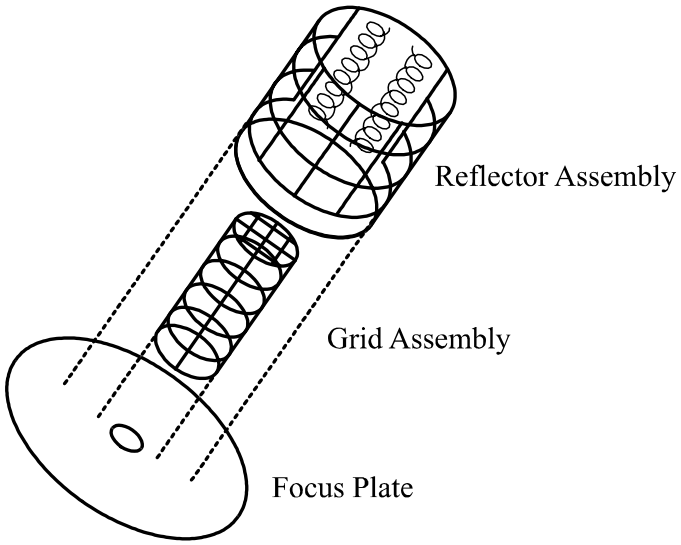

Figure 2-2: UTI 100C open ion source design showing the focus plate, reflector and grid.

The positive ions created by collisions with an electron (Equation 2.1) are extracted by the focus plate which is charged to a negative potential with respect to ground (-30 V). The ions are separated in the quadrupole and detected by a Channeltron electron multiplier capable of operating in both analog and pulse counting modes. The UTI is designed to operate in the analog mode as it is equipped with an analog pre-amplifier and a picoammeter which measures signal current directly from the amplifier.

The EI mode was not satisfactory for the kinetics experiments described later in this thesis for a number of reasons. First, even with low electron energies, stable organic species are fragmented so that the evaluation of spectra becomes difficult when a variety of species are present [*Harrison*, 1992]. The unstable organic radical intermediate species may also be fragmented to the point where a parent ion peak is not detected, rendering the identification of these species difficult if not impossible. Second, the nominal sensitivity of this instrument is not sufficient for detecting the radical species of interest in the flow tube. The concentrations of radical intermediates produced in the flow tube experiments are between 10^9-10^{11} molecules cm^{-3}. The experiments were performed under high pressure conditions, generally 100-200 Torr, corresponding to radical concentrations below 0.1 ppm. These concentrations are below the nominal detection limit of the UTI instrument in its original configuration. Third, the instrument is not configured for detection of negative ions. Many radical species of interest can only be detected using negative chemical ionization reaction schemes. Therefore, the conversion of the UTI to a CIMS system capable of detecting both positive and negative ions was necessary.

2.2 UTI Conversion

2.2.1 Ion source

The first step in the conversion of the UTI to a CIMS system was the development of an external ion source. There are a number of methods in the literature to produce ions, however, the two generally used in our group are corona discharge and α-particle bombardment from a radioactive ^{210}Po source [*Lipson et al.*, 1999; *Percival et al.*, 1997]. The potential for producing larger ion currents with the corona discharge gave it an advantage over the polonium source for the initial setup of the instrument. The corona discharge technique is well suited to the production of both positive and negative ions. However, the detection of many organic species can only be accomplished using positive chemical ionization [*Harrison*, 1992]. A mixture of helium (3 STP L min^{-1}) and oxygen (0.1 STP cm^3 min^{-1}) was passed over a corona discharge needle at +4 kV with respect to ground. The corona discharge needle was housed in a $\frac{1}{4}$" o.d. stainless steel tube which was grounded. The needle was shielded from the stainless steel tube by a glass sheath which left only the needle tip exposed. In this way, the discharge was localized at the tip of the needle, leading to more efficient ion production. Discharge currents were typically 35 μA. The major ion peak detected using this method for production of positive ions was O_2^+. A sample spectrum is shown in Figure 2-3. The dominant peak is O_2^+ (32 amu) but there are also small signals at 16 amu (O_2^{2+} or O^+) and 28 amu, corresponding to N_2^+. Other ions of interest could be generated using water vapor (H_3O^+) or nitric oxide (NO^+) as a trace species in the helium carrier gas. Similar techniques were used in the production of negative ions. For example, a mixture of N_2 and SF_6 was passed over a needle charged to -4 kV to produce SF_6^-.

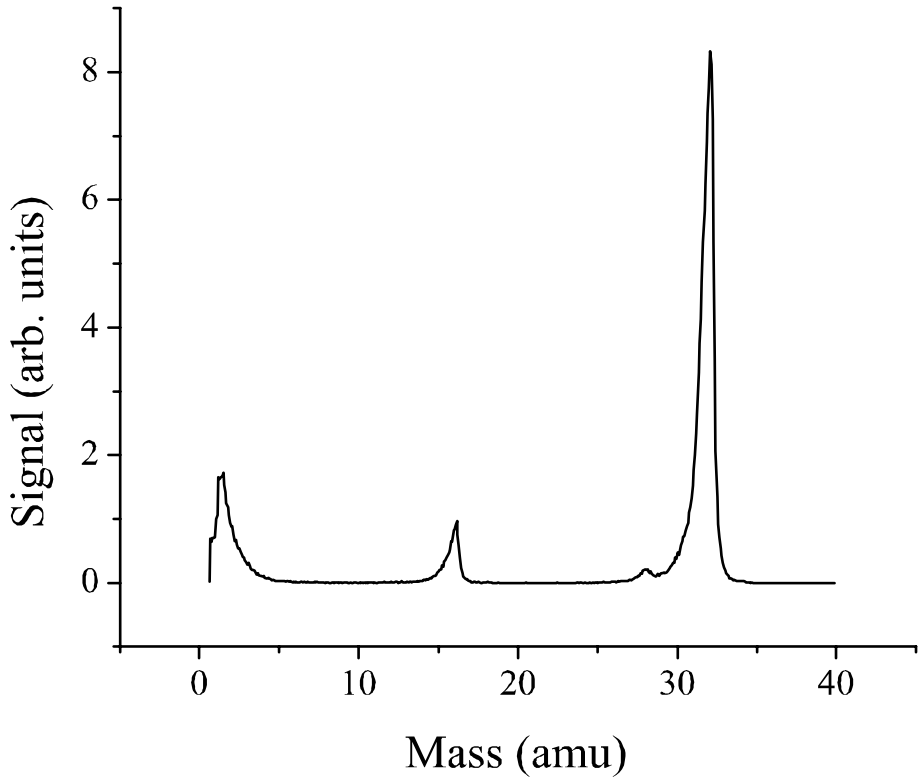

Figure 2-3: Sample positive ion spectrum of a corona discharge of He/O_2 using the UTI 100C for ion detection.

2.2.2 Chamber design

The chemical ionization reactions in these experiments occur outside the vacuum chamber housing the UTI. The ions must then be transported from the flow tube to the quadrupole where they are separated. The vacuum chamber housing the UTI consists of two differentially pumped stainless steel chambers. The first is pumped by a Varian diffusion pump (model VHS-6) and is maintained at a pressure of 10^{-4} to 10^{-5} Torr under flow conditions. The second chamber houses the quadrupole and electron multiplier and is pumped by a Varian turbomolecular drag pump (model V550). The pressure in this chamber is maintained between 10^{-5} and 10^{-6} Torr under flow conditions. The ions and neutral molecules from the flow tube

are pumped by an Edwards rotary vane pump (model E2M18). A 250 μm aperture allows a small gas flow from the flow tube into the first chamber. The ions must be transported a large distance (approx. 6") before they enter the electron impact source region. The ions pass through the electron impact source and into the second chamber to be analyzed by the quadrupole. Figure 2-4 shows a diagram of the two chambers.

Various ion optics were used to transport the ions effectively from the front aperture to the quadrupole. A voltage was applied to the front aperture to help focus the ions as they enter the first chamber. The reflector assembly must be grounded so that no electrons are produced at the filaments, however the grid assembly and focus plate can be biased to aid in focusing and attracting the ions toward the quadrupole. The primary challenge, however, was transporting the ions over the large distance from the aperture to the electron impact source.

Ion guide

The electrostatic ion guide has been used to transport ions in mass spectrometric applications for years [*Geno & Macfarlane*, 1986; *Bondarenko & Macfarlane*, 1997]. Recent papers have also described the use of the ion guide in chemical ionization applications [*Zhang et al.*, 1998; *Zhang et al.*, 2000]. The ion guide consists of a $1\frac{1}{2}$" diameter mesh cylinder mounted axially along the vacuum chamber. A wire is mounted in the center of the cylinder and runs the entire length of the cylinder ($6\frac{1}{4}$"). These two components are electrically isolated from each other and the chamber and can be biased independently. For the detection of positive ions, the wire was biased negative with respect to the cylinder so that ions were attracted toward the wire. The ions enter the chamber with a specific kinetic energy and develop a stable spiralling trajectory around the wire [*Zhang et al.*, 2000]. The mesh cylinder allows neutral species to be

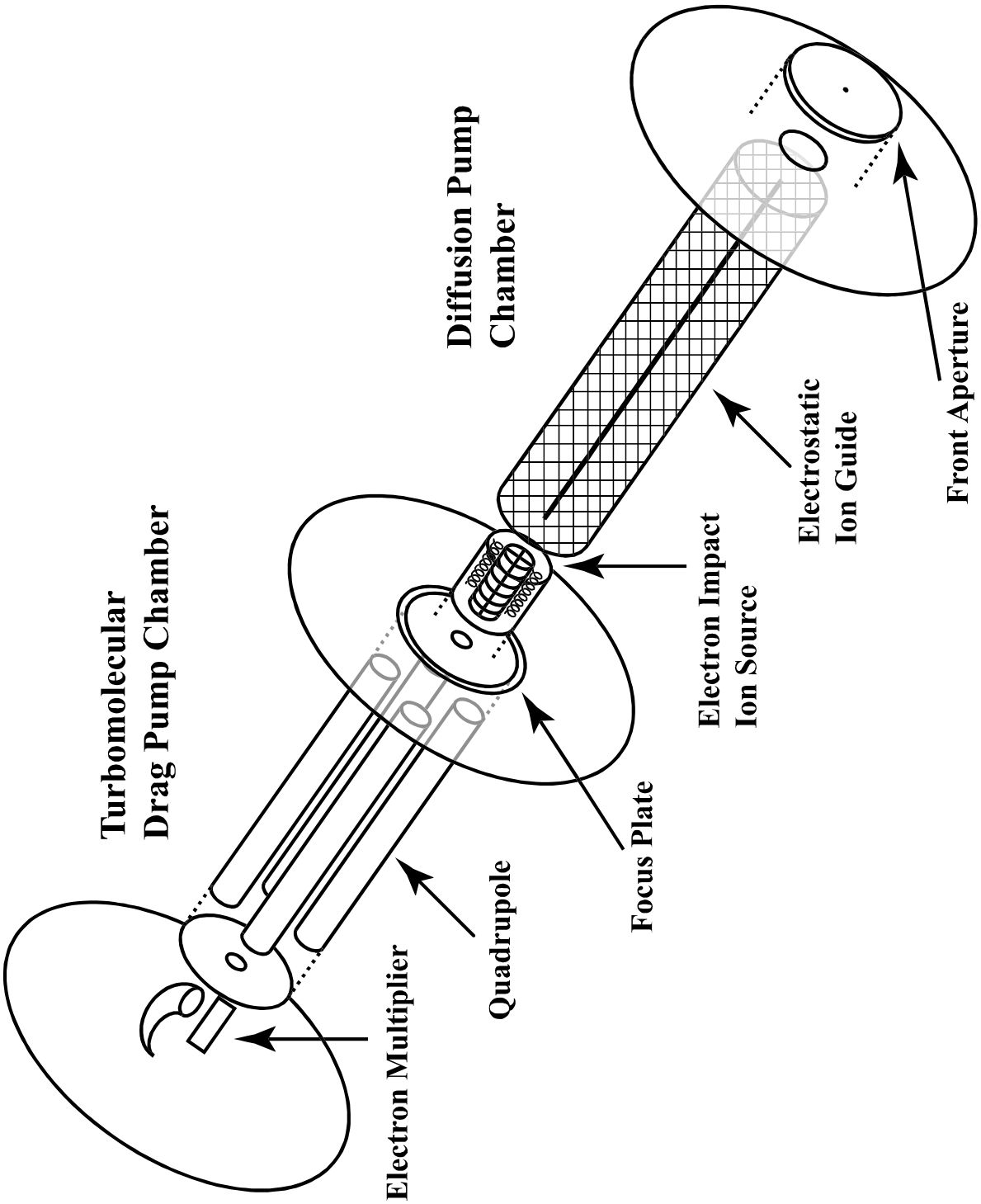

Figure 2-4: Chamber design utilizing the ion guide to transport ions from the front aperture to the quadrupole.

pumped away by the diffusion pump. In this way, the ions of interest are transported along the length of the ion guide and enter the electron impact source region where they are focused into the quadrupole. A diagram of the chamber design utilizing the ion guide is shown in Figure 2-4. Typical voltages used for the ion guide design are given in Table 2.1.

Electrostatic lenses

An alternative to the ion guide was the use of electrostatic lenses to transport the ions to the quadrupole. This technique has been well established in our laboratory [*Seeley et al.*, 1996]. For this application, however, electrostatic lenses have distinct disadvantages. The lenses need to be spaced approximately $\frac{1}{2}$" to 1" apart for maximum transmission efficiency. The efficiency of electrostatic lenses decreases over long distances. Therefore, the efficiency and cost constraints of a set of electrostatic lenses spanning the 6" from the front aperture to the electron impact source were large deterrents for this method. These limitations were overcome by the design of a "top hat" flange for the diffusion pump chamber. This flange effectively placed the front aperture approximately $4\frac{1}{2}$" closer to the electron impact source. The remaining $1\frac{1}{2}$" were spanned by a set of 3 electrostatic lenses spaced $\frac{1}{2}$" apart. The lens stack consisted of a set of 3 copper gaskets with an outer diameter of $1\frac{7}{8}$" and an inner diameter of $1\frac{7}{16}$". The pumping efficiency of the diffusion pump was not significantly affected, as pressures of 10^{-4} to 10^{-5} Torr could be achieved in the first chamber under flow conditions for both the ion guide and top hat designs. A diagram of the modified chamber with electrostatic lenses is shown in Figure 2-5. Representative voltages for the top hat ion optics are also given in Table 2.1.

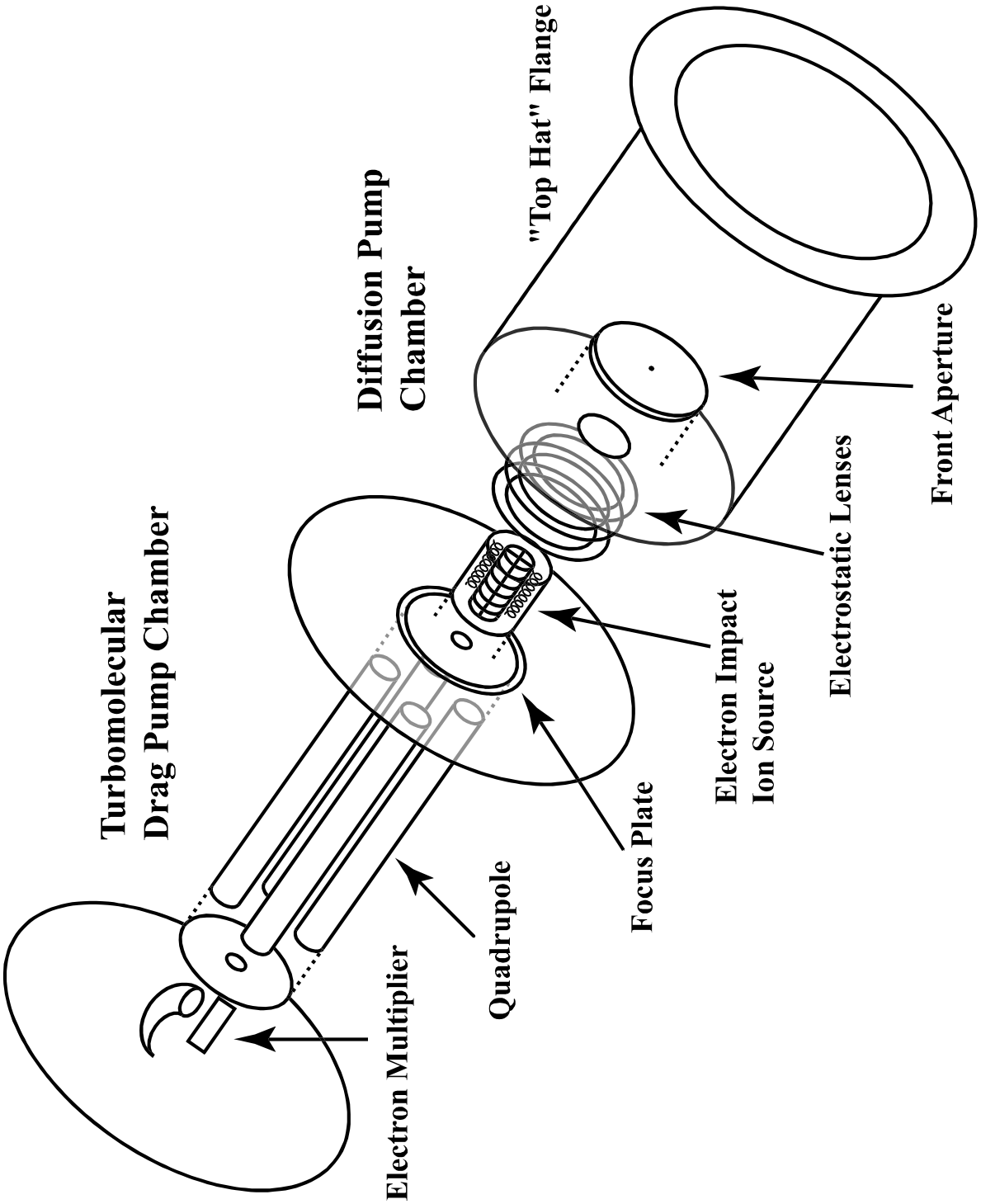

Figure 2-5: Chamber design utilizing the "top hat" flange and electrostatic lenses to transport ions from the front aperture to the quadrupole.

Ion Optic	Ion Guide Voltages	Top Hat Voltages
Front Aperture	+50	+30
Mesh Cylinder	+30	—
Wire	0	—
Lens 1	—	+25
Lens 2	—	0
Lens 3	—	+10
Grid Assembly	+5	+15
Focus Plate	-25	-30

Table 2.1: Ion optic voltages for positive ion detection.

2.2.3 Negative ion detection

The conversion of the UTI to a chemical ionization instrument opens the possibility for both positive and negative ion production and detection. The original configuration of the UTI, however, allows for detection of positive ions only (Figure 2-6). There are two methods for

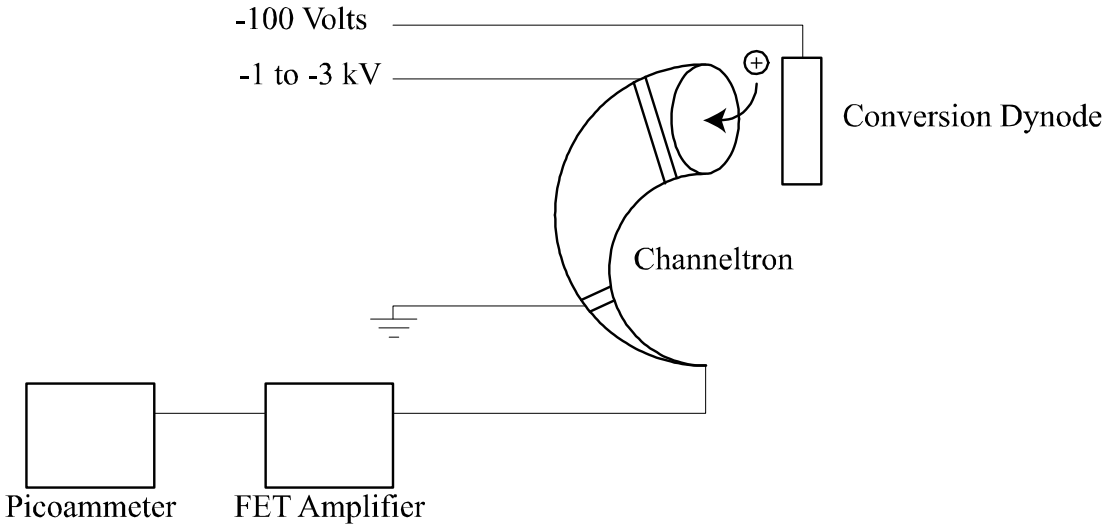

Figure 2-6: UTI analog signal detection scheme for positive ions

modifying the UTI for negative ion detection. The first method is to bypass the -100 V output to the conversion dynode shown in Figure 2-6. A high voltage power supply could be

used to apply a voltage of +3 to +5 kV to the conversion dynode. The negative ions would be attracted to the conversion dynode and upon impact would be converted to positive ion fragments through an ion sputtering process. The positive ions would be repelled from the dynode and be attracted to the negatively charged Channeltron. This detection scheme is illustrated in Figure 2-7.

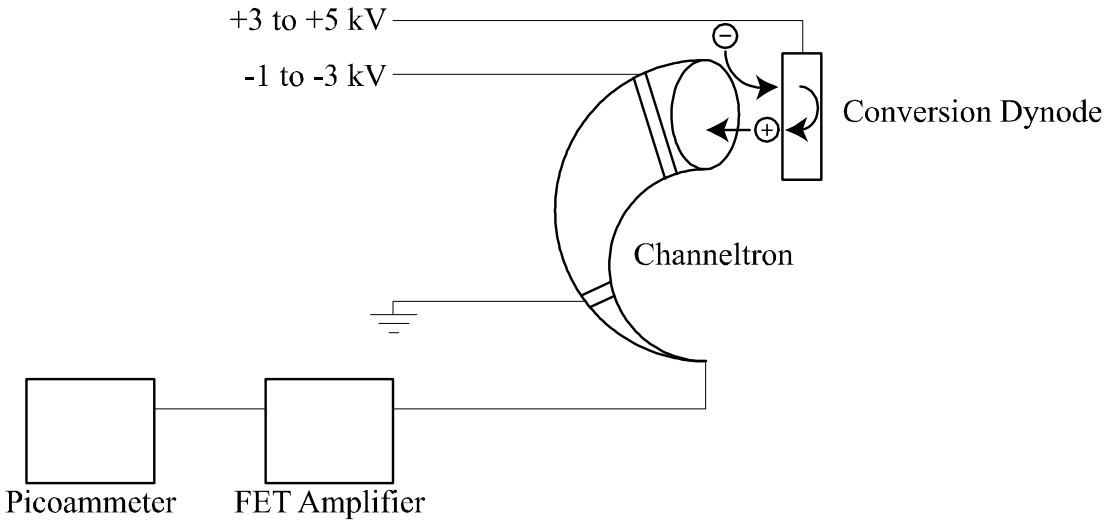

Figure 2-7: UTI analog signal detection scheme for negative ions.

The second option for the detection of negative ions is to convert the system to a pulse counting instrument. The negative ions would directly impinge on the positively charged (+2 kV) Channeltron electron multiplier. Secondary electrons would be generated and begin a cascade of electrons toward the positively charged (+4 kV) rear of the multiplier. The electrons would then be collected on the highly positively charged collector (+4.1 kV). Analog currents cannot be measured directly at high voltages, therefore the detection electronics are shielded from the high voltages by a pF capacitor and the signal is converted to pulses by a pulse counting pre-amplifier. A rate meter then counts the pulses and converts the signal from

the preamplifier into counts per second (cps).

There are several points of comparison for these two methods. The sputtering efficiency of the conversion dynode is poor compared to the efficiency of the Channeltron in converting an ion to secondary electrons. There is a significant loss of ion signal, therefore, in using the conversion dynode to detect negative ions. However, use of the conversion dynode is more straightforward since the only additional equipment needed is a high-voltage power supply. The pulse counting detection scheme requires a high voltage power supply as well as a pulse counting pre-amplifier and a rate meter, so the cost of converting the UTI to a pulse counting instrument was higher than using the conversion dynode. Due to the increased sensitivity inherent in pulse counting techniques, the extra cost of converting to pulse counting mode was determined to be worthwhile.

Figure 2-8 illustrates the final instrument setup including the electronics for switching between positive and negative ion modes. In negative ion detection mode, the double pole switch is in the up position as shown in the diagram. The counting preamplifier receives approximately +4 kV from the high voltage power supply and sends approximately +3.8 kV to the collector and +3.6 kV to the Channeltron. The resistance of the channeltron is approximately 80 MΩ, so the variable resistor acts as a voltage divider between the channeltron and ground. If the variable resistor is set to 80 MΩ the +3.6 kV sent to the multiplier will be split evenly. The front of the Channeltron will have a voltage of +1.8 kV, the back will have a voltage of +3.6 kV, and the signal collector will have a voltage of +3.8 kV. This way, the electrons are attracted to the collector once they reach the end of the channeltron. Conversely, if the double pole switch is reversed for positive ion detection and the variable resistor is set to 0Ω, the front of the channeltron receives a 3 kV negative bias and the collector and rear of the channeltron

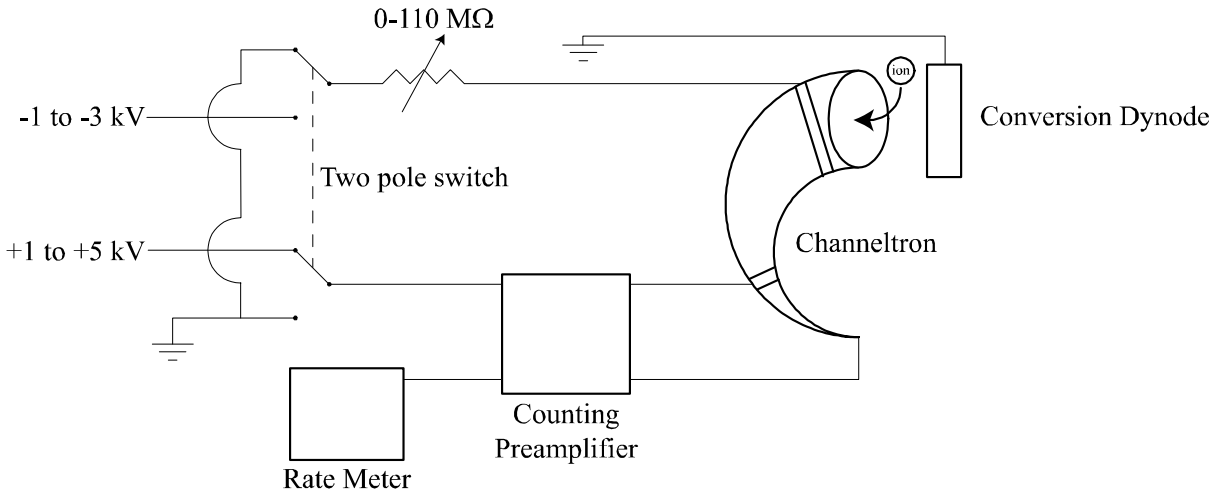

Figure 2-8: UTI configuration for both positive and negative ion detection in pulse counting mode

are both at ground. In this way, the instrument is changed from positive to negative ion modes by the simple throw of a switch.

2.3 Results and Conclusions

The ion transmission efficiency of the ion guide design compared to the electrostatic lens design was investigated. The ion signal produced by the corona discharge of a mixture of Ar (3 STP L min^{-1}) and SF_6 (0.1 STP cm^3 min^{-1}) for the two designs is shown in Figure 2-9. The ion signal shown for each case is the maximum signal achieved after tuning all ion optic voltages. The SF_6^- signal achieved using the ion guide is a factor of five lower than the signal achieved using the lenses. The same trend was observed for positive ion detection of O_2^+. The ion guide was never directly compared to the lenses over the same transmission distance due to design constraints, however, the lens design with the top hat flange is clearly superior to the ion guide

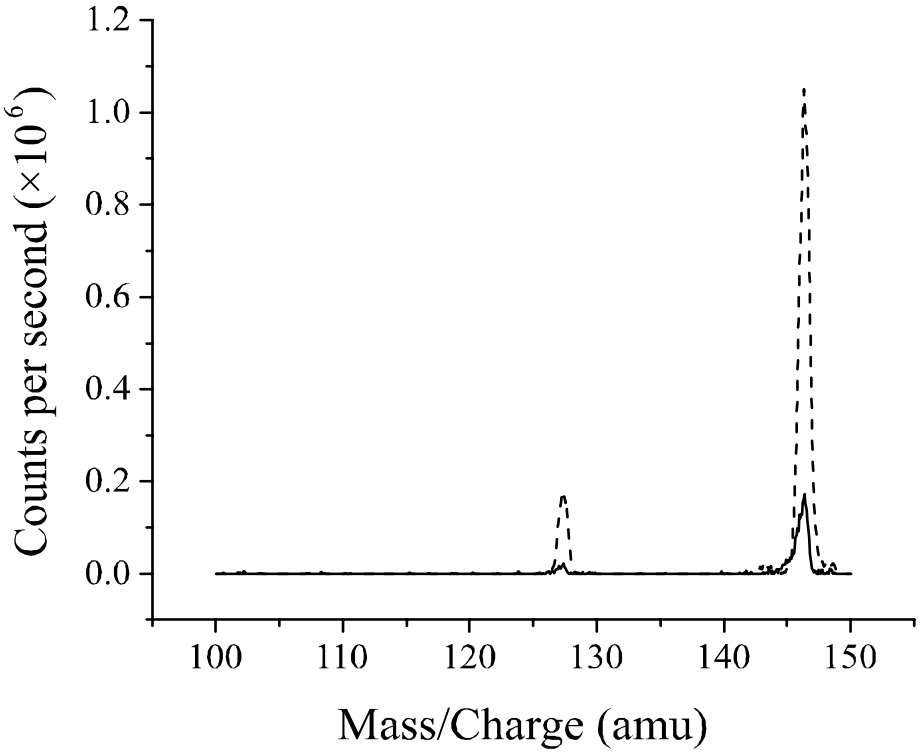

Figure 2-9: Optimal SF_6^- signal intensities for both the ion guide and top hat lens design. (—) represents the ion guide design and (– –) represents the top hat design.

for this chamber design.

The ^{210}Po ion source (Nuclecel P-2031) was also used to generate both positive and negative ions. A mixture of N_2 (5 STP L min^{-1}) and SF_6 (1 STP cm^3 min^{-1}) was passed through the polonium source. The proposed mechanism for ion production in the radioactive polonium source is as follows:

$$\alpha^{2+} + N_2 \longrightarrow \alpha^{2+} + N_2^+ + e^- \tag{2.2}$$

$$SF_6 + e^- \longrightarrow SF_6^- \tag{2.3}$$

The polonium source generally produces lower ion currents than the corona discharge, however the absence of a high energy electrical discharge reduces background counts at the multiplier. Dark noise from the polonium source (1-10 cps) was generally one order of magnitude lower than with the corona discharge (10-100 cps). Unfortunately, no ion signal was detected with the ion guide design using the polonium source for ion generation. Ion signal was detected, however, using the top hat design with electrostatic lenses. For the top hat design, the SF_6^- signal was generally two orders of magnitude lower with the polonium source compared to the corona source. Comparative signal levels for the various ion sources and ion optic designs are shown in Table 2.2.

	Ion Guide (cps)	Top Hat (cps)
^{210}Po signal level	0	5×10^3
^{210}Po noise level	0	1-10
Corona signal level	1×10^5	5×10^5
Corona noise level	10-100	10-100
Maximum S/N	1×10^4	5×10^4

Table 2.2: Typical SF_6^- signal levels and maximum signal-to-noise ratios for both chamber designs.

The largest signal-to-noise ratio achieved was using the corona discharge ion source with the top hat chamber design. Therefore, the kinetics experiments were performed using this setup. The absence of signal for the combination of the ion guide with the polonium source may indicate that the performance of the ion guide is correlated to the energy of the ions. The ion trajectory through the ion guide may only be stable for a specific range of ion energies and the polonium source may not produce ions in that range.

A sensitivity analysis was performed using the top hat design with corona discharge to determine if the instrument had sufficient sensitivity to detect low concentrations of relevant

species. The flow tube setup used in the sensitivity experiments is shown in Figure 2-10. The flow tube and chemical ionization apparatus consists of two differentially pumped regions separated by a 1 mm aperture. The sensitivity experiments were conducted at conditions similar to those used for kinetics experiments. Ultra-high purity N_2 (BOC 99.999%) was used as the high flow (50 STP L min^{-1}) carrier gas in the flow tube and the gas was pumped by a Varian rotary vane pump (model SD-700). The pressure in the flow tube was maintained at 100 Torr under flow conditions. NO_2 was introduced through a moveable injector which had a fan-shaped teflon turbulizer at the end to induce turbulence and enhance mixing. A small portion of the gas from the flow tube was pumped through the 1 mm aperture between the flow tube and CI region. The CI region was maintained at a pressure of 20 Torr under flow conditions. The ion-molecule reaction time was approximately 4 ms for the flow and pressure conditions given. A sample calibration curve is given in Figure 2-11. A calibration mixture of NO_2 (Matheson 99.5%) was prepared by purification through several freeze-pump-thaw cycles and dilution with N_2 (BOC 99.999%). NO_2 flows were measured through a calibrated flowmeter (Tylan FM-360).

The sensitivity of the UTI to NO_2 using the detection scheme shown in Equation 2.4 ($k_{2.3}$ = 1.4×10^{-10} cm^3 $molecule^{-1}$ s^{-1}) [*Huey et al.*, 1995] is approximately 1×10^9 molecules cm^{-3} cps^{-1}.

$$SF_6^- + NO_2 \longrightarrow SF_6 + NO_2^- \tag{2.4}$$

For a signal-to-noise ratio of 2 and 1 second integration time, this sensitivity corresponds to a detection limit for NO_2 of approximately 10 ppb in the flow tube. This limit is an order of magnitude lower than the nominal sensitivity of the UTI in electron impact ionization mode.

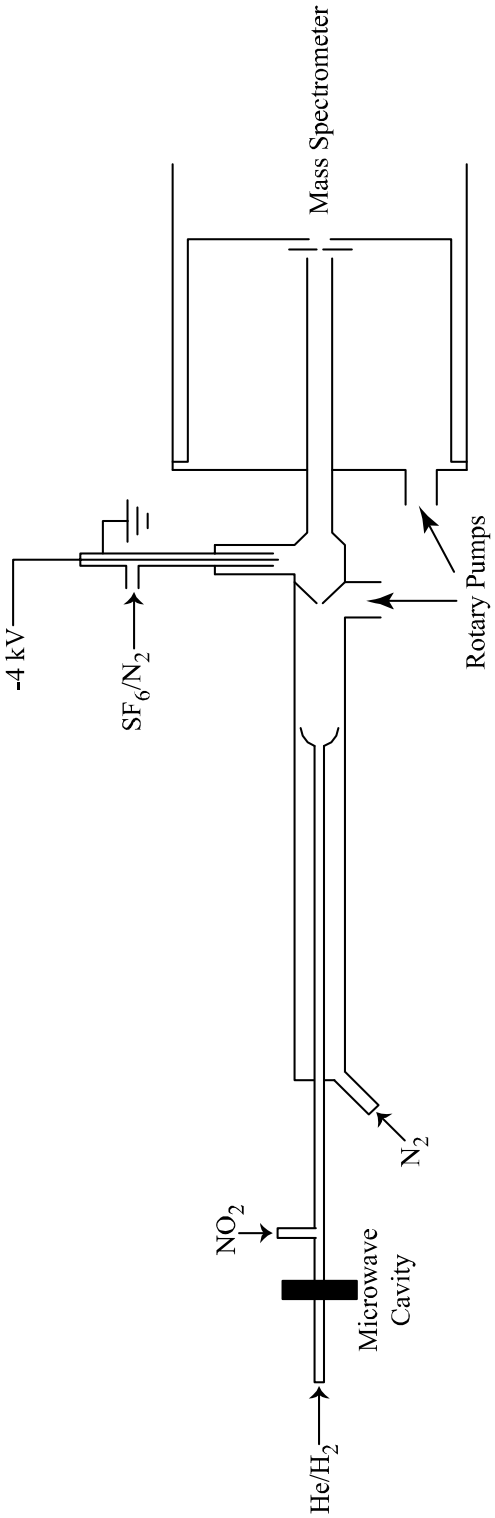

Figure 2-10: Experimental setup for NO_2 sensitivity analysis.

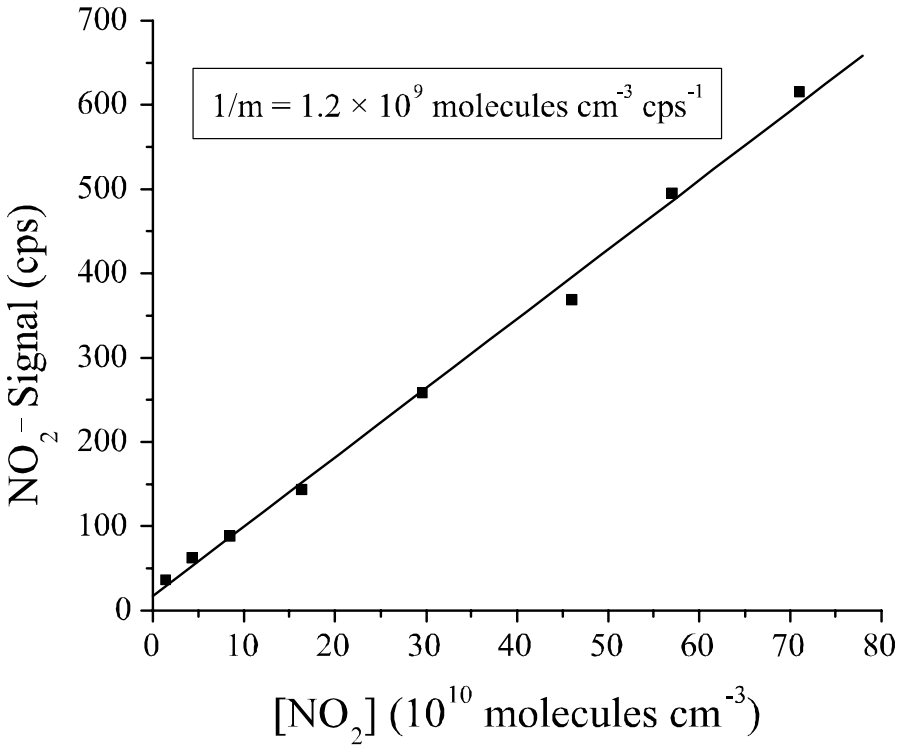

Figure 2-11: Calibration of NO_2 sensitivity using SF_6^- produced by corona discharge. (–) represents a linear least squares fit to the data.

Higher sensitivities have been achieved for species such as OH due to faster reaction rates with SF_6^-. Other chemical ionization instruments in the laboratory have been able to obtain NO_2 sensitivities as low as 1-5 $\times$ 10^7 molecules cm^{-3} cps^{-1} [*Percival et al.*, 1997]. These higher sensitivities are achieved by more efficient ion transmission to the quadrupole and longer ion-molecule reaction times.

In conclusion, the modifications made to the UTI 100C allow the detection of both positive and negative ions in analog and pulse counting modes. The use of a "top hat" flange coupled to electrostatic lenses was determined to produce larger ion signals than the ion guide for the space constraints of this system. The sensitivity of the UTI instrument has been improved

from 0.1 ppm levels to 1-10 ppb for most species of interest. This improvement in sensitivity should be sufficient to allow the detection of most stable organic species and many organic radical species as well. The conversion of the UTI to chemical ionization also holds promise for the detection of organic species with the M^+ or $[M+H]^+$ peak allowing for easier identification of the species of interest. .

References for Chapter 2

Bondarenko, P.V. and R.D. Macfarlane, A new electrospray ionization time-of-flight mass spectrometer with electrostatic wire ion guide, *International Journal of Mass Spectrometry and Ion Processes*, **160**, 241-258, 1997.

Geno, P.W. and R.D. Macfarlane, ^{252}Cf plasma desorption mass spectrometry at low acceleration voltages using the electrostatic particle guide, *International Journal of Mass Spectrometry and Ion Processes*, **74**, 43-57, 1986.

Harrison, A.G., *Chemical Ionization Mass Spectrometry*, CRC Press, Boca Raton, 1992, pp. 113-120.

Huey, L.G., D.R. Hanson, and C.J. Howard, Reactions of SF_6^- and I^- with atmospheric trace gases, *J. Phys. Chem.*, **99**, 5001-5008, 1995.

Lipson, J.B., T.W. Beiderhase, L.T. Molina, M.J. Molina, and M. Olzmann, Production of HCl in the OH plus ClO reaction: laboratory measurements and statistical rate theory calculations, *J. Phys. Chem. A*, **103**, 6540-6551, 1999.

UTI Model 100C Precision Mass Analyzer Operating & Service Manual, UTI Instruments Co., San Jose, CA, 1990, sec. III-8.

Percival C.J., G.D. Smith, L.T. Molina, and M.J. Molina, Temperature and pressure dependence of the rate constant for the ClO + NO_2 reaction, *J. Phys. Chem.*, **101**, 8830-8833, 1997.

Seeley, J.V., R.F. Meads, M.J. Elrod, and M.J. Molina, Temperature and pressure dependence of the rate constant for the HO_2 + NO reaction, *J. Phys. Chem*, **100**, 4026-4031, 1996.

Zhang, R., W. Lei, L.T. Molina, and M.J. Molina, Ion transmission and ion/molecule separation using an electrostatic ion guide in chemical ionization mass spectrometry, *International Journal of Mass Spectrometry*, **194**, 41-48, 2000.

Zhang, R., L.T. Molina, and M.J. Molina, Development of an electrostatic ion guide in chemical ionization mass spectrometry, *Review of Scientific Instruments*, **69**, 4002-4003, 1998.

Chapter 3

Methane Oxidation Reactions

3.1 Introduction

The mechanism of ozone production in the troposphere does not depend on photolysis of O_2 since sunlight of sufficient wavelength does not penetrate into the troposphere. The production of ozone is instead driven by the reaction of $O(^3P)$ with oxygen (Reaction 1.8). Oxygen atoms are formed from the photolysis of NO_2 produced by the reactions of peroxy radicals (RO_2). The coproduct of NO_2 photolysis, NO, can be converted back to NO_2 by reaction with ozone:

$$NO + O_3 \longrightarrow NO_2 + O_2 \tag{3.1}$$

Therefore, a photostationary state is established between NO, NO_2, and O_3 in the sunlit atmosphere [*Tyndall et al.*, 2001]. Any reactions that convert NO to NO_2 other than Reaction 3.1 lead to net production of ozone. Examples of these reactions are the reactions of HO_2 and

RO_2 radicals with NO.

$$RO_2 + NO \longrightarrow RO + NO_2 \tag{3.2}$$

$$HO_2 + NO \longrightarrow OH + NO_2 \tag{3.3}$$

The alkoxy radical produced in Reaction 3.2 reacts further to produce an aldehyde or ketone and HO_2, which will regenerate OH. This hydroxyl radical, OH, can regenerate RO_2 by the reaction with another organic molecule. This oxidation cycle is illustrated in Figure 3-1.

The key reactions leading to ozone production in the troposphere involve peroxy radicals. As mentioned earlier in Chapter 1, methane is the most abundant hydrocarbon in the atmosphere, and therefore the methyl peroxy radical (CH_3O_2) is also a very important species in the troposphere. The reaction of CH_3O_2 with NO has been extensively studied and the overall rate constant is well known ($k_{3.4} = 7.7 \times 10^{-12}$ cm^3 molecule s^{-1}) [*DeMore et al.*, 1997].

$$CH_3O_2 + NO \longrightarrow CH_3O + NO_2 \tag{3.4}$$

$$\xrightarrow{M} CH_3ONO_2 \tag{3.5}$$

This reaction was therefore chosen as a trial study for the UTI CIMS experimental setup. A sample of the previous studies of this reaction and the results are summarized in Table 3.1. The branching ratio of this reaction (Reaction 3.5) to form the stable methyl nitrate (CH_3ONO_2) is important because it represents a radical sink in areas of high NO_x concentration. CH_3ONO_2 has been measured in the atmosphere and of the simple alkyl nitrates is present in the highest concentrations, up to 220 ppt [*Finlayson-Piits & Pitts*, 2001]. This branching ratio has been

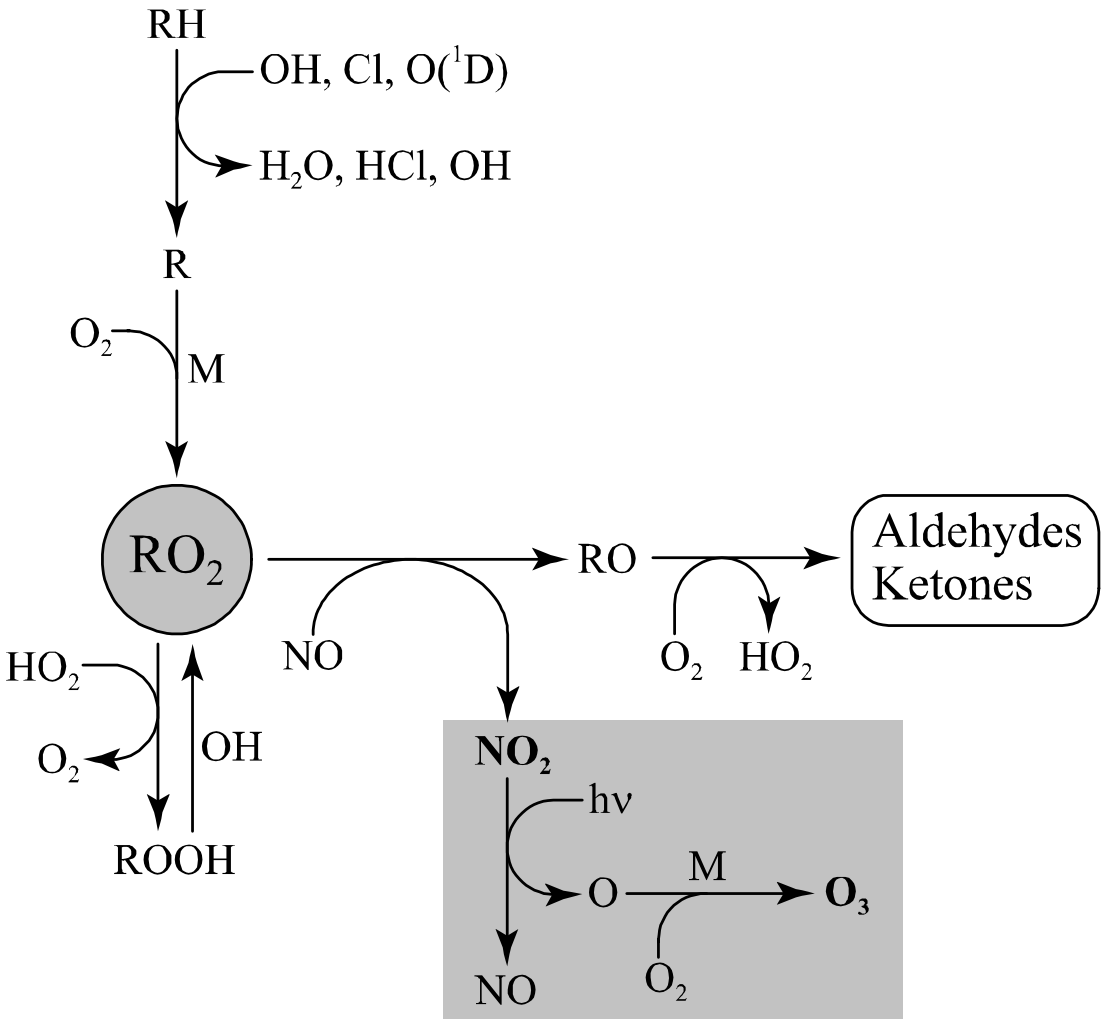

Figure 3-1: Ozone production cycle in the troposphere involving organic species (R), NO_x, and O_3.

directly measured in a recent study which is also summarized in Table 3.1 [*Scholtens et al.*, 1999]. The branching ratio measurement is outside the scope of this initial experiment, however.

Reference	$\mathbf{k}_{3.4}$ (298 K)[a]	$\mathbf{k}_{3.4}/\mathbf{k}_{(3.4+3.5)}$ (298 K)	**Method**[b]
Cox & Tyndall, 1980	6.5×10^{-12}	—	MMS
Scholtens et al., 1999	7.8×10^{-12}	< 0.03	DF-CIMS
Zellner et al., 1986	7×10^{-12}	< 0.2	FP-LIF
Ravishankara et al., 1981	8.1×10^{-12}	< 0.24	FP-LIF
Sander & Watson, 1980	7.1×10^{-12}	—	FP-UV
Simonaitis & Heicklen, 1981	7.7×10^{-12}	—	FP-UV
Plumb et al., 1981	8.6×10^{-12}	—	DF-EIMS
Villalta et al., 1995	7.5×10^{-12}	—	FT-CIMS
Masaki et al., 1994	1.12×10^{-11}	—	LP-PIMS

Table 3.1: Comparison of room temperature rate constant values for the CH_3O_2 + NO reaction. [a]Rate constants are given in units of cm^3 $molecule^{-1}$ s^{-1}. [b]FP=flash photolysis, LP=laser photolysis, FT=flow tube, DF=discharge flow, MMS=molecular modulation spectrometry, CIMS=chemical ionization mass spectrometry, EIMS=electron impact mass spectrometry, PIMS=photoionization mass spectrometry, UV=ultraviolet absorption, LIF=laser induced fluoresence.

Another important reaction of the CH_3O_2 radical is the reaction with HO_2. In areas of low NO_x concentrations, the cross-reactions of peroxy radicals with each other will dominate other reaction channels such as reaction with NO. The reaction of CH_3O_2 with HO_2 represents a radical sink in the troposphere and is important for modeling the chemistry of low NO_x air masses such as the marine boundary layer. There are two likely channels for this reaction:

$$CH_3O_2 + HO_2 \longrightarrow CH_3OOH + O_2 \tag{3.6}$$

$$\longrightarrow HCHO + H_2O + O_2 \tag{3.7}$$

The first channel (Reaction 3.6) produces methyl peroxide (CH_3OOH) which is soluble in water and can be removed from the atmosphere by deposition or precipitation. The second channel (Reaction 3.7) produces formaldehyde (HCHO) which is not as soluble in water as methyl

peroxide, but is a very important photolytic source of radical species in the troposphere.

$$HCHO \xrightarrow{h\nu} H + HCO \tag{3.8}$$

$$\xrightarrow{h\nu} H_2 + CO \tag{3.9}$$

The recommendation for the overall rate constant for the reaction of CH_3O_2 with HO_2 is $k_{3.6}$ $= 5.6 \times 10^{-12}$ cm^3 molecule s^{-1} [*DeMore et al.*, 1997]. The recommendation for the branching ratio is $k_{3.6}/(k_{3.6} + k_{3.7}) = 1.0$ at all temperatures and pressures. Studies of this reaction have generally used the method of ultraviolet absorption for detection of the CH_3O_2 and HO_2 radicals. The broadband absorption spectra of these two radicals are weak and overlapping so that the determination of absolute concentrations is difficult.

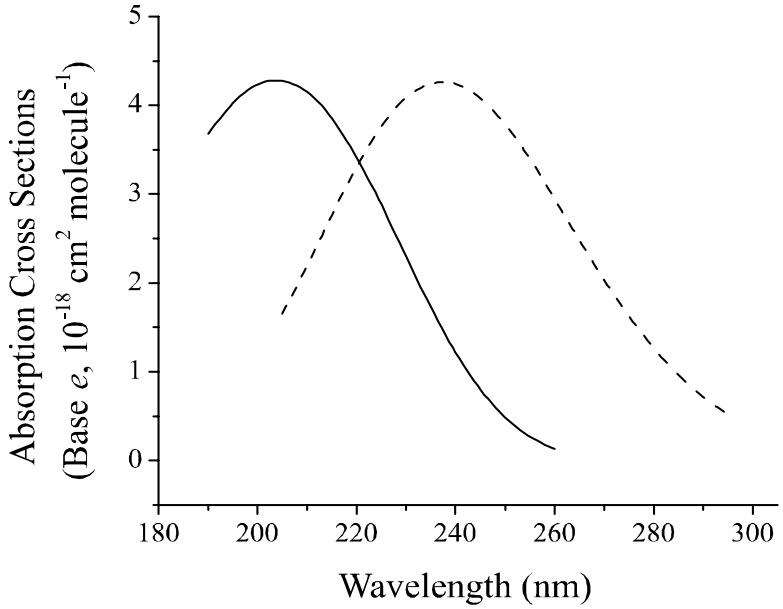

Figure 3-2: Recommended ultraviolet cross-section data for selected peroxy radicals. Plots represent HO_2 (—) and CH_3O_2 (– –).

Reference	$\mathbf{k}_{(3.6+3.7)}$ (298 K)[a]	$\mathbf{k}_{3.7}/\mathbf{k}_{(3.6+3.7)}$ (298 K)	**Method**[b]
Lightfoot et al., 1990	6.2×10^{-12}	—	FP-UV
Kurylo et al., 1987	2.9×10^{-12}	—	FP-UV
Jenkin et al., 1988	5.4×10^{-12}	0.4	MMS-UV-IR
Wallington, 1991	—	0.08	FP-IR
Kan et al., 1980	1.3×10^{-12}	—	FP-IR
McAdam et al., 1987	6.4×10^{-12}	—	FP-UV
Cox & Tyndall, 1979	6.0×10^{-12}	—	MMS-UV
Cox & Tyndall, 1980	6.5×10^{-12}	—	MMS-UV
Dagaut et al., 1988	2.9×10^{-12}	—	FP-UV
Moortgat et al., 1989	4.8×10^{-12}	0.3	MMS-UV-IR
Elrod et al., 2001	—	0.11	DF-CIMS

Table 3.2: Comparison of room temperature rate constant values for the $CH_3O_2 + HO_2$ reaction. [a]Rate constants are given in units of cm^3 $molecule^{-1}$ s^{-1}. [b]FP=flash photolysis, DF=discharge flow, MMS=molecular modulation spectrometry, CIMS=chemical ionization mass spectrometry, UV=ultraviolet absorption, IR=infrared absorption.

Large concentrations of the radicals must also be produced due to the relatively small ultraviolet cross-sections. The current cross-section recommendation is shown in Figure 3-2 [*Tyndall et al.*, 2001]. The overlapping absorption spectra and interference from the self-reactions of the peroxy radicals (Reaction 3.10 and 3.11) lead to difficulty in interpreting the time dependent absorption profiles which are measured in most of the studies to date (Table 3.2).

$$CH_3O_2 + CH_3O_2 \longrightarrow Products \tag{3.10}$$

$$HO_2 + HO_2 \longrightarrow H_2O_2 + O_2 \tag{3.11}$$

The ability to monitor the reactants without the use of ultraviolet absorption techniques is crucial in improving the current recommendation for this rate constant [*DeMore et al.*, 1997]. The difficulties in using the CIMS technique are in producing enough of the radical species to measure significant decays and in minimizing self reactions of the peroxy radicals.

3.2 CH_3O_2 + NO Kinetics

3.2.1 Experimental setup

The experimental setup consisted of a 16" long and 1" i.d. pyrex tube equipped with a $\frac{1}{4}$" o.d. pyrex moveable injector. The flowtube was coated with Halocarbon wax (Halocarbon Products, Inc.) to reduce raducal loss on the walls. The moveable injector was fitted with a teflon turbulizer to enhance mixing and help develop turbulent flow conditions [*Seeley*, 1994]. A diagram of the turbulizer is shown in Figure 3-3. The gas from the injector enters the left side of the turbulizer and is forced through the 24 pinholes distributed on the four teflon arms radiating from the turbulizer. This injection method shortens the mixing time in the flowtube. The N_2 carrier gas in the flowtube flows around the fan shaped part of the turbulizer which helps develop turbulence.

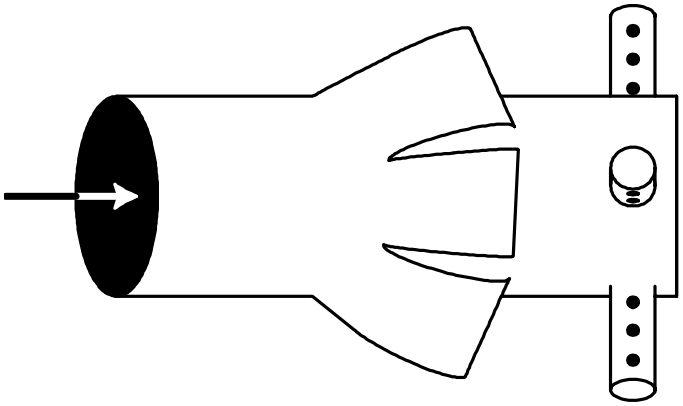

Figure 3-3: Diagram of the teflon turbulizer design used in the CH_3O_2 kinetics experiments.

CH_3O_2 was produced in a $\frac{1}{4}$" o.d. alumina sidearm at the rear of the flowtube. CH_3O_2 was produced in the sidearm through a series of chemical reactions. A mixture of UHP He (BOC 99.997%) (3 STP L min^{-1}) and F_2 (Matheson 2.0% in He) (0.01 STP cm^3 min^{-1}) was

introduced into the sidearm and passed through a microwave discharge cavity operating at 2.45 GHz and 15 W. CH_4 (BOC 99.97%) was introduced downstream of the microwave discharge cavity and reacted with the fluorine atoms. CH_4 was in excess and scavenged >99% of the fluorine atoms in 1 ms of reaction time. Approximately 1 ms downstream of the CH_4 inlet, UHP O_2 (BOC 99.994%) was added in excess and reacted with the methyl radicals present. The O_2 converted >99% of the CH_3 radicals into CH_3O_2 in the 2 ms of reaction time before the radicals entered the flow tube. The reactions producing CH_3O_2 are given below:

$$F_2 \xrightarrow{MW} F + F \tag{3.12}$$

$$F + CH_4 \longrightarrow HF + CH_3 \tag{3.13}$$

$$CH_3 + O_2 \xrightarrow{M} CH_3O_2 \tag{3.14}$$

($k_{3.13} = 6.7 \times 10^{-11}$ cm^3 molecule^{-1} s^{-1}, $k_{3.14} = 4.8 \times 10^{-13}$ cm^3 molecule^{-1} s^{-1}) [*DeMore et al.*, 1997].

Nitric oxide, NO, was introduced through the moveable injector. A sweep gas of UHP He (2 STP L min^{-1}) was mixed with NO (Matheson 99.0%). Before the NO was used, it was purified further to remove any trace unwanted nitrogen oxides. A sample of NO was collected at -196°C in an evacuated pyrex bulb with a cold finger. The frozen NO sample was pumped for approximately 5 minutes to remove any non-condensible gases. The cold finger was then placed in an acetone-dry ice slush bath at -80°C. Contaminants such as NO_2 (b.p. 21.2°C) and N_2O_3 (b.p. 3.5°C (dec)) remained in the bulb at this temperature while the NO (b.p. -151.8°C) was released. A portion of this purified NO was introduced into a passivated stainless steel canister and diluted with 4 atm UHP N_2 (BOC 99.999%). Final mixing ratios of the NO/N_2

mixtures ranged from 1% to 5%. Spectroscopic analysis of the mixtures yielded a NO_2/N_2 mixing ratio of $<10^{-4}$. The carrier gas (50 STP L min^{-1}) in the flow tube was UHP N_2 and the pressure was maintained at 100 Torr under full flow conditions. The flow tube effluent was pumped by a Varian SD-700 rotary vane pump. The flow tube was separated from the chemical ionization region by a 1 mm pyrex aperture. A small portion of the flow tube effluent ($\sim$ 500 STP cm^3 s^{-1}) passed through the 1 mm aperture and mixed with the ionization flow. The ionization flow consisted of 3 STP L min^{-1} UHP He mixed with 0.1 STP cm^3 min^{-1} UHP O_2 which passed over the corona discharge needle operating at +4 kV. The CI region was pumped by an Edwards E2M18 rotary vane pump and the pressure was maintained at 20 Torr under full flow conditions. Pressures in the flow tube and CI region were measured with an 0-1000 Torr capacitance manometer (MKS Beratron). A schematic of the experimental setup is shown in Figure 3-4.

3.2.2 Chemical ionization scheme

Ideally, the chemical ionization scheme used for this experiment would be able to simultaneously detect NO and CH_3O_2. A detection scheme has been previously developed for the detection of CH_3O_2 [*Villalta et al.*, 1995]. In this experiemnt, O_2^+ was used as the ionization reagent for

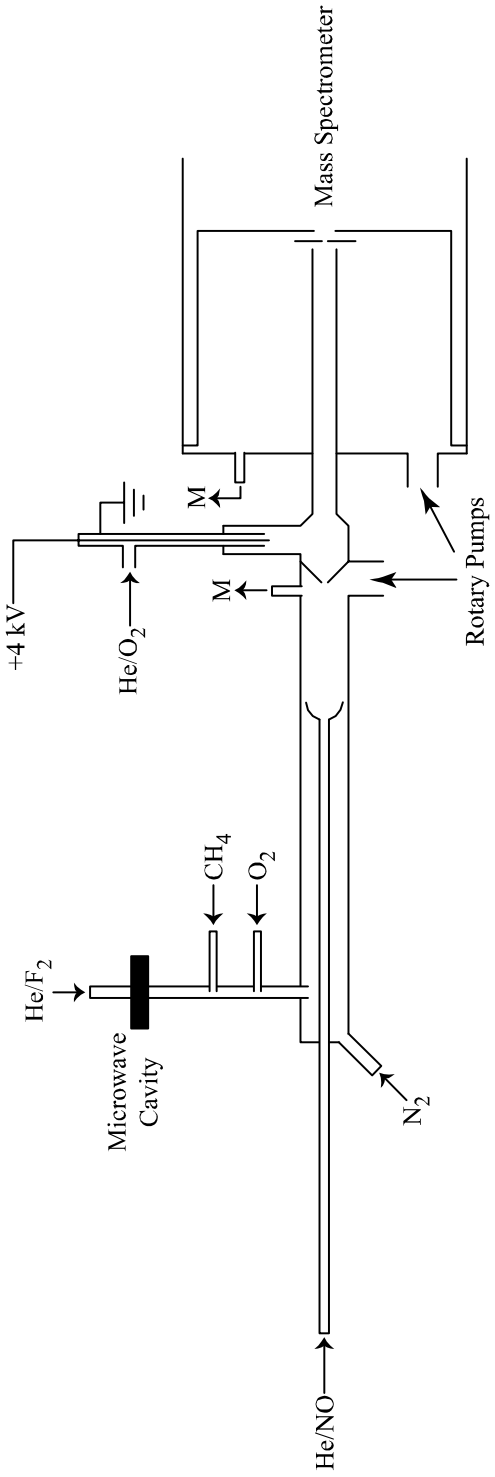

Figure 3-4: Experimental setup for the study of the reaction rate of CH_3O_2 + NO at room temperature and 100 Torr. M=capacitance manometer.

the detection of CH_3O_2. The reactions of O_2^+ with the molecules of interest are shown below:

$$O_2^+ + CH_3O_2 \longrightarrow O_2 + CH_3O_2^+ \quad (3.15)$$

$$\longrightarrow 2O_2 + CH_3^+ \quad (3.16)$$

$$O_2^+ + NO \longrightarrow O_2 + NO^+ \quad (3.17)$$

$$O_2^+ + NO_2 \longrightarrow O_2 + NO_2^+ \quad (3.18)$$

$$O_2^+ + CH_3 \longrightarrow O_2 + CH_3^+ \quad (3.19)$$

The reaction of O_2^+ with CH_3O_2 proceeds mainly through Reaction 3.16 while Reaction 3.15 accounts for only about 25% of the overall reaction [*Villalta et al.*, 1995]. This favors the detection of CH_3O_2 through the CH_3^+ ion, however the CH_3 radicals formed in the sidearm must be completely titrated with O_2 to form CH_3O_2 or interference will occur from Reaction 3.19. Additional motivation for the detection of CH_3O_2 as CH_3^+ is the interference of $^{15}NO_2^+$ and $N^{17}O_2^+$ at the $CH_3O_2^+$ mass channel (m/z=47). This interference could become significant as NO_2 is formed as a product of the reaction of CH_3O_2 with NO as well as being a product of side reactions in the flow tube.

3.2.3 Modeling and titration schemes

The kinetic data becomes significant easier to analyze when the reaction is performed under pseudo-first order conditions. Briefly, pseudo-first order kinetics holds when one of the reactants in a second order reaction is present in large excess so that its concentration does not change over the course of the reaction. The second order rate coefficient can be expressed as a product of the pseudo-first order constant, k_{1st}, and the concentration of the excess reagent. This greatly

simplifies the analysis of the kinetic data acquired in these experiments. In this reaction the concentration of NO was at least an order of magnitude higher than the CH_3O_2 concentration at all times. This could be experimentally observed by monitoring the NO^+ signal as the reaction time was varied. Under pseudo-first order conditions the NO concentration should remain constant for all reaction times. This condition held for typical CH_3O_2 concentrations, however a rough titration scheme for CH_3O_2 was also developed to ensure pseudo-first order conditions. The important reactions for the titration of CH_3O_2 are given below:

$$CH_3O_2 + NO \longrightarrow CH_3O + NO_2 \tag{3.20}$$

$$CH_3O + O_2 \longrightarrow CH_2O + HO_2 \tag{3.21}$$

$$HO_2 + NO \longrightarrow OH + NO_2 \tag{3.22}$$

$$CH_3O + NO \xrightarrow{M} CH_3ONO \tag{3.23}$$

The NO concentration must be large enough to convert all the CH_3O formed in Reaction 3.20 to methyl nitrite (CH_3ONO) in order to prevent the formation of HO_2 and subsequent formation of NO_2. The reaction and titration chemistry was modeled to insure that the side reactions of neither products nor reactants would interfere with the measurements. The reaction set used for the modeling is given in Table 3.3.

Figures 3-5 and 3-6 show the results of modeling the titration scheme. For each model run, the initial concentrations used were representative of the concentrations in the flow tube. Figure 3-5 shows that the CH_3O_2 should be completely converted to NO_2 and CH_3ONO on the time scale accessible in the flow tube for an NO concentration of 2.0×10^{13} molecules

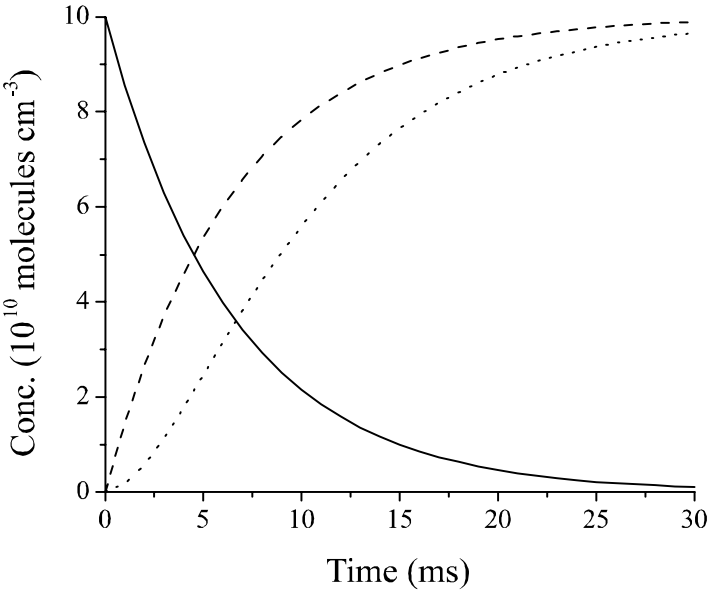

Figure 3-5: Titration scheme modeling results for the initial concentrations $[CH_4]_0 = 5\times10^{12}$, $[O_2]_0 = 5\times10^{14}$, $[CH_3O_2]_0 = 1\times10^{11}$, and $[NO]_0 = 2\times10^{13}$. All concentrations are given in molecules cm^{-3}. (—) = CH_3O_2, (– –) = NO_2, (··) = CH_3ONO.

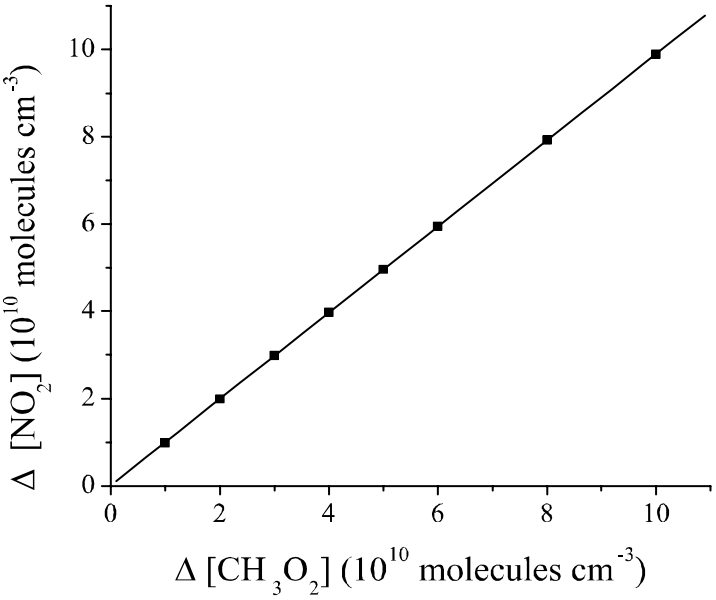

Figure 3-6: Model results showing the rise in $[NO_2]$ for a given decrease in $[CH_3O_2]$. The linear least-squares fit has a slope of 0.98.

Reaction	**Rate**[a]
$CH_3O_2 + NO \rightarrow CH_3O + NO_2$	7.7×10^{-12}
$CH_3O + NO \xrightarrow{M} CH_3ONO$	1.2×10^{-11}
$CH_3O_2 + CH_3O_2 \rightarrow CH_2O + CH_3OH + O_2$	2.8×10^{-13}
$CH_3O_2 + CH_3O_2 \rightarrow 2\ CH_3O + O_2$	1.4×10^{-13}
$CH_3O + O_2 \rightarrow CH_2O + HO_2$	1.9×10^{-15}
$CH_3O + NO_2 \xrightarrow{M} CH_3ONO_2$	1.3×10^{-11}
$HO_2 + NO \rightarrow OH + NO_2$	8.1×10^{-12}
$OH + NO \xrightarrow{M} HONO$	1.7×10^{-12}
$OH + NO_2 \xrightarrow{M} HNO_3$	3.4×10^{-12}
$OH + CH_4 \rightarrow H_2O + CH_3$	6.3×10^{-15}
$CH_3 + O_2 \xrightarrow{M} CH_3O_2$	4.8×10^{-13}

Table 3.3: Chemical reactions used in kinetic modeling. Rate constants are given for 100 Torr and 298 K and are in units of cm^3 $molecule^{-1}$ s^{-1}. [a][*DeMore et al.*, 1997]

cm^{-3}. The plot also shows that there is little, if any, excess NO_2 produced from side reactions in the flow tube. The model was run for a variety of CH_3O_2 concentrations and the change in NO_2 concentration was plotted as a function of the change in CH_3O_2 concentration. The concentrations of the other species in the flow tube were held constant. As seen in Figure 3-6, CH_3O_2 can be successfully titrated to NO_2 for these reaction conditions and no correction factor is needed as the slope of the least squares fit is approximately 1.

The titration was performed by varying the F_2 flow through the microwave discharge cavity to change the CH_3O_2 concentration in the flow tube. The CH_3^+ signal level was recorded and approximately 2×10^{13} molecules cm^{-3} of NO were added to the flow tube through the moveable injector. The NO_2 signal change was recorded and the discharge was turned off to record the background NO_2 signal coming from the NO sample or other sources. The NO_2 signal was then calibrated using an NO_2 sample of known concentration. Figure 3-7 shows a plot of the CH_3^+ signal vs. the change in NO_2 concentration. Based on the model results, no correction factor was needed for this titration, so the CH_3^+ signal level was multiplied by the

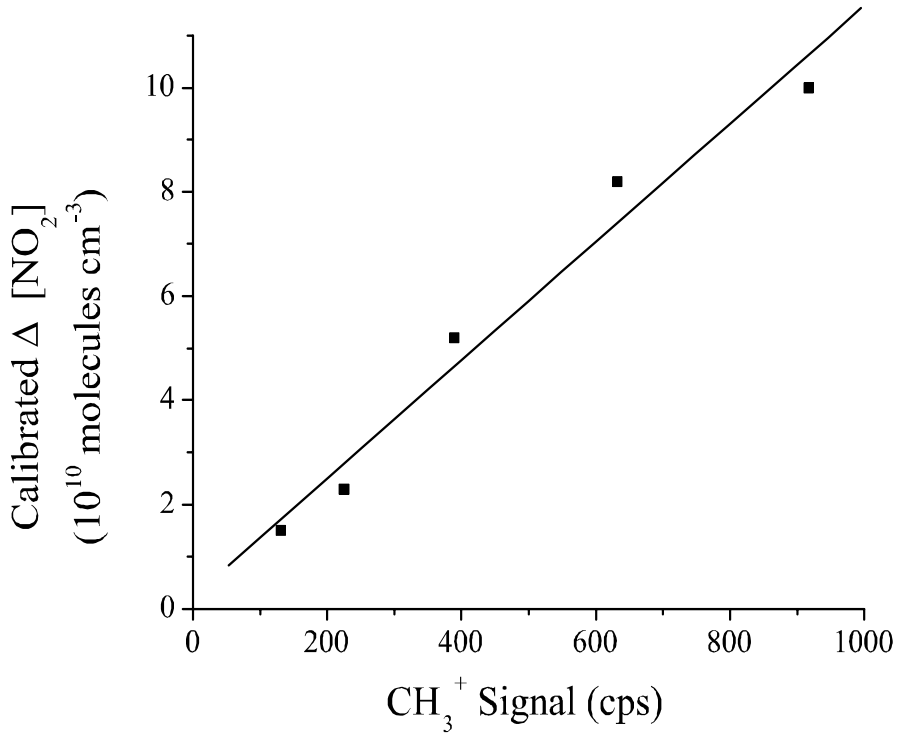

Figure 3-7: A sample CH_3O_2 titration curve. The slope of the linear least-squares fit gives the CH_3O_2 sensitivity (m = 1.1 $\times$ 10^8 molecules cm^{-3} cps^{-1}).

slope of the best fit line obtained in Figure 3-7 to obtain the CH_3O_2 concentration in the flow tube.

3.2.4 Results and discussion

Experiments were performed under pseudo-first order conditions with the CH_3O_2 concentration ranging from 5-10 $\times$ 10^{10} molecules cm^{-3} and NO concentrations ranging from 0.7-10 $\times$ 10^{12} molecules cm^{-3}. The NO mixing time was determined by injecting NO through the moveable injector without the microwave discharge cavity operating. The injector position and hence the residence time of the NO in the flow tube was changed so that the residence time ranged from 1-30 ms. The plot of the NO^+ signal as a function of injector distance is given in Figure 3-8.

The NO^+ signal is relatively flat until the residence time reaches about 5 ms as shown by the smoothed line through the data. The mixing time for the flow conditions used is approximately 5 ms. Based on these results, the reaction time range used for this experimental setup was

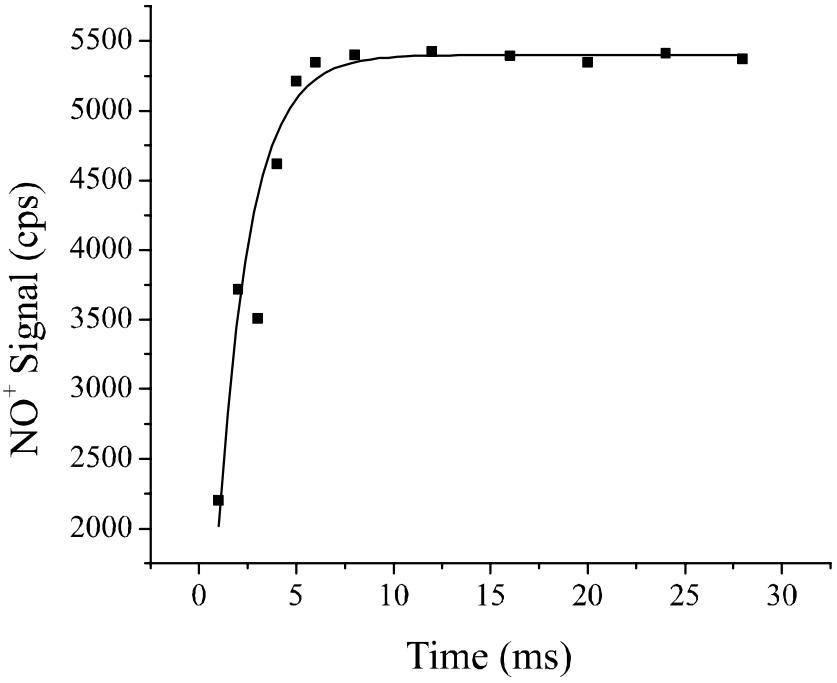

Figure 3-8: NO^+ signal as a function of injector distance or residence time in the flow tube.

8-28 ms.

CH_3O_2 decays were recorded as a function of reaction time and NO concentration for a range of NO concentrations. A sample pseudo-first order plot is given in Figure 3-9. Pseudo-first order decay rates (k_{1st}) were obtained by a non-linear exponential fit to the data. The pseudo-first order decay rates were plotted as a function of NO concentration and a linear least squares fit to this data yielded the second order rate coefficient (Figure 3-10).

The experiment was repeated several times and the second order rate coefficients and reaction conditions are summarized in Table 3.4.

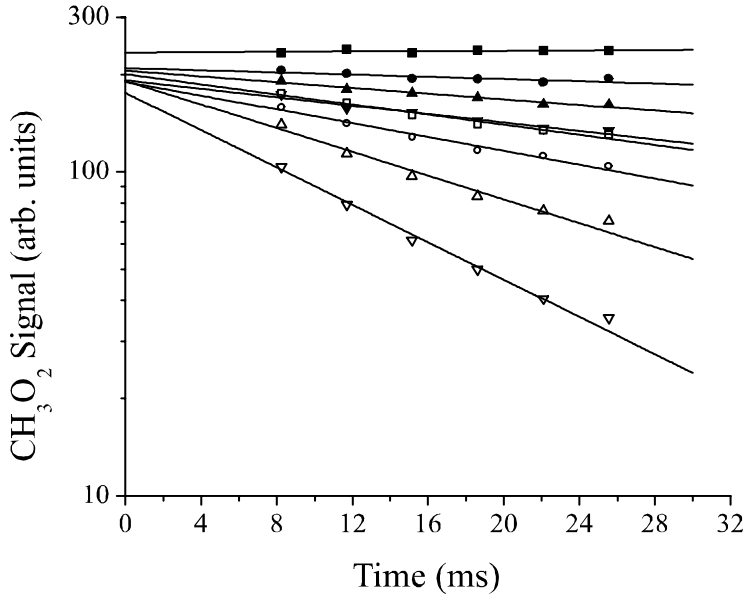

Figure 3-9: Pseudo-first order decays of CH_3^+ vs. reaction time with NO. Fits to each set of data yield k_{1st}. [NO] (10^{11} molecules cm^{-3}): (■) none, (●) 7.5, (▲) 13.6, (▼) 18.1, (□) 23.1, (○) 36.0, (△) 50.9, (▽) 78.1

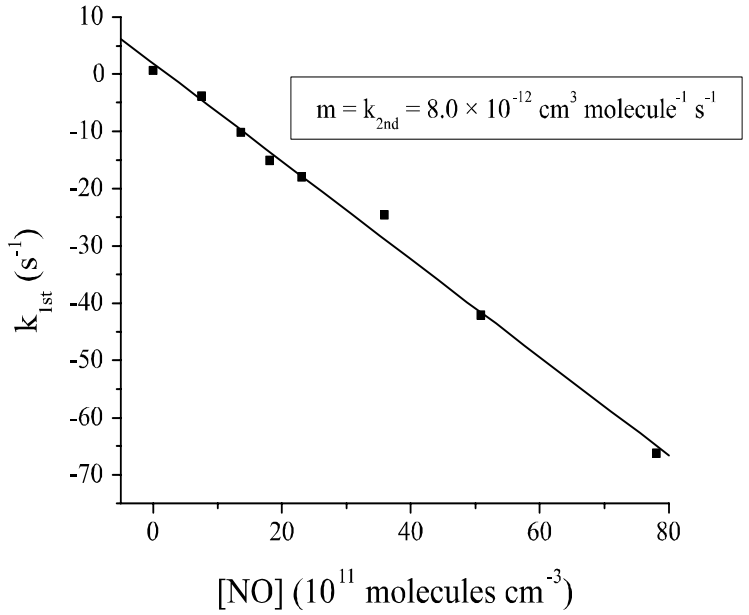

Figure 3-10: Pseudo-first order decay rate coefficients (k_{1st}) plotted as a function of [NO] concentration. Linear least-squares fit yields the second order rate coefficient ($k_{3.4}$).

Total Flow	**Temperature**	**Pressure**	$\mathbf{R}_e$	$\mathbf{k}_{3.4}$
(STP L min^{-1})	(K)	(Torr)	—	(cm^3 molecule s^{-1})
52100	298	99.9	3078	8.0×10^{-12}
53400	298	100	3155	6.2×10^{-12}
52600	298	100.3	3108	6.0×10^{-12}
				$(6.7 \pm 2.2) \times 10^{-12}$

Table 3.4: Experimental conditions and second order reaction rates for the CH_3O_2 + NO measurements.

The value of $(6.7 \pm 2.2) \times 10^{-12}$ cm^3 $molecule^{-1}$ s^{-1} represents the average with an error of 2σ and is not corrected for turbulent flow errors. The measured value for $k_{3.4}$ agrees with the current recommendation of 7.7×10^{-12} cm^3 $molecule^{-1}$ s^{-1} [*DeMore et al.*, 1997] within experimental error.

These experiments indicate that simple organic radicals such as CH_3O_2 can be detected with this CIMS technique and second order kinetic rate constants can be accurately measured. The CH_3O_2 + NO reaction was studied and the measured reaction rate agrees well with the literature recommendation. The success in measuring the reaction rate of a well known CH_3O_2 reaction motivates the study of other CH_3O_2 reaction rates.

3.3 CH_3O_2 + HO_2 Kinetics

3.3.1 Experimental setup

The basic flow tube setup used in this experiment was similar to that described in the previous section on CH_3O_2 + NO kinetics. CH_3O_2 was produced in the sidearm at the rear of the flow tube. HO_2 was produced in the moveable injector. The injector consisted of a $\frac{1}{4}$" o.d. alumina tube with a nested $\frac{1}{8}$" o.d. teflon tube running the length of the injector. A mixture of UHP He (3 STP L min^{-1}) and H_2 (0.1 STP cm^3 min^{-1}) was passed through a microwave

discharge cavity operating at 2.45 GHz and 40 W. The hydrogen atoms traveled the length of the injector inside the $\frac{1}{8}$" o.d. tteflon tube. UHP O_2 (2 STP cm^3 min^{-1}) was admitted into the back of the $\frac{1}{4}$" o.d. injector, but remained separate from the H atoms. The H atoms and O_2 were allowed to mix in the final 2 cm of the injector where >99% of the H atoms were converted to HO_2 through Reaction 3.24 ($k_{3.24} = 1.7 \times 10^{-13}$ cm^3 $molecule^{-1}$ s^{-1} at 298 K and 100 Torr).

$$H + O_2 \xrightarrow{M} HO_2 \tag{3.24}$$

This technique of HO_2 production has been used in the past [*Elrod et al.*, 1996] and is effective at reducing HO_2 self reaction and wall loss in the injector. CH_3O_2 was produced by a variety of methods (see section 3.3.4). The teflon turbulizer already described in detail was used to promote turbulent mixing of the reactants. Pressures in the flow tube and chemical ionization region were monitored with a capacitance manometer (MKS Beratron). A schematic of the basic setup is shown in Figure 3-11.

The main peroxy radical reactions occurring in the flow tube are given by Reactions 3.25-3.27.

$$CH_3O_2 + CH_3O_2 \longrightarrow Products \tag{3.25}$$

$$CH_3O_2 + HO_2 \longrightarrow CH_3OOH + O_2 \tag{3.26}$$

$$HO_2 + HO_2 \longrightarrow H_2O_2 + O_2 \tag{3.27}$$

The recommended rate constants for these reactions are $k_{3.25} = 4.7 \times 10^{-13}$ cm^3 $molecule^{-1}$ s^{-1}, $k_{3.26} = 5.6 \times 10^{-12}$ cm^3 $molecule^{-1}$ s^{-1} $k_{3.27} = 1.8 \times 10^{-12}$ cm^3 $molecule^{-1}$ s^{-1} [*DeMore*

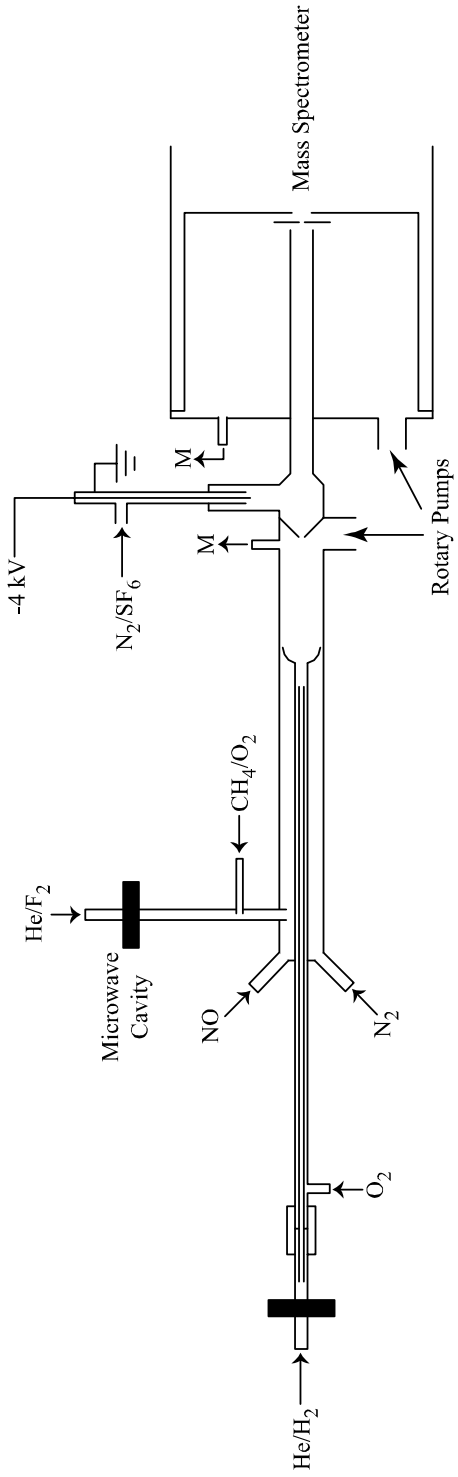

Figure 3-11: Experimental setup for the study of the reaction rate of CH_3O_2 + HO_2 at room temperature and 100 Torr. M=capacitance manometer.

et al., 1997]. There are a number of possible CIMS methods to determine the rate constant of Reaction 3.26. The first is to produce high concentrations of both reactants, leading to large radical decays and competition between the various reaction channels. This method requires simultaneous measurements of both radicals as well as titration methods to determine absolute radical concentrations. The time evolution of the absolute concentrations of both radicals is necessary in order to fit the multi-exponential decays using a chemical model. This method is complex and dependent on rate constants for all of the reactions occurring in the flow tube. Despite the fact that this method is not reliant on the absorption spectra of CH_3O_2 and HO_2, it offers little improvement over current methods for measuring $k_{3.26}$.

The second possible CIMS method is to work under pseudo-first order conditions. The preferable excess reagent in this experiment would be CH_3O_2 since the self reaction rate of CH_3O_2, $k_{3.25}$, is approximately a factor of 4 slower than the HO_2 self reaction rate, $k_{3.27}$. The concentration of HO_2 would be kept sufficiently low so that the self reaction was not important. The pseudo-first order decays of HO_2 would then be measured as a function of CH_3O_2 concentration. This would eliminate the need to titrate the HO_2 radical and would eliminate the necessity to model the flow tube chemistry to extract a rate constant. This method has several advantages over previous studies, namely the reaction rate determination is not dependent on complex chemical modeling and the measurement does not depend on ultraviolet cross-section data for HO_2 and CH_3O_2.

3.3.2 Modeling and titration

The titration of CH_3O_2 to determine the absolute concentration in the flow tube was accomplished using a method similar to that described in Section 3.2.3. NO was injected in the

rear of the flow tube in large concentrations ($>3 \times 10^{13}$ molecules cm^{-3}) and reacted with the CH_3O_2 to form NO_2 and CH_3ONO. The reaction set given in Table 3.3 was used to model the titration chemistry. Since CH_3O_2 was the excess reagent in this experiment, the calculation was extended to higher initial CH_3O_2 concentrations than in Section 3.2.3. A plot of the calculation results is given in Figure 3-12. This titration method remains linear up to CH_3O_2

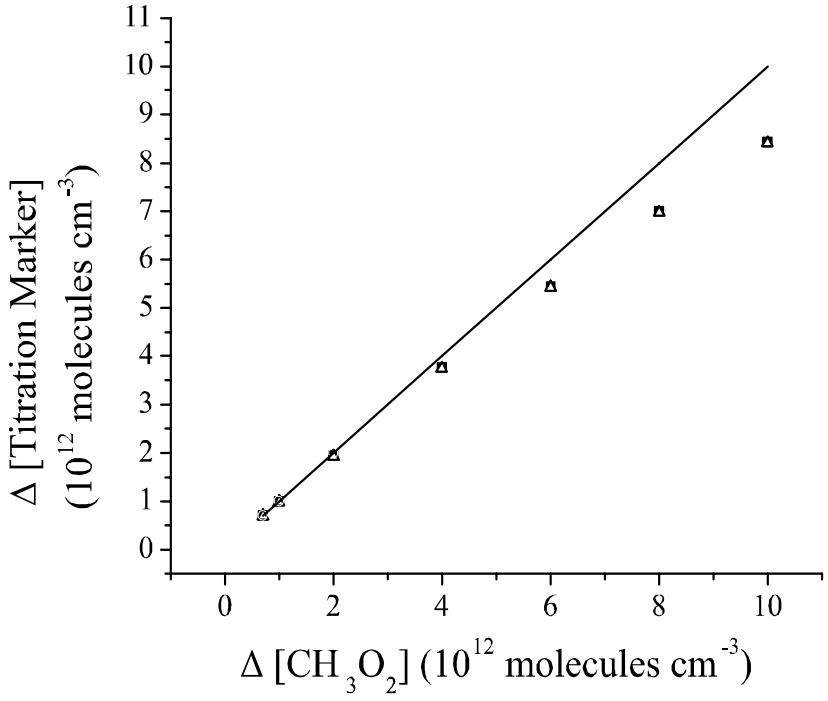

Figure 3-12: Modeling results for the titration of high concentrations of CH_3O_2 with NO. The solid line (—) represents unity conversion of CH_3O_2 to NO_2 or CH_3ONO. (■) = NO_2, (△) = CH_3ONO.

concentrations of $\sim 2 \times 10^{12}$ molecules cm^{-3}, but then begins to deviate. A 15% correction factor is needed at CH_3O_2 concentrations of 1×10^{13} molecules cm^{-3}. This is a reasonable correction factor which can be obtained by the model, therefore this titration method is viable up to high concentrations of CH_3O_2.

The chemistry in the flow tube must also be modeled to determine if any side reactions of either products or reactants will interfere with the pseudo-first order decays of HO_2. The reaction set used in the modeling of the flow tube chemistry is given in Table 3.5.

Reaction	**Rate**[a]
$CH_3O_2 + HO_2 \rightarrow CH_3OOH + O_2$	5.6×10^{-12}
$CH_3O + CH_3O_2 \rightarrow CH_3OOH + CH_2O$	2.6×10^{-12} [b]
$CH_3O_2 + CH_3O_2 \rightarrow CH_2O + CH_3OH + O_2$	2.8×10^{-13}
$CH_3O_2 + CH_3O_2 \rightarrow 2\ CH_3O + O_2$	1.4×10^{-13}
$CH_3O + O_2 \rightarrow CH_2O + HO_2$	1.9×10^{-15}
$HO_2 + HO_2 \xrightarrow{M} H_2O_2 + O_2$	1.6×10^{-13}
$HO_2 + HO_2 \rightarrow H_2O_2 + O_2$	1.7×10^{-12}
$CH_3O + CH_3O \rightarrow CH_2O + CH_3OH$	1.3×10^{-11} [c]
$CH_2O + HO_2 \xrightarrow{M}$ Adduct	5.0×10^{-14}

Table 3.5: Chemical reactions used in kinetic modeling. Rate constants are given for 100 Torr and 298 K and are in units of cm^3 molecule^{-1} s^{-1}. [a][*DeMore et al.*, 1997]. [b][*Heicklen*, 1988]. [c][*Biggs et al.*, 1997]

The major complication to note for the flowtube chemistry is that for high concentrations of CH_3O_2, the self reaction of CH_3O_2 will produce CH_3O radicals which can regenerate HO_2 through reaction with oxygen. Therefore, the oxygen concentration in the flow tube must be kept low enough to ensure that the fate of CH_3O is reaction with itself or CH_3O_2. The reaction kinetics were modeled for a variety of initial concentrations and the results are plotted in Figures 3-13 and 3-14. Initial concentrations of reactants used in the model were $[CH_3O_2]_0$ = variable, $[HO_2]_0 = 7.0 \times 10^{10}$ molecules cm^{-3}, and $[O_2]_0 = 3.0 \times 10^{14}$ molecules cm^{-3}.

The modeled HO_2 decays are well represented by pseudo-first order kinetics. The decays do become slightly non-linear at high CH_3O_2 concentrations on a semi-log scale as seen in Figure 3-13, however the deviation is minor. This non-linearity in the HO_2 decays is due to self reaction of CH_3O_2 at high initial CH_3O_2 concentrations resulting in losses of 25% in the $[CH_3O_2]$ over the reaction time modeled. The $[O_2]$ in the flow tube was held at $3.0 \times$

10^{14} molecules cm^{-3} for all model runs. At higher O_2 concentrations, HO_2 production due to side reactions in the flow tube became significant and led to large non-linearity in the HO_2 pseudo-first order decays. The pseudo-first order decay rates were plotted as a function of $[CH_3O_2]_{final}$ in Figure 3-14. The pseudo-first order decay rates were also plotted as a function of the initial and average CH_3O_2 concentrations in the flow tube. The linear least-squares fits to these data sets led to larger deviations from the rate coefficient used in the model for the $CH_3O_2 + HO_2$ reaction. This error is due to the greater sensitivity of the exponential fit to the HO_2 concentrations at long reaction times (28 ms). These HO_2 concentrations are represented more closely by the final $[CH_3O_2]$. The slope of the linear least-squares fit in Figure 3-14 has an error of approximately 4% from the modeled rate constant of 5.6×10^{-12} cm^3 $molecule^{-1}$ s^{-1} (Table 3.5). The errors in the fits using $[CH_3O_2]_0$ and $[CH_3O_2]_{avg}$ were 24% and 15% respectively.

These modeling studies predict that under sufficiently low O_2 concentrations, pseudo-first order kinetics will accurately represent the decay profiles of HO_2 and CH_3O_2 concentrations can be determined with small correction factors using a nitric oxide titration scheme. The pseudo-first order decay rates of HO_2 are also best represented by the CH_3O_2 concentrations at long reaction times.

3.3.3 Chemical ionization

HO_2 chemical ionization techniques using a variety of CI reagents have been described in the literature [*Elrod et al.*, 1996; *Seeley et al.*, 1996]. The two reaction schemes for detecting HO_2 are given in Reaction 3.28 and 3.29. The detection sensitivities for HO_2 using these two reagents have been compared [*Ivanov et al.*, 2001] and greater sensitivity to HO_2 can be

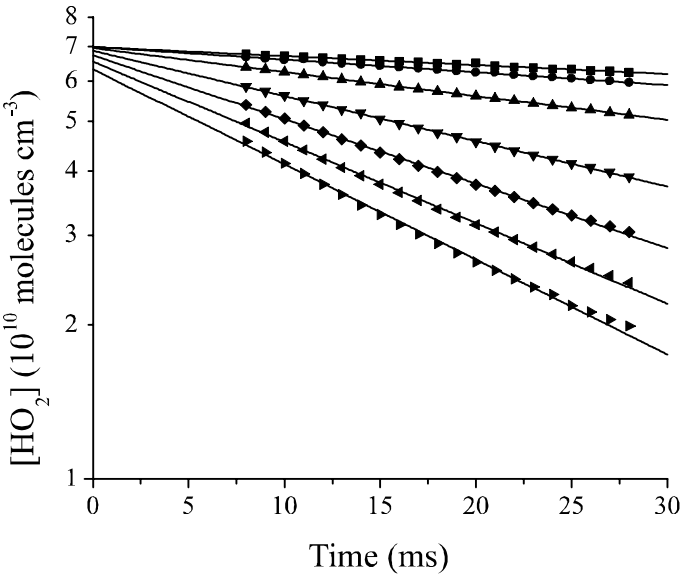

Figure 3-13: Pseudo-first order decays of HO_2 in the presence of various initial concentrations of CH_3O_2 ranging from 7×10^{11} molecules cm^{-3} (■) to 1×10^{13} molecules cm^{-3} (►). (—) represent exponential fits to the data.

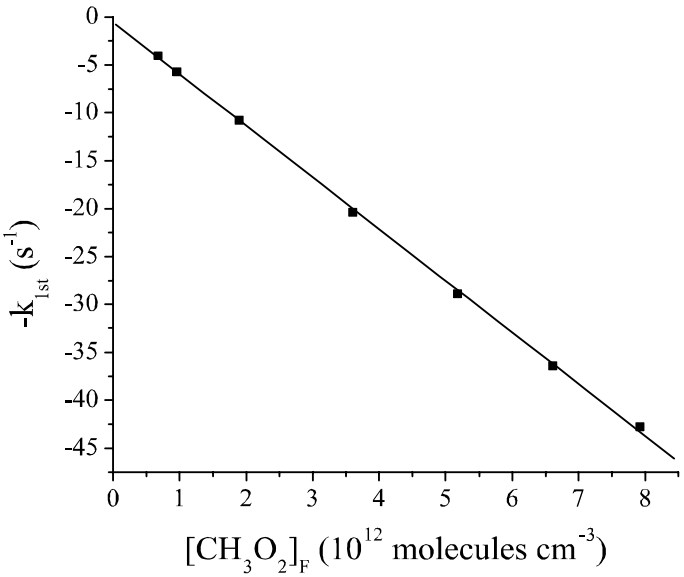

Figure 3-14: Plot of the pseudo-first order decay coefficients (k_{1st}) vs. $[CH_3O_2]_{final}$. (—) represents a linear least-squares fit to the data and has a slope of 5.38×10^{-12} cm^3 molecule^{-1} s^{-1}.

achieved by reaction with F^-.

$$F^- + HO_2 \longrightarrow HF + O_2^- \tag{3.28}$$

$$SF_6^- + HO_2 \longrightarrow SF_4O_2^- + Products \tag{3.29}$$

The reaction of HO_2 with SF_6^- is likely a complex multi-step reaction and proceeds with a slower overall rate constant [*Ivanov et al.*, 2001]. The detection of HO_2 using SF_6^- is also hindered by the interference of the reaction:

$$SF_6^- + H_2O_2 \longrightarrow SF_4O_2^- + Products \tag{3.30}$$

Significant concentrations of H_2O_2 can be produced in the HO_2 source (Reaction 3.27), so care must be taken to ensure that HO_2 concentrations are kept low enough to minimize self reactions of HO_2. These restrictions in the use of SF_6^- suggest that F^- is the reagent of choice for detecting HO_2.

CH_3O_2 has also been detected using various chemical ionization schemes [*Villalta et al.*, 1995; *Elrod et al.*, 2001]. Reactions 3.31-3.33 summarize the chemical ionization reactions of CH_3O_2:

$$F^- + CH_3O_2 \longrightarrow CH_3F + O_2^- \tag{3.31}$$

$$O_2^+ + CH_3O_2 \longrightarrow CH_3^+ + 2O_2\ (major) \tag{3.32}$$

$$H_3O^+ \cdot (H_2O)_n + CH_3O_2 \longrightarrow CH_3O_2H^+ \cdot (H_2O)_{n-1} + H_2O \tag{3.33}$$

Due to the fact that the product ion of both CH_3O_2 and HO_2 reaction with F^- is O_2^-, HO_2 can not be uniquely detected with F^- in the presence of CH_3O_2. SF_6^- is therefore the only viable option for the detection of HO_2 despite its limitations and lower sensitivity. Since the detection of HO_2 will be performed in negative ion mode, the titration of CH_3O_2 is more conveniently carried out in negative ion mode as well. The chemical ionization reactions of interest for the titration of CH_3O_2 are Reactions 3.34 and 3.35.

$$F^- + CH_3ONO \longrightarrow CH_3F + NO_2^- \tag{3.34}$$

$$SF_6^- + NO_2 \longrightarrow SF_6 + NO_2^- \tag{3.35}$$

Since both CH_3O_2 and CH_3ONO can be detected with F^-, this ionization scheme was chosen for the titration of CH_3O_2. There is no significant reaction of F^- with the titration coproduct NO_2, so there will be no interference from this ionization reaction channel.

3.3.4 CH_3O_2 radical source

In order to achieve significant HO_2 decay rates, high concentrations of CH_3O_2 must be produced (10^{12}-10^{13} molecules cm^{-3}). High instantaneous concentrations of CH_3O_2 ($>10^{14}$ molecules cm^{-3}) have been produced using flash photolysis [*Lightfoot et al.*, 1991], however the equipment required for flash photolysis was not available for this experiment. Flash photolysis is also not typically used to produce the steady state radical concentrations needed in this experiment. The most commonly used radical sources for flow tube experiments are microwave discharge sources and thermal decomposition sources [*Villalta et al.*, 1995; *Scholtens et al.*, 1999].

Absolute CH_3O_2 concentrations were determined by titrating the CH_3O_2 to CH_3ONO as

discussed previously. CH_3ONO was synthesized using the method of Rook [*Rook*, 1982]. Synthesis details are provided in Appendix A. CH_3ONO (b.p. -12°C) samples were stored in

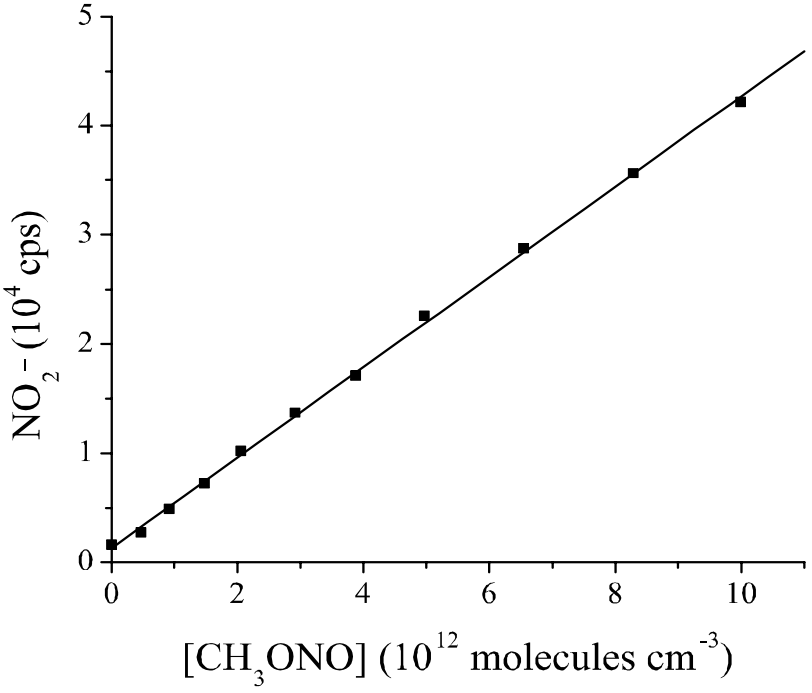

Figure 3-15: Calibration plot of CH_3ONO detected as NO_2^-. Linear least-squares fit (1/m) gives a sensitivity of 2.4×10^8 molecules cm^{-3} cps^{-1}.

an isopropanol-dry ice slush bath at -78°C. Purity was determined to be >99% by ultraviolet and infrared absorption analysis. Gas-phase samples were withdrawn from the stock and diluted with UHP N_2 to 2% mixtures in a passivated pyrex bulb. A sample calibration curve for CH_3ONO is plotted in Figure 3-15. The calibration is linear over the range of CH_3O_2 concentrations needed for this experiment.

Microwave discharge

The first CH_3O_2 source used was the microwave discharge source described in Section 3.2.1 and Reactions 3.12-3.14. A diagram of the sidearm is shown in Figure 3-16. Setup 1 was used for

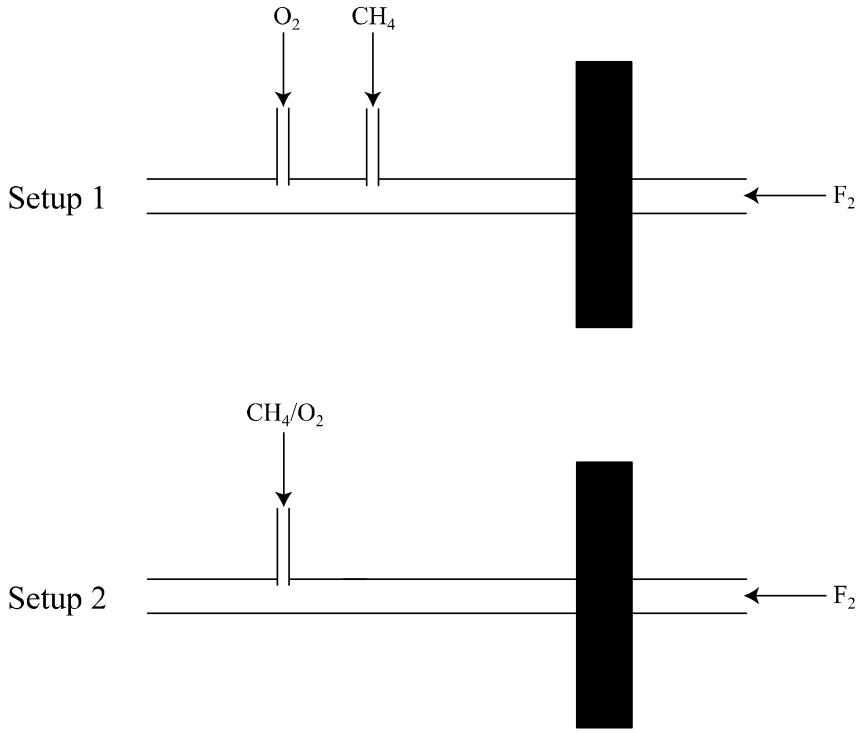

Figure 3-16: CH_3O_2 radical source designs utilizing a microwave discharge cavity.

the CH_3O_2 + NO experiment. It was capable of producing CH_3O_2 concentrations in the 10^{10} molecules cm^{-3} range. However, in these experiments where much higher concentrations were needed, adding more F_2 to the microwave discharge cavity flow did not significantly increase the CH_3O_2 signal. This is likely due to reactions of the methyl radicals in the 1 ms of reaction time before they are converted to CH_3O_2 by the O_2 flow ($k_{3.36} = 5.2 \times 10^{-11}$ cm^3 $molecule^{-1}$ s^{-1}) [*Fahr et al.*, 1991].

$$CH_3 + CH_3 \xrightarrow{M} C_2H_6 \tag{3.36}$$

The O_2 must therefore be present when the methyl radicals are formed so that the formation of CH_3O_2 will compete with the self reaction of the CH_3 radicals. The sidearm was modified so that the CH_4 and O_2 were added simultaneously (Figure 3-16, Setup 2). The CH_4 concentration in the sidearm must now be high enough to prevent the reaction

$$F + O_2 \xrightarrow{M} FO_2 \tag{3.37}$$

($k_{3.37} = 1.4 \times 10^{-14}$ cm^3 molecule^{-1} s^{-1} at 100 Torr) [*DeMore et al.*, 1997].

There were several difficulties with this radical production method. The first was that this source was only capable of producing CH_3O_2 concentrations up to 3×10^{12} molecules cm^{-3}. This was likely due to the fact that the oxygen concentration in the flow tube must be held below 3×10^{14} molecules cm^{-3}, constraining the oxygen concentration accessible in the sidearm. The methyl radical self-reaction loss was still significant at the maximum sidearm O_2 concentration. The second difficulty with this method was the interference of HF in the chemical ionization region. HF was produced in large concentrations ($>10^{13}$ molecules cm^{-3}) due to Reaction 3.13 and F atom reaction with the walls of the alumina tube. The SF_6^- reaction with HF has been studied numerous times [*Streit*, 1982; *Hanson & Ravishankara*, 1992], however no reaction has been measured. These measurements were done at low pressures which were not representative of the turbulent flow experiments. Under high pressure experimental conditions, the microwave discharge of F_2 in the presence of CH_4 led to complete conversion of the SF_6^- mass peak to a secondary peak (m/z = 59) at HF concentrations of $\sim 7 \times 10^{12}$ molecules cm^{-3}. This HF concentration is assumed based on complete conversion of F_2 to 2 HF molecules in the sidearm. This is a reasonable assumption due to the weak F_2 bond energy (159 kJ/mol) [*Lide*,

1990]. The mass peak at 59 amu was attributed to $F^- \cdot (HF)_2$ despite no previous evidence of a reaction between SF_6^- and HF. Smaller peaks were also seen at 39 and 79 amu. This surprising result could be due to reaction of SF_6^- with HF clusters in the gas phase rather than single HF molecules. These HF clusters may not be present at the low HF concentrations and low pressures used in other experiments. A control experiment was performed to try to decisively identify these peaks as $F^- \cdot (HF)_n$ ions. A small flow of water vapor was introduced in the sidearm in place of the CH_4/O_2 mixture. The reaction of F atoms with H_2O produced HF and OH according to Reaction 3.38

$$F + H_2O \longrightarrow HF + OH \tag{3.38}$$

($k_{3.38} = 1.4 \times 10^{-11}$ cm^3 molecule^{-1} s^{-1}) [*DeMore et al.*, 1997]. This reaction produced the same result as the CH_4/O_2 reaction, lending support for the identification of the mass peaks at 39, 59, and 79 amu as $F^- \cdot (HF)_n$ ions.

Since SF_6^- was used under experimental conditions to detect HO_2, this method of CH_3O_2 production was unacceptable. It was not able to produce the desired CH_3O_2 concentrations and significantly depleted the SF_6^- signal. Other microwave discharge sources were investigated, but none could be found in which the side products did not interfere with the flow tube or ionization chemistry.

Thermal source

A thermal source for this experiment must produce significant quantities of methyl radicals without any coproducts which would interfere with the flow tube or chemical ionization chem-

istry. Several thermal decomposition methyl radical sources have been previously used [*Villalta et al.*, 1995; *Heydtmann et al.*, 1992].

$$CH_3CH_2ONO \xrightarrow{\Delta} CH_3 + CH_2O + NO \tag{3.39}$$

$$CH_3NNCH_3 \xrightarrow{\Delta} 2CH_3 + N_2 \tag{3.40}$$

Reaction 3.39 could not be used due to the interference of the reaction of NO with the peroxy radicals of interest. Reaction 3.40 was promising due to the high yield of methyl radicals and the stable coproduct, N_2.

A stable azomethane complex ($CH_3NNCH_3 \cdot 2$ CuCl) was synthesized according to the method of Diels and Koll [*Diels & Koll*, 1925]. Synthesis details are given in Appendix B. The complex was stored in a darkened ampule at room temperature under 1 atm of UHP N_2. Gas-phase mixtures were made by placing a sample of the complex in a pyrex finger. The finger was evacuated and heated slowly to 125°C. Azomethane was liberated with small amounts of methane, ethane, and hydrogen, leaving the CuCl behind. The azomethane (f.p. -78°C) was collected in a passivated bulb at -80°C and the impurities were pumped away. This freeze pump thaw cycle was repeated and then the azomethane was diluted with UHP N_2. Azomethane purity was checked with ultraviolet and infrared absorption and was >99%.

The self reaction of the methyl radicals limited the production of CH_3O_2 due to the limitations on the oxygen concentration in the flow tube. The highest O_2 concentration that could be reached at 100 Torr in the sidearm was 7×10^{15} molecules cm^{-3}. The thermal source was designed as a high-pressure (1 atm) radical source. This design improvement had a number of benefits. First, for the same mixing ratios of oxygen in the sidearm the absolute concentration

is a factor of 7.6 higher, making the O_2 reaction with CH_3 more competitive with the self reaction. The increase in pressure also increases $k_{3.14}$ by a factor of 2 with no corresponding increase in $k_{3.36}$. Modeling of the sidearm chemistry suggests that these two improvement could lead to a factor of 5 increase in the CH_3O_2 production in the sidearm.

The initial thermal decomposition source design utilized a high-temperature oven (Lindberg 55035). Figure 3-17 shows a schematic of the design. A small flow (1 STP cm^3 min^{-1}) of the

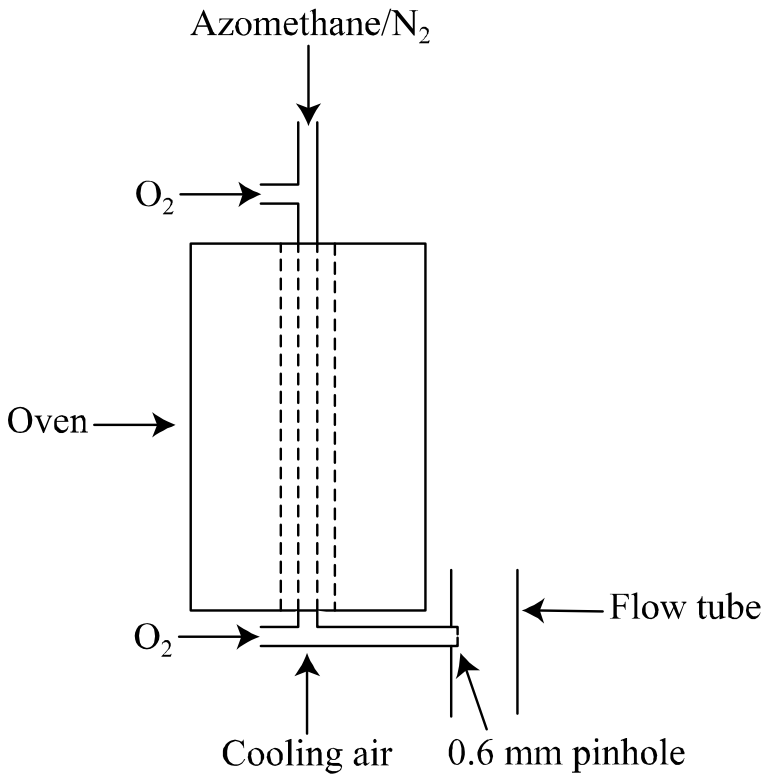

Figure 3-17: CH_3O_2 radical source based on high temperature thermal decomposition of azomethane.

azomethane/N_2 mixture was injected upstream of the oven with a large flow (3 STP L min^{-1}) of UHP N_2 as a carrier gas. Aflow of UHP O_2 (3 STP cm^3 min^{-1}) could be injected before or after the high temperature region producing O_2 concentrations of 3×10^{16} molecules cm^{-3} in

the sidearm region. The sidearm flow passed through a 600 μm pinhole and into the flow tube. Pressures in the sidearm ranged from 700-800 Torr depending on the carrier N_2 flow. A high flow of room temperature air was directed on the $\frac{1}{4}$" o.d. quartz tube downstream of the oven to cool the gas as it exited the oven. The temperature of the gas in the oven was measured as a function of distance to verify the precision of the temperature readout of the oven. Figure 3-18 shows the results of this calibration. A K-type thermocouple was inserted into the gas flow at various positions and allowed to equilibrate with the gas temperature. The oven set-point temperature is within 25 K of the maximum gas temperature for a set-point of 1073 K.

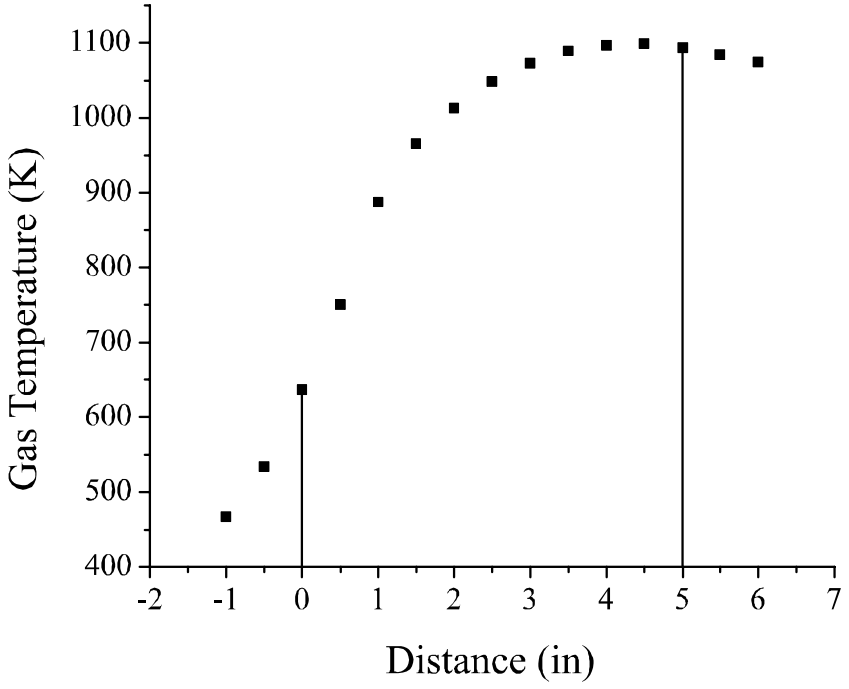

Figure 3-18: Temperature profile of the gas as a function of distance for an oven set point of 800°C. The drop lines represent the inlet and outlet of the oven with zero being the gas inlet.

The azomethane concentration in the flow tube could be monitored using O_2^+ as the ioniza-

tion reagent.

$$CH_3NNCH_3 + O_2^+ \longrightarrow CH_3NNCH_3^+ + O_2 \tag{3.41}$$

The azomethane signal began to decay at about 600 K and reached about 50% of its original concentration at a temperature of 675 K. Therefore, the oven temperature was set at 700 K. The oxygen was initially injected downstream of the oven. This configuration led to no measurable CH_3O_2 signal. This result was not unexpected as the high temperatures in the oven led to large methyl radical losses. Methyl radical reactions that were not important at room temperature became significant at high temperatures (Reactions 3.42 and 3.43).

$$CH_3 + CH_3 \longrightarrow C_2H_5 + H \tag{3.42}$$

$$CH_3 + CH_3 \longrightarrow C_2H_4 + H_2 \tag{3.43}$$

The methyl radicals produced in the oven were scavenged by the quartz walls and self-reactions before they were converted to CH_3O_2. The oxygen was then injected upstream of the oven so that the methyl radicals would preferentially react with O_2 rather than each other. This configuration also yielded no measurable CH_3O_2 signal. This was likely due to the relative stabilities of $(CH_3N)_2$ and CH_3O_2 at high temperatures. There is limited data on the unimolecular dissociation rate of CH_3O_2 at high temperatures, however the available data suggests that the decomposition rate of CH_3O_2 is faster than azomethane as seen in Figure 3-19. The methyl radicals were again lost due to self-reactions and wall loss even in the presence of high concentrations of O_2.

It was necessary to design a radical source in which the azomethane was quickly heated

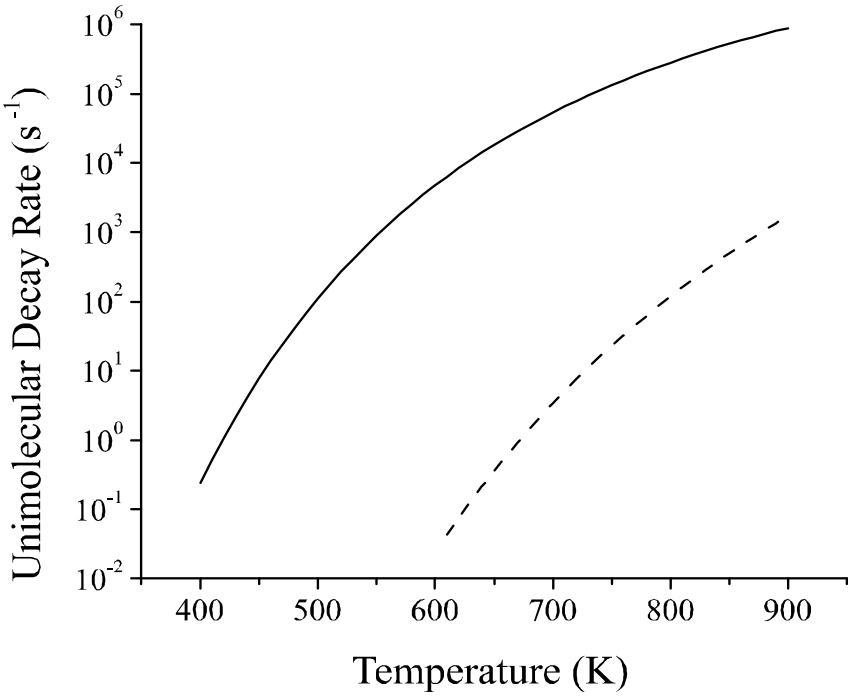

Figure 3-19: Unimolecular decay rates of $(CH_3N)_2$ (- -) and CH_3O_2 (—) over a range of temperatures [*Du & Hessler*, 1996; *Tsang & Hampson*, 1986].

to temperatures near 700-800 K and then quickly quenched to temperatures of <400 K in the presence of O_2 before the methyl radicals could be lost to self-reaction. One design employed for this purpose is shown in Figure 3-20. A small flow (100 STP cm^3 min^{-1}) of an azomethane/N_2 mixture was passed over the nichrome wire coil located on the inside of a $\frac{1}{8}$" o.d. alumina tube. The residence time of the azomethane in the heated region was less than 1 ms. A large sheath flow of 3 STP L min^{-1} of UHP N_2 and 3 STP cm^3 min^{-1} of UHP O_2 was passed over the end of the alumina tube. A large flow of room temperature air was directed at the $\frac{1}{4}$" o.d. pyrex tube to help cool the gas. The gas mixture then expanded through a 600 μm pinhole into the flow tube. A variable power AC supply was used to control the voltage on the nichrome wire.

The azomethane concentration in the flow tube was monitored using O_2^+. The $CH_3NNCH_3^+$

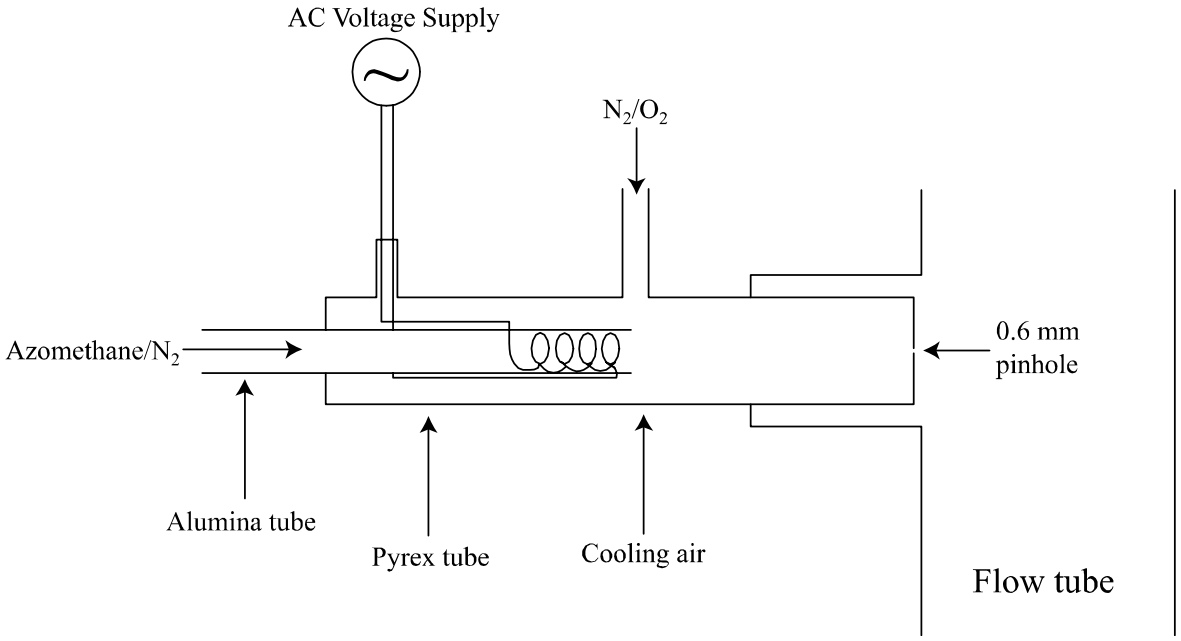

Figure 3-20: CH_3O_2 source utilizing a nichrome wire for decomposition of azomethane.

signal was measured as a function of voltage applied to the nichrome wire to determine if sufficient temperatures could be reached to decompose the azomethane. The nichrome wire failed in all cases before any measurable decomposition occurred. If there was no oxygen added to the sheath flow, higher voltages could be applied to the wire before it failed, however no decomposition was seen. The oxygen in the sheath flow may have oxidized the nichrome wire and caused it to fail more quickly at high temperatures.

Thermal decomposition of azomethane is a useful methyl radical source in many applications, however the decomposition of azomethane is often followed by expansion and rapid cooling of the gas to prevent methyl radical self reaction [*Peng et al.*, 1992]. It proved to be too difficult to adapt this technique of radical production to the experimental conditions required.

3.3.5 Conclusions

The reaction of CH_3O_2 with HO_2 can theoretically be studied under pseudo-first order conditions using chemical ionization mass spectrometry. The development of a CH_3O_2 radical source capable of producing concentrations in the 10^{12}-10^{13} molecules cm^{-3} range remains the largest obstacle in performing this experiment. A clever thermal source or photolytic source of methyl radicals holds the greatest promise in this regard. Photolysis of an azomethane/O_2 mixture with an excimer laser at 193 nm would yield high CH_3 concentrations and hence potentially large CH_3O_2 concentrations. A laser source would be needed to produce the photon flux necessary for efficient photolysis. Unfortunately, an excimer laser was not readily available, so a photolysis source could not be used. Another potential obstacle in studying this reaction with the CIMS technique is that the concentrations of H_2O_2 and O_2 must be kept low in the flow tube so that HO_2 is not regenerated through side reactions with oxygen and so that the detection of HO_2 is not complicated by the presence of H_2O_2.

3.4 Conclusions

The reactions of peroxy radicals are important for the cycling of radicals in the atmosphere. CIMS techniques have been used to detect RO_2 radicals and reaction rates have also been measured for several RO_2 reactions, including CH_3O_2 + NO. This reaction rate was measured with the UTI 100C precision mass analyzer coupled to a turbulent flow reactor. The measured rate coefficient of $(6.7 \pm 2.2) \times 10^{-12}$ cm^3 $molecule^{-1}$ s^{-1} agrees well with the recommended value. The uncertainty in the CH_3O_2 + HO_2 reaction rate could not be improved due to difficulty in producing the large amounts of CH_3O_2 needed to measure this reaction.

Appendix A: Synthesis of CH_3ONO

Synthesis of CH_3ONO:

1. Charge a 500-ml round bottom flask with 100 ml of deionized water (H_2O).
2. Add 25 ml reagent grade methanol (CH_3OH) to the round bottom flask.
3. Add a mixture of 25 ml conc. sulfuric acid (H_2SO_4) and 25 ml nitrosyl sulfuric acid (HO_3SONO) to the addition funnel.
4. Stir the contents of the flask and purge with He for 15 minutes.
5. Place the round bottom flask in a 25°C water bath.
6. Immerse cold trap in liquid nitrogen (77 K).
7. Add contents of additional funnel dropwise over 30 minutes with stirring and He slowly flowing.
8. Product vapors are collected in the cold trap for an additional 15 minutes with He flowing.
9. Remove the cold trap and close to the atmosphere.

Distillation of CH_3ONO:

1. Connect the cold trap and an evacuated cold finger to the vacuum line.
2. Pump on the cold trap at 77 K for 5 minutes.
3. Place the cold trap in a isopropanol-dry ice slush bath at 195 K.
4. Place the cold finger in liquid nitrogen at 77 K.
5. Distill the CH_3ONO to the cold finger with very slow pumping to remove any non-condensables.
6. Discard the fraction remaining in the cold trap at 195 K.

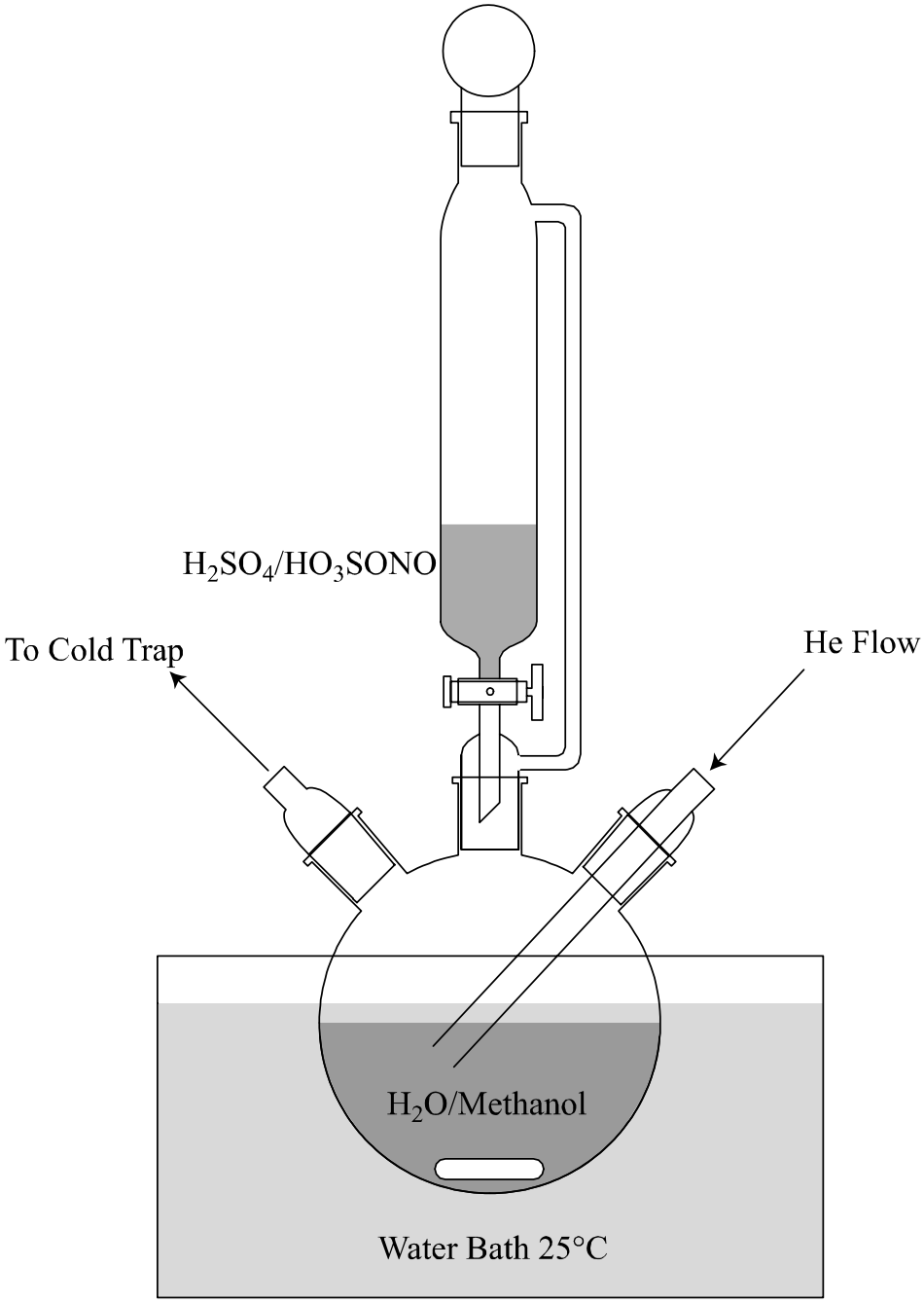

Figure 3-21: Setup for the synthesis of methyl nitrite (CH_3ONO).

7. Distill the CH_3ONO several more times from 195 to 77 K.
8. The product should be a glassy green solid at 77 K and a greenish-yellow liquid at 195 K.

Storage of CH_3ONO:

1. Store in a darkened cold finger at 195 K.
2. Vapor pressure at 200 K is 19.8 Torr [*Rook*, 1982].

Appendix B: Synthesis of CH_3NNCH_3

Synthesis of $CH_3NNCH_3 \cdot 2CuCl$:

1. Charge a 500-ml round bottom flask with 50 ml of deionized water (H_2O).
2. Add ∼10 g dimethylhydrazine dihydrochloride ($CH_3NHNHCH_3 \cdot 2HCl$) to the round bottom flask.
3. Add 100 ml of a 2.5M sodium acetate (CH_3CO_2Na) solution.
4. Make a mixture of ∼20 g anhydrous copper(II) chloride ($CuCl_2$) in enough deionized water to dissolve it all and add the mixture to the addition funnel.
5. Stir the contents of the flask, heat to 40°C and purge with N_2 for 15 minutes.
6. Add the contents of the addition funnel dropwise over 1 hour, maintaining the reaction temperature at 40°C.
7. Filter the contents of the round bottom flask in a Buchner funnel.
8. Wash the rusty-orange crystals with copious amounts of deionized water.
9. Wash the crystals with acetone, methanol and deionized water again.
10. Dry the crystals under suction with the Buchner funnel until the are dry enough to be transferred to an ampule.
11. Dry the crystals in the ampule under vacuum until they reach a constant mass.

Storage of $CH_3NNCH_3 \cdot 2CuCl$:

1. Store in a darkened ampule under 1 atm of N_2 at room temperature.

Liberation of CH_3NNCH_3:

1. Transfer a sample of azomethane to another ampule.
2. Attach the ampule and an evacuated bulb with a cold finger to the vacuum line.

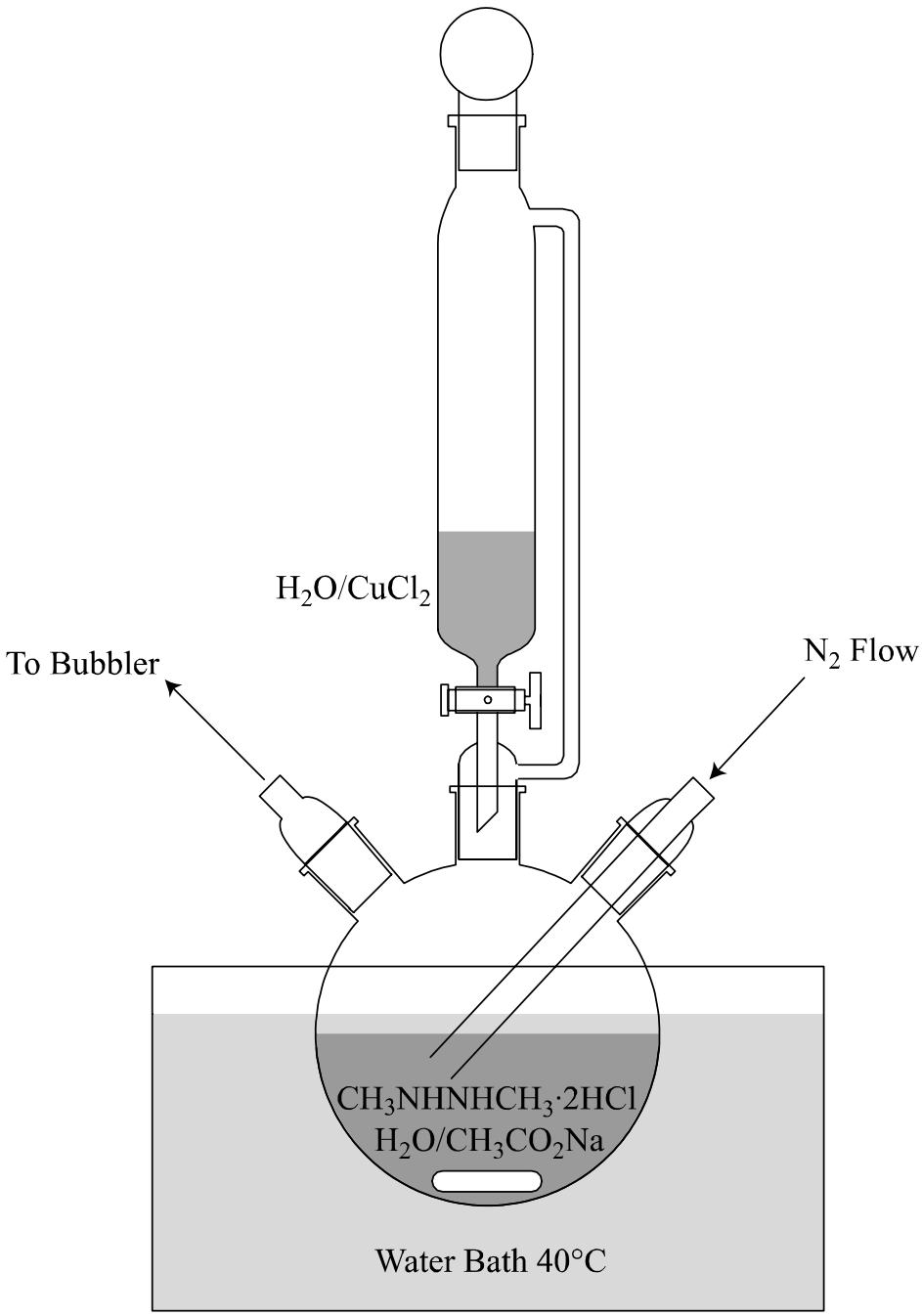

Figure 3-22: Setup for the synthesis of azomethane (CH_3NNCH_3).

3. Evacuate the ampule containing the azomethane complex.
4. Heat the ampule slowly in a silicon oil bath until the azomethane begins to be liberated ($\sim$125°C).
5. Immerse the cold finger of the evacuated bulb in an isopropanol-dry ice slush bath at -80°C.
6. Transfer the azomethane from the ampule to the cold finger.
7. Close the ampule and pump on the azomethane in the cold finger for 5 minutes at -80°C.
8. Make a gas-phase mixture of azomethane immediately, do not store pure azomethane as it is explosive.

References for Chapter 3

Biggs, P., C.E. Canosa-Mas, J.-M. Fracheboud, D.E. Shallcross, and R.P. Wayne, Kinetics of the reaction of F atoms with CH_3ONO and CH_3O, and the reaction of CH_3O with a number of hydrocarbons, *J. Chem. Soc. Faraday Trans.,* **93**, 2481-2486, 1997.

Cox, R.A. and G.S. Tyndall, Rate constants for reactions of CH_3O_2 in the gas phase, *Chem. Phys. Lett.*, **65**, 357-360, 1979.

Cox, R.A. and G.S. Tyndall, Rate constants for reactions of CH_3O_2 with HO_2, NO, and NO_2 using molecular modulation spectrometry, *J. Chem. Soc. Faraday Trans. 2,* **76**, 153-163, 1980.

Dagaut, P., T.J. Wallington, and M.J. Kurylo, Temperature dependence of the rate constant for the HO_2 + CH_3O_2 gas-phase reaction, *J. Phys. Chem.,* **92**, 3833-3836, 1988.

DeMore, W.B., S.P. Sander, C.J. Howard, A.R. Ravishankara, D.M. Golden, C.E. Kolb, R.F. Hampson, M.J. Kurylo, and M.J. Molina, *Chemical Kinetics and Photochemical Data for Use in Stratospheric Modeling*, JPL Publication 97-4, Jet Propulsion Laboratory, Pasadena, CA, 1997.

Diels, O. and W. Koll, Über Cuprohalogenid-Molekülverbindungen der Azokörper, *Ann.*, **443**, 262-273, 1925.

Du, H. and J.P. Hessler, Recombination of methyl radicals. 1. New data between 1175 and 1750 K in the falloff region, *J. Phys. Chem.*, **100**, 974-983, 1996.

Elrod, M.J., R.F. Meads, J.B. Lipson, J.V. Seeley, and M.J. Molina, Temperature dependence of the rate constant for the HO_2 + BrO reaction, *J. Phys. Chem.*, **100**, 5808-5812, 1996.

Elrod, M.J., D.L. Ranschaert, and N.J. Schneider, Direct kinetics study of the temperature dependence of the CH_2O branching channel for the CH_3O_2 + HO_2 reaction, *Int. J. Chem. Kinet.*, **33**, 363-376, 2001.

Fahr, A., A. Laufer, R. Klein, and W. Braun, Reaction rate determinations of vinyl radical reactions with vinyl, methyl, and hydrogen atoms, *J. Phys. Chem.*, **95**, 3218-3224, 1991.

Finlayson-Pitts, B.J. and J.N. Pitts, Jr., *Chemistry of the Upper and Lower Atmosphere*, Academic Press, San Diego, 2000, pp. 595.

Hanson, D.R. and A.R. Ravishankara, Heterogeneous chemistry of HBr and HF, *J. Phys. Chem.*, **96**, 9441-9446, 1992.

Heicklen, J., The decomposition of alkyl nitrites and the reactions of alkoxyl radicals, *Adv. Photochem.*, **14**, 177, 1988.

Heydtmann, H., D. Boglu, and J.J. Sloan, Development of a methyl radical source for use in reaction dynamics studies, *Chemical Physics*, **168**, 293-300, 1992.

Ivanov, A.V., A.K. Bertram, S.I. Trakhtenberg, L.T. Molina, and M.J. Molina, Hetergeneous interaction of HO_2 radicals with organic surfaces of tropospheric interest, manuscript in preparation, private communication, 2001.

Jenkin, M.E., R.A. Cox, G.D. Hayman, and L.J. Whyte, Kinetic study of the reactions CH_3O_2 + CH_3O_2 and CH_3O_2 + HO_2 using molecular modulation spectroscopy, *J. Chem. Soc. Faraday Trans. 2,* **84**, 913-930, 1988.

Kan, C.S., J.G. Calvert, and J.H. Shaw, Reactive channels of the CH_3O_2-CH_3O_2 reaction, *J. Phys. Chem.*, **84**, 3411-3417, 1980.

Kurylo, M.J., P. Dagaut, T.J. Wallington, and D.M. Neuman, Kinetic measurements of the gas phase HO_2 + CH_3O_2 cross-disproportionation reaction at 298 K, *Chem. Phys. Lett.*, **139**, 513-518, 1987.

Lide, D.R., *CRC Handbook of Chemistry and Physics*, 71st Ed., CRC Press, Boca Raton, 1990.

Lightfoot, P.D., V. Veyret, and R. Lesclaux, Flash photolysis study of the CH_3O_2 + HO_2 reaction between 248 and 573 K, *J. Phys. Chem.*, **94**, 708-714, 1990.

Lightfoot, P.D., P. Roussel, F. Caralp, and R. Lesclaux, Flash Photolysis study of the CH_3O_2 + CH_3O_2 and CH_3O_2 + HO_2 reactions between 600 and 719 K: unimolecular decomposition of methylhydroperoxide, *J. Chem. Soc. Faraday Trans.,* **87**, 3213-3220, 1991.

Masaki, A., S. Tsunashima, and N. Washida, Rate constant for the reaction of CH_3O_2 with NO, *Chem. Phys. Lett.*, **218**, 523-528, 1994.

McAdam, K, B. Veyret, and R. Lesclaux, UV absorption spectra of HO_2 and CH_3O_2 radicals and the kinetics of their mutual reactions at 298 K, *Chem. Phys. Lett.*, **133**, 39-44, 1987.

Moortgat, G.R., R.A. Cox, G. Schuster, J.P. Burrows, and G.S. Tyndall, Peroxy radical reactions in the photo-oxidation of CH_3CHO, *J. Chem. Soc. Faraday Trans. 2,* **85**, 809-829, 1989.

Peng, X.D., R. Viswanathan, G.H. Smudde, and P.C. Stair, A methyl free-radical source for use in surface studies, *Review of Scientific Instruments*, **63**, 3930-3935, 1992.

Plumb, I.C., K.R. Ryan, J.R. Steven, and M.F.R. Mulcahy, Rate coefficient for the reaction of CH_3O_2 with NO at 295 K, *J. Phys. Chem.*, **85**, 3136-3138, 1981.

Ravishankara, A.R., F.L. Eisele, N.M. Kreutter, and P.H. Wine, Kinetics of the reaction

of CH_3O_2 with NO, *J. Chem. Phys.*, **74**, 2267–2274, 1981.

Rook, F.L., Preparation, vapor pressure, and infrared spectrum of methyl nitrite, *J. Chem. Eng. Data*, **27**, 72-73, 1982.

Sander, S.P. and R.T. Watson, Kinetics studies of the reactions of CH_3O_2 with NO, NO_2, and CH_3O_2 at 298 K, *J. Phys. Chem.*, **84**, 1664-1674, 1980.

Scholtens, K.W., B.M. Messer, C.D. Cappa, and M.J. Elrod, Kinetics of the CH_3O_2 + NO reaction: temperature dependence of the overall rate constant and an improved upper limit for the CH_3ONO_2 branching channel, *J. Phys. Chem. A*, **103**, 4378-4384, 1999.

Seeley, J.V., *Experimental Studies of Gas Phase Reactions Using the Turbulent Flow Tube Technique*, Ph.D. Thesis, Massachusetts Institute of Technology, 1994.

Seeley, J.V., R.F. Meads, M.J. Elrod, and M.J. Molina, Temperature and pressure dependence of the rate constant for the HO_2 + NO reaction, *J. Phys. Chem.*, **100**, 4026-4031, 1996.

Simonaitis, R. and J. Heicklen, Rate coefficient for the reaction of CH_3O_2 with NO from 218 to 365 K, *J. Phys. Chem.*, **85**, 2946-2949, 1981.

Streit, G.E., Negative ion chemistry and the electron affinity of SF_6, *J. Chem. Phys.*, **77**, 826-833, 1982.

Tsang, W. and R.F. Hampson, Chemical kinetic data base for combustion chemistry. Part I. Methane and related compounds, *J. Phys. Chem. Ref. Data*, **15**, 1087-1279, 1986.

Tyndall, G.S., R.A. Cox, C. Granier, R. Lesclaux, G.K. Moortgat, M.J. Pilling, A.R. Ravishankara, and T.J. Wallington, Atmospheric chemistry of small organic peroxy radicals, *J. Geophys. Res.*, **106**, 12157-12182, 2001.

Villalta, P.W., L.G. Huey, and C.J. Howard, A temperature-dependent kinetics study of the CH_3O_2 + NO reaction using chemical ionization mass spectrometry, *J. Phys. Chem.*, **99**, 12829-12834, 1995.

Wallington, T.J. and S.M. Japar, Reaction of CH_3O_2 + HO_2 in air at 295 K: a product study, *Chem. Phys. Lett.*, **167**, 513-518, 1990.

Wallington, T.J., Fourier-transform infrared product study of the reaction of CH_3O_2 + HO_2 over the pressure range 15-700 Torr at 295 K, *J. Chem. Soc. Faraday Trans.,* **87**, 2379-2382, 1991.

Zellner, R., B. Fritz, and K. Lorenz, Methoxy formation in the reaction of CH_3O_2 radicals with NO, *Journal of Atmospheric Chemistry*, 241-251, 1986.

Chapter 4

Atmospheric Oxidation of Toluene

4.1 Introduction

The oxidation of aromatic compounds play a very important role in the chemistry of the troposphere. Aromatics such as benzene, toluene and the xylenes are produced in significant concentrations in many urban areas, with measured concentrations reaching 40 ppb [*Jing et al.*, 2001; *Zielinska & Fujita*, 1994]. The rates for the reaction of aromatic compounds with OH range from 1.23×10^{-12} cm^3 molecule^{-1} s^{-1} for benzene to 5.75×10^{-11} cm^3 molecule^{-1} s^{-1} for a more highly substituted aromatic such as 1,3,5-trimethylbenzene [*Atkinson*, 1994]. These rate constants correspond to tropospheric lifetimes with respect to OH in the range of hours to weeks. These relatively short lifetimes compounded with the significant concentrations in the troposphere indicate the importance of the chemistry of aromatic compounds, especially in urban air masses both near the source and as the air mass ages. Many aromatics and their oxygenated or nitrated derivatives have significant human health effects as well, making our understanding of the chemistry of these compounds vital.

Toluene is generally the most abundant aromatic VOC in the troposphere. The sources of toluene are dominantly anthropogenic in nature [*Karl et al.*, 2001]. Toluene is a major component of gasoline and is present in tailpipe emissions, and is also widely used in industrial applications. The reactions of toluene with a number of atmospheric oxidants are given below:

$$C_7H_8 + OH \longrightarrow Products \tag{4.1}$$

$$C_7H_8 + NO_3 \longrightarrow Products \tag{4.2}$$

$$C_7H_8 + O_3 \longrightarrow Products \tag{4.3}$$

$$C_7H_8 + O(^3P) \longrightarrow Products \tag{4.4}$$

($k_{4.1} = 5.96 \times 10^{-12}$ cm^3 molecule^{-1} s^{-1}), ($k_{4.2} = 6.8 \times 10^{-17}$ cm^3 molecule^{-1} s^{-1}), ($k_{4.3} < 10^{-20}$ cm^3 molecule^{-1} s^{-1}), ($k_{4.4} = 7.6 \times 10^{-14}$ cm^3 molecule^{-1} s^{-1}) [*Atkinson*, 1994; *Baulch*, 1992]. Clearly, the dominant atmospheric loss process for toluene is reaction with OH. Nighttime oxidation of toluene by NO_3 is of only very minor importance.

The atmospheric oxidation mechanisms of aromatic compounds such as toluene are not well understood at this time [*Atkinson*, 1994]. There have been many smog chamber and product studies which have identified oxidation products and attempted to elucidate mechanisms, however many stable products can be formed through multiple reaction pathways [*Atkinson et al.*, 1989; *Volkamer et al.*, 2001; *Tuazon et al.*, 1986; *Atkinson & Aschmann*, 1994]. Direct detection of radical intermediates and kinetic measurements of elementary steps in these mechanisms are needed in order to validate and improve the current proposed oxidation mechanisms. A small portion of the currently proposed atmospherically relevant oxidation mechanism is shown in Figure 4-1.

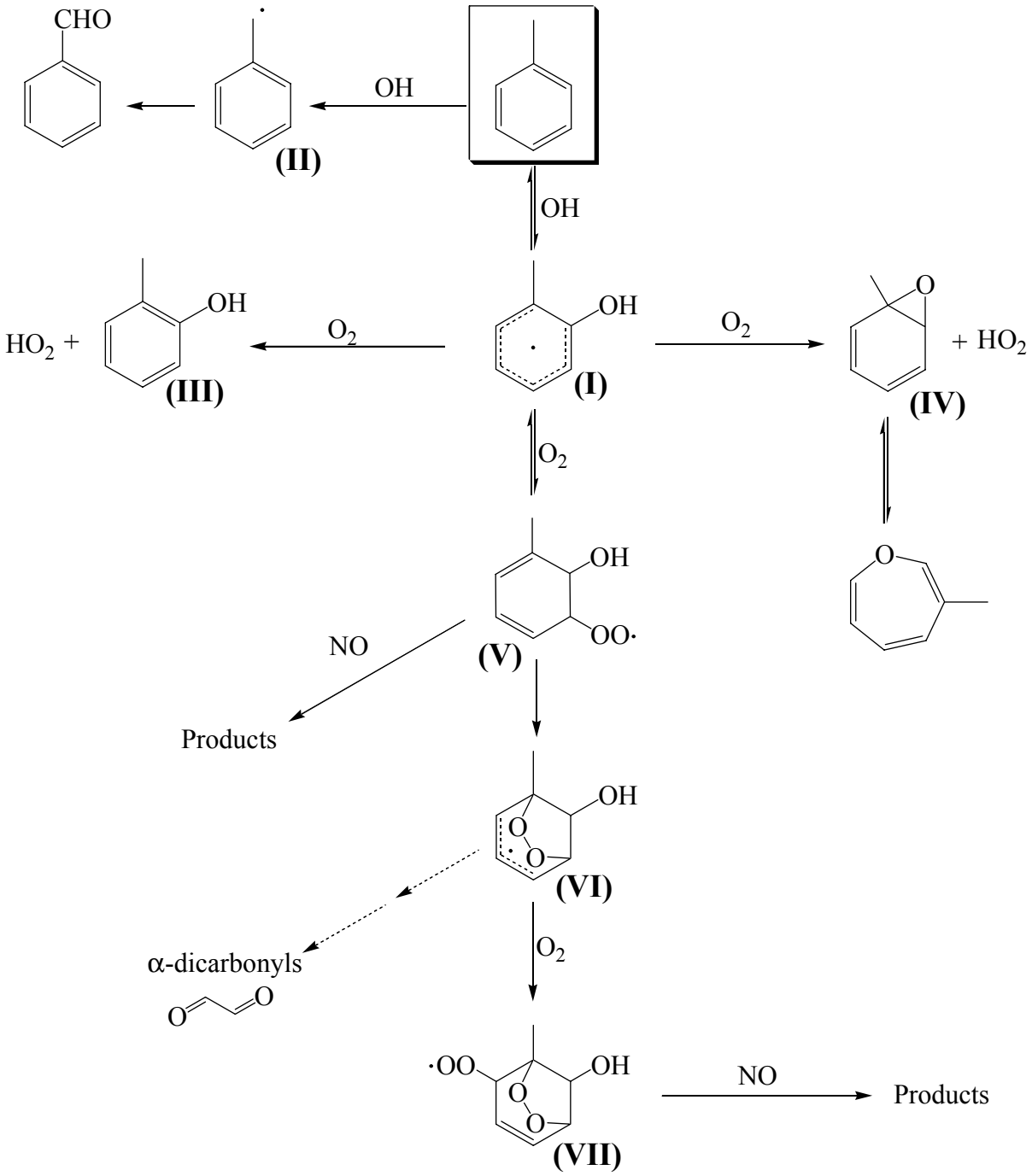

Figure 4-1: Diagram of the basic currently proposed mechanism for the atmospheric oxidation of toluene. Toluene is highlighted at the top of the figure.

The oxidation is initiated by a multi-channel reaction with OH to form a benzyl radical (II) or the methylhydroxycyclohexadienyl radical (I), referred to as the adduct after this point. The figure does not include all possible adduct isomers for simplicity. The current recommendation for the branching ratio of this reaction to form the adduct is 0.88 [*Atkinson*, 1994]. The benzyl radical reacts like a typical alkyl radical and forms benzaldehydein a mechanism similar to that of the formation of formaldehyde in the oxidation of methane. The reaction to form the adduct is reversible, with a decomposition rate of 4 s^{-1} at 298 K [*Atkinson*, 1994]. Few direct observations of the adduct have been made, but the studies to date suggest that the atmospheric fate of the adduct is reaction with O_2 [*Bohn*, 2001]. The proposed reactions of the adduct are as follows

$$Adduct + O_2 \longrightarrow Products \tag{4.5}$$

$$Adduct + NO_2 \longrightarrow Products \tag{4.6}$$

$$Adduct + NO \longrightarrow Products \tag{4.7}$$

with rate constants of $k_{4.5} = 5.4 \times 10^{-16}$ cm^3 $molecule^{-1}$ s^{-1}, $k_{4.6} = 1.0 \times 10^{-11}$ cm^3 $molecule^{-1}$ s^{-1}, and $k_{4.7} < 3.0 \times 10^{-14}$ cm^3 $molecule^{-1}$ s^{-1} [*Atkinson*, 1994]. Despite the slow rate of reaction with oxygen, this reaction will dominate in the atmosphere due to the high concentration of oxygen. The reaction of the adduct with NO_2 will only be of importance in regions of very high NO_x concentration such as a combustion exhaust plume.

The reaction of the adduct with O_2 may proceed via numerous pathways. The first pathway is hydrogen abstraction to form the stable cresol (III) and HO_2. The second pathway is addition of oxygen to the ring to form a peroxy radical (V). This pathway has recently been shown to

be reversible, unlike many other organic radical reactions to form RO_2 [*Bohn*, 2001]. Recent studies have also suggested that the reaction of the adduct with oxygen could lead to the formation of toluene oxide (IV) which could isomerize to form methyloxepin [*Klotz et al.*, 2000].

The peroxy radical (V) formed from the adduct + O_2 reaction could undergo reaction with NO to form the corresponding alkoxy radical or organic nitrate, or it could undergo internal cyclization to form a bridged bicyclic radical (VI). Recent work suggests that this bridged radical intermediate decomposes to form glyoxal and other dicarbonyls [*Volkamer et al.*, 2001], however it may also add another O_2 molecule to form a bridged peroxy radical (VII). This peroxy radical may react with NO or go on to decompose or rearrange in some way.

It is clear that product studies alone are insufficient to elucidate the oxidation mechanism, the complexity of which is illustrated by the studies cited here. In particular, the study of the intermediate steps of this mechanism is complicated by the presence of many equilibrium reactions, creating difficulties that cannot be resolved via product studies. Additionally, the carbon balance for this system has not been closed at this time, as there are still unidentified product species [*Atkinson*, 1994]. Direct studies of the intermediate steps of this reaction system would complement the product studies and are essential to the complete understanding of the mechanism of aromatic oxidation.

4.2 Toluene + OH Kinetics

4.2.1 Introduction

The first step in the elucidation of the atmospheric oxidation mechanism of toluene was the flow tube-CIMS study of the reaction of toluene and OH and the verification of the recommended

rate constant. The forward and reverse rate coefficients for this reaction are well known and are shown below

$$Toluene + OH \longrightarrow Benzyl + H_2O \tag{4.8}$$

$$Toluene + OH \overset{M}{\leftrightarrows} Adduct \tag{4.9}$$

with $k_{4.8} = 7.15 \times 10^{-13}$ cm^3 molecule^{-1} s^{-1}, $k_{4.9} = 5.24 \times 10^{-12}$ cm^3 molecule^{-1} s^{-1}, $k_{-4.9}$ = 4.9 s^{-1}[*Atkinson*, 1994; *Knispel et al.*, 1990]. The fact that this reaction is an equilibrium reaction with a significant reverse reaction rate prevents the simple pseudo-first order kinetic treatment of the data for this experiment.

The reaction kinetics were numerically modeled to determine the expected OH concentration profiles for the time scales of a flow tube study. Reactions 4.8 and 4.9 were used to model the OH decays for a variety of toluene concentrations. The data from the numerical model could be fit according to the solution to the system of differential equations describing the toluene + OH reactions.

$$\frac{d[OH]}{dt} = -k_8[Toluene][OH] - k_9[Toluene][OH] + k_{-9}[Adduct] \tag{4.10}$$

$$\frac{d[Adduct]}{dt} = k_9[Toluene][OH] - k_{-9}[Adduct] \tag{4.11}$$

Under conditions where the [Toluene]>>[OH], the solution of Equations 4.10 and 4.11 for the

OH concentration at time t is

$$[OH]_t = \frac{k_{4.9}k_{-4.9}}{(k_{4.8}+k_{4.9})^2[Toluene]+k_{4.9}k_{-4.9}}[OH]_0(1-e^{(-(k_{4.8}+k_{4.9})[Toluene]-\frac{k_{4.9}k_{-4.9}}{k_{4.8}+k_{4.9}})t})+$$
$$[OH]_0(e^{(-(k_{4.8}+k_{4.9})[Toluene]-\frac{k_{4.9}k_{-4.9}}{k_{4.8}+k_{4.9}})t}) \quad (4.12)$$

under the assumtion that [Adduct]$_t = \frac{k_9}{k_8+k_9}$([OH]$_0$ -[OH]$_t$). This assumption is only valid for short times and breaks down as the system reaches equilibrium.

A plot of the numerical model results and the fits of Equation 4.12 to this modeled data is given in Figure 4-2. The results from the non-linear least-squares fits using Equation 4.12 give values for the rate constants within 3% of the values used in the model. Figure 4.3 shows the results of an exponential fit to the modeled OH decays using a simple pseudo-first order treatment of the data. The results from these fits assuming pseudo-first order conditions yields an overall rate coefficient, $k_{4.1}$, of 4.5 $\times$ 10^{-12} cm^3 molecule^{-1} s^{-1}. This rate coefficient is 25% below that used in the model, however under the assumption that the reaction of toluene with OH is irreversible, a pseudo-first order treatment of the data yields a reasonable first approximation for k_1.

4.2.2 Chemical ionization

The detection of many organic species can not be accomplished through the use of negative ionization reactions involving SF_6^- or F^- [*Harrison*, 1992]. A positive chemical ionization scheme is used to detect many organics and oxygenated organics. The detection of toluene can

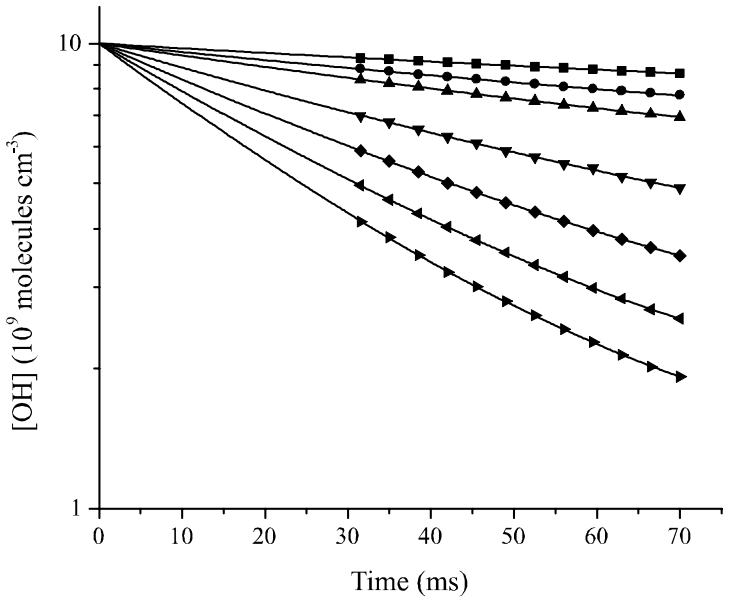

Figure 4-2: Model results for the toluene + OH reaction system. Toluene concentrations ranged from 4×10^{11} molecules cm^{-3} (■) to 5×10^{12} molecules cm^{-3} (▶). Best fit lines represent a non-linear least-squares fit of Equation 4.12 to the numerical model results..

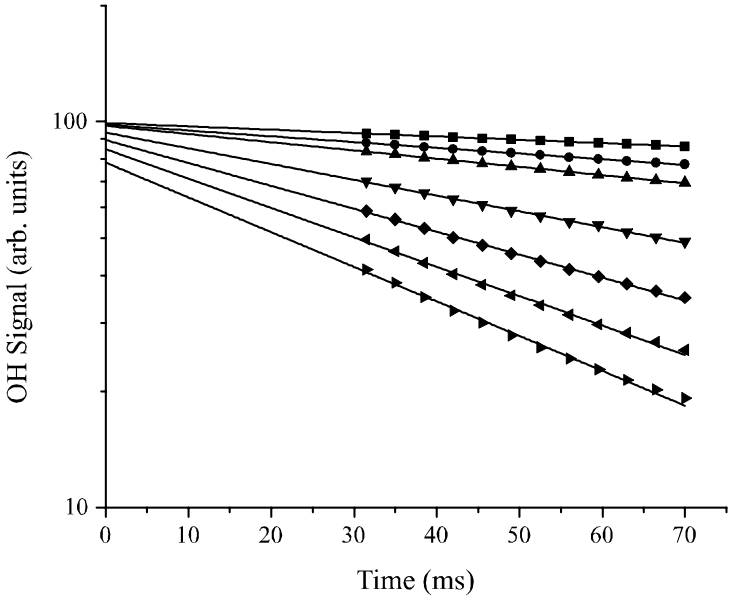

Figure 4-3: Model results for the toluene + OH reaction. Best fit lines represent a fit using a simple exponential assuming pseudo-first order kinetics ($[OH] = [OH]_0 * e^{-k[Toluene]t}$).

be achieved with the following ion-molecule reactions:

$$O_2^+ + C_7H_8 \longrightarrow C_7H_8^+ + O_2 \quad (major) \tag{4.13}$$

$$\longrightarrow C_7H_7^+ + Products \quad (minor) \tag{4.14}$$

$$\longrightarrow C_6H_5^+ + Products \quad (minor) \tag{4.15}$$

$$NO^+ + C_7H_8 \longrightarrow C_7H_8^+ + NO \tag{4.16}$$

$$\longrightarrow [C_7H_8 \cdot NO]^+ \tag{4.17}$$

NO^+ has been extensively used for the detection of aromatic compounds due to its low ionization energy (I.E. = 9.3 eV) [*Harrison*, 1992] which results in soft ionization collisions with aromatics, and its tendency to form positively charged adducts with organic molecules such as aromatic compounds.

A sample calibration curve for the detection of toluene is given in Figure 4-4. The high sensitivity to toluene with O_2^+ was encouraging for the detection of other aromatic radical species such as the toluene-OH adduct. The OH signal was monitored using SF_6^- according to Reaction 4.18.

$$SF_6^- + OH \longrightarrow OH^- + SF_6 \tag{4.18}$$

This reaction has been extensively used and is very sensitive for the detection of OH [*Lipson et al.*, 1999]. Using these chemical ionization schemes, both reactants could be monitored in the flow, although not simultaneously.

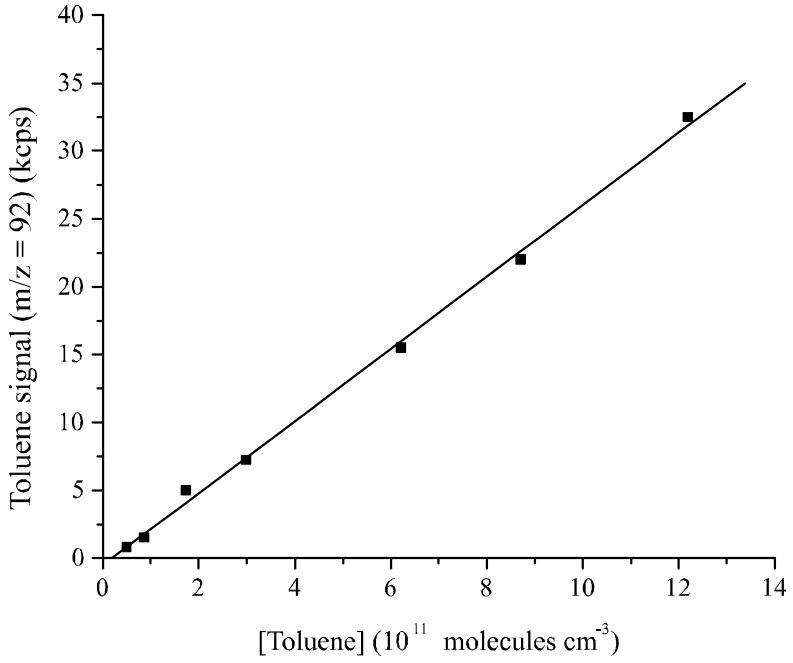

Figure 4-4: Calibration of toluene using O_2^+ as the ionization reagent. Reciprocal slope of the linear least-squares fit gives the sensitivity ($1/m = 3.7 \times 10^7$ molecules cm^{-3} cps^{-1}).

4.2.3 Experimental setup

The experimental setup was similar to that used for the methane oxidation reactions (Chapter 3). A diagram of the setup is shown in Figure 4-5. OH was produced in the sidearm via microwave discharge. A large flow of UHP He (3 STP L min^{-1}) was mixed with a 2% mixture of F_2 in He (0.1 STP cm^3 min^{-1}). The fluorine atoms produced in the microwave discharge were mixed with a flow of UHP He (2 STP cm^3 min^{-1}) saturated with water vapor from a fritted bubbler held at 0°C in an ice-water bath. OH radicals were produced via the reaction

$$F + H_2O \longrightarrow OH + HF \tag{4.19}$$

with $k_{4.19} = 1.4 \times 10^{-11}$ cm^3 molecule^{-1} s^{-1} [*DeMore et al.*, 1997]. The concentration of water vapor in the sidearm was $>1 \times 10^{14}$ molecules cm^{-3} so that >99% of the fluorine atoms were converted to OH in the sidearm.

Toluene vapor was introduced through the moveable injector by passing a UHP He flow (1-10 STP cm^3 min^{-1}) through a fritted bubbler containing toluene which was held in an *o*-xylene-liquid N_2 slush bath at -30°C. The vapor pressure of toluene at this temperature is 0.81 Torr [*Lide*, 1990] yielding toluene concentrations of 5-50 $\times 10^{11}$ molecules cm^{-3} in the flow tube under normal flow conditions. The flow tube was coated with Halocarbon wax (Halocarbon Products, Inc.) and the injector was fitted with the teflon turbulizer described previously. A high flow of UHP N_2 (50 STP L min^{-1}) served as the carrier gas and the pressure in the flow tube was maintained at 100 Torr under flow conditions. The flowtube was pumped by a Varian rotary vane pump (SD-700) and pressures were measured with a capacitance manometer (MKS Baratron). All flows were measured with calibrated flowmeters (Tylan 360). As described previously, a 1 mm pinhole separated the flow tube from the chemical ionization region. Ions were formed by addition of a trace amount (10 ppm) of either SF_6 or O_2 to a flow of UHP Ar (BOC 99.998%) (3 STP L min^{-1}). The flow was passed over a corona discharge needle operating at ±4 kV. This allowed the production of either O_2^+ or SF_6^- depending on the species of interest, toluene or OH. The chemical ionization flow was pumped by a Edwards rotary vane pump (E2M18) and pressures in the CI region ranged from 10-20 Torr depending on the flow conditions.

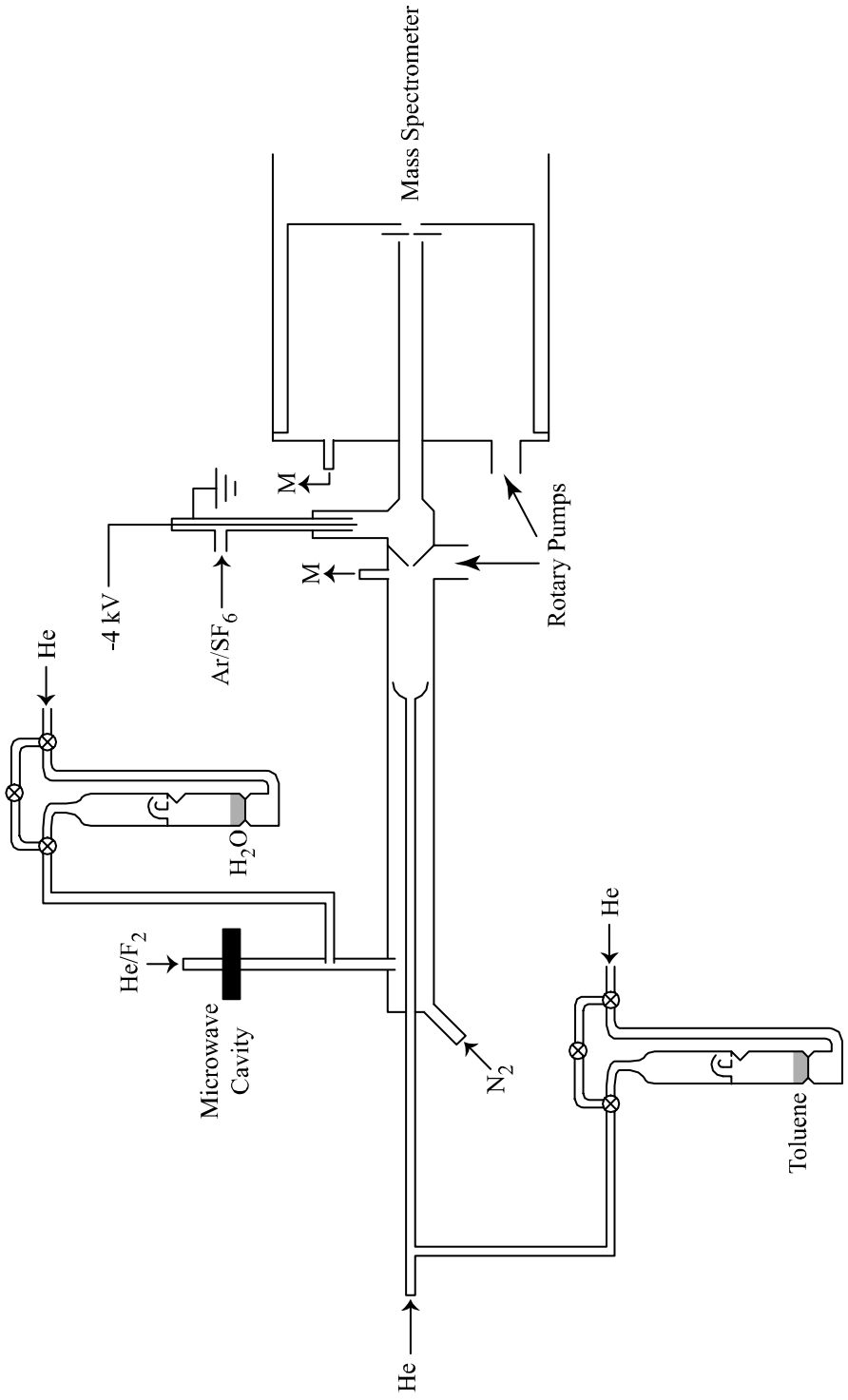

Figure 4-5: Experimental setup for the reaction of toluene with OH. The drawing is not to scale.

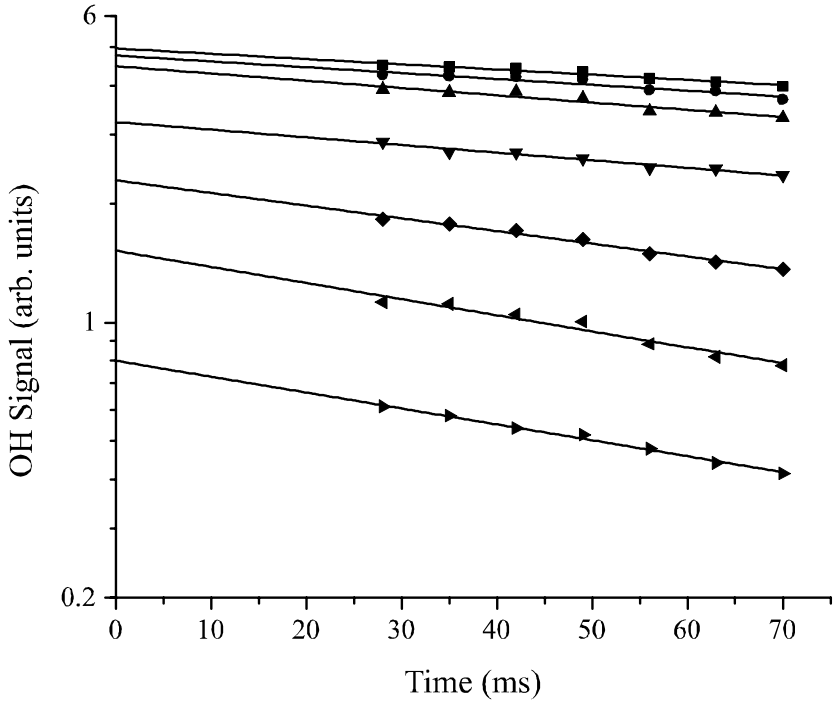

Figure 4-6: Typical OH decay profiles vs. reaction time for a number of toluene concentrations ranging from 1.8×10^{11} molecules cm^{-3} (●) to 4.1×10^{12} molecules cm^{-3} (►). Best fit lines represent a non-liear least-squares fit to a simple exponential ($y = ae^{-bx}$) assuming pseudo-first order conditions and an irreversible reaction.

4.2.4 Results and discussion

Hydroxyl radical (OH) decays were monitored as a function of time for various toluene concentrations. Equation 4.12 was applicable only when the concentration of toluene did not change significantly as a function of reaction time. This condition was verified by monitoring the toluene signal as a function of injector position with the OH microwave discharge operating. This condition held for all concentrations of toluene used in these experiments. Therefore the [OH] was estimated to be less than 5×10^{10} molecules cm^{-3}. Figure 4-6 gives a typical set of OH decay profiles for a number of toluene concentrations. The measured decays are very different than the modeled decays shown in Figure 4-2 and the non-linear fit to Equation 4.12

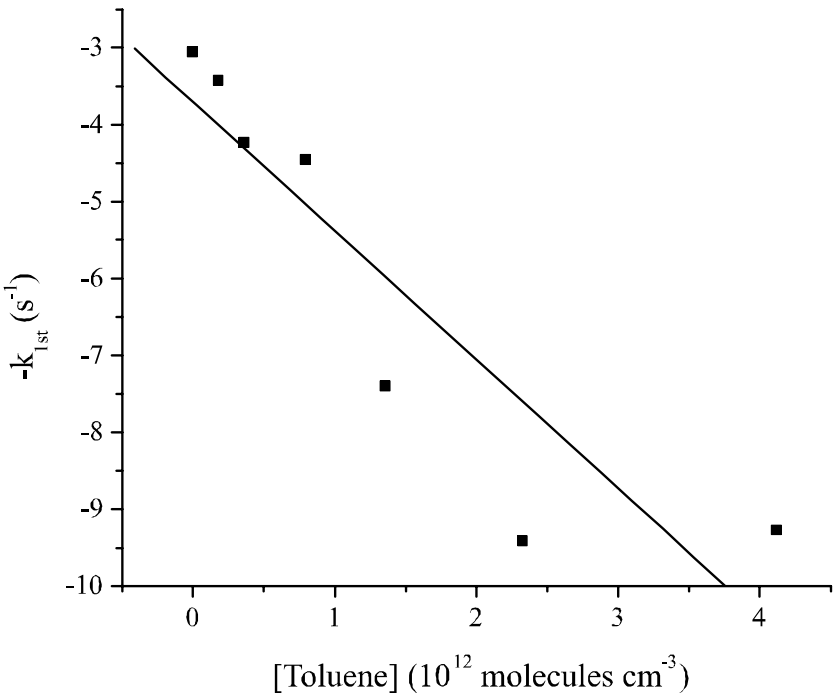

Figure 4-7: Plot of the pseudo-first order OH decay rates vs. toluene concentration. The linear least-squares fit gives the second order rate of 1.6×10^{-12} cm^3 molecule^{-1} s^{-1}.

did not converge when the [Toluene] and $[OH]_0$ were fixed. The $[OH]_0$ was also allowed to vary and the fit again did not converge. A plot of the pseudo-first order decay rates as a function of toluene concentration is given in Figure 4.7. The non-linear least-squares fits from Figure 4-6 vs. the toluene concentrations yielded a slope of 1.6×10^{-12} cm^3 molecule^{-1} s^{-1}. This rate coefficient is almost a factor of 4 lower than the current recommendation of Atkinson. Even a fit to the first three data points yields a rate coefficient which is a factor of 2 below the recommendation.

The OH reaction profiles in Figure 4-6 suggest that there is a secondary loss process for OH in the flow tube, and this loss rate may increase as a function of time. The OH decays in Figure 4-6 were performed sequentially from lowest to highest toluene concentrations. The

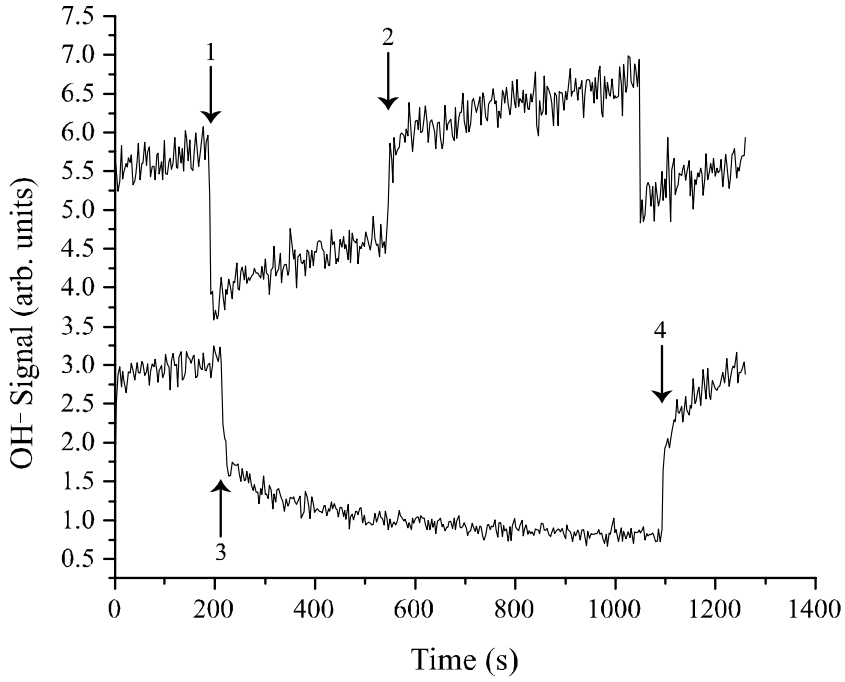

Figure 4-8: OH profiles as a function of time. The upper trace is the OH response to NO_2. The lower trace is the response to toluene.

order of the measurements was reversed (e.g. from highest to lowest toluene concentration) to determine if a strong time dependence of this unknown OH loss was observable, however the decays were similar when the order was reversed.

The OH profile as a function of time for a single toluene concentration was then recorded and compared to a similar OH decay profile when NO_2 was introduced instead of toluene via the injector. This plot is shown in Figure 4-8. The OH signal was rising over the course of these experiments due to conditioning of the walls of the sidearm to fluorine atoms and OH radicals. The upper trace in the plot is the OH response to the addition of NO_2 to the flow tube with a constant reaction time of 70 ms. At position 1 in the plot, $\sim 1.5 \times 10^{12}$ molecules cm^{-3} of NO_2 was introduced through the moveable injector. The signal immediately dropped

and stabilized within 50 s. The OH signal continued the upward trend seen before the NO_2 was added. Moreover, the OH signal dropped by approximately 30% which is consistant with the recommended rate constant of 3.4×10^{-12} cm^3 molecule^{-1} s^{-1} [*DeMore et al.*, 1997] for the reaction of OH with NO_2 at 100 Torr and under these conditions. At position 2, the NO_2 flow was stopped and the OH signal quickly recovered (<200 s). The signal recovery may have been slower than the decay due to residual NO_2 being purged from the injector.

The lower trace shows the effect of adding toluene through the moveable injector with a constant reaction time of 70 ms. Position 3 in the plot corresponds to the addition of $\sim 1.0 \times 10^{12}$ molecules cm^{-3} of toluene via the bubbler. The expected OH signal loss for these conditions was 35% corresponding in this experiment to a signal drop from 3.1 to 2.0. As seen in the plot, the initial decay in the OH signal is larger than expected, followed by a long slow decay (>1000 s) of the OH signal. If the OH signal was monitored long enough (>1 hr) in the presence of toluene, the signal approached the background noise level. The toluene flow was stopped at point 4 in the plot, and the OH recovery also has a much longer time constant than the NO_2 experiment.

The source of this phenomenon was difficult to ascertain. The toluene concentration in the flow tube could change over time due to bubbler effects such as non-saturated gas flows or entrained aerosols, or could be due to passivation processes in the teflon tubing which connected the bubbler to the pyrex injector. The bubbler was replaced with a 1% gas-phase mixture of toluene in UHP N_2 in a passivated 3 L pyrex bulb. The teflon tubing connecting the toluene flow meter to the injector was shortened to minimize the surface area in contact with high concentrations of toluene. Neither of these changes had a significant effect on the OH response. These toluene concentration effects would also likely not lead to complete loss of the OH signal

over long times.

A more likely explanation for the observed decays was a loss process for OH based on the accumulation of toluene or a product of the toluene-OH reaction on the surfaces of the flow tube. If OH underwent a heterogeneous reaction with toluene or a reaction product on the walls of the flow tube, the loss rate of OH would increase as this organic matter accumulated. A number of experiments were conducted to test this hypothesis. The toluene flow through the injector was turned on 1 hour before the OH discharge was activated. The toluene should have significantly accumulated on the walls of the flow tube and the observed OH profile would be markedly different from that in Figure 4-8. The profile did not change significantly, however, from that in Figure 4-8. Toluene adsorption on the wall did not seem to play a significant role, however the OH loss may have been due to products of the reaction.

The flow tube was coated with Halocarbon wax for the data presented in Figure 4-8, so the experiments were repeated with a thin sheet of teflon as a coating in the flow tube and with bare pyrex walls to determine if the wall characteristics would have a significant impact on the OH profile. Once again, the OH profile remained unchanged for various wall coatings. An organic smell was noticed on the teflon sheet insert when it was removed from the flow tube, so the entire setup was examined. A light brown organic coating was observed in the chemical ionization region, especially near the 1 mm pinhole where expansion of the flowtube effluent occurs and the low pressures are more conducive to wall reactions. The chemical ionization region was cleaned and coated with halocarbon wax. The experiment was repeated and no significant change in the OH profile was observed. It was therefore assumed that the organic deposition was not a reactive uptake on the walls of the flow tube and chemical ionization region, but a condensation process involving low-volatility products of the toluene-OH reaction. Production

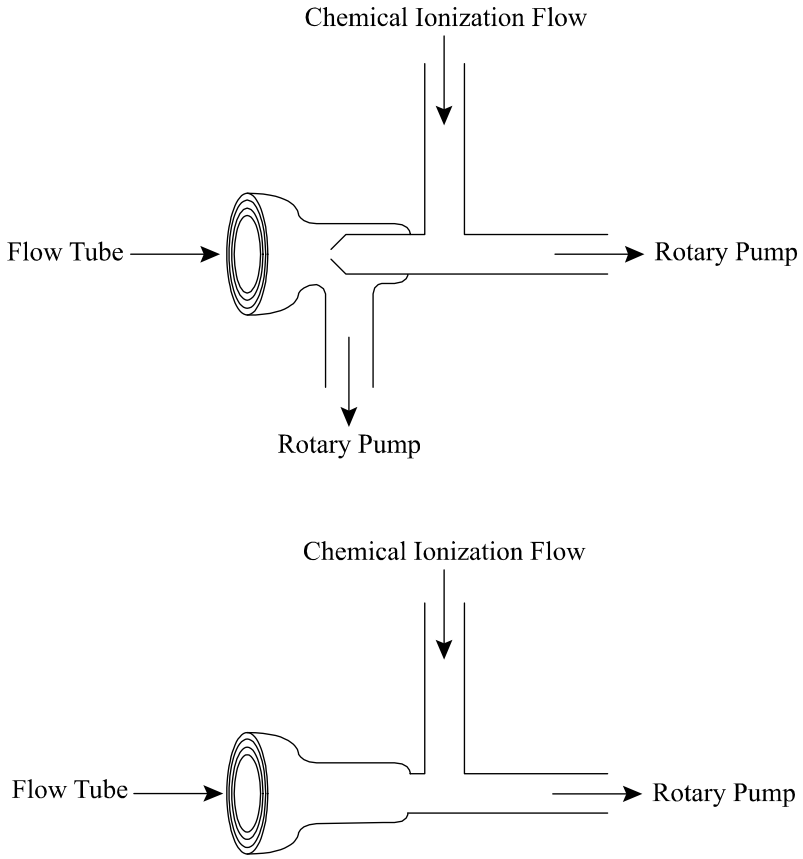

Figure 4-9: Design modification for the chemical ionization region.

of secondary organic aerosols has been observed in the oxidation of toluene [*Hurley et al.*, 2001], lending some support to this argument. For a condensation process, the chemical reactivity of the surface should have little effect on the accumulation of organic matter as was observed in the experiments.

A design modification in the chemical ionization region could potentially solve this problem. A schematic of the design modification made is shown in Figure 4-9. The upper drawing in Figure 4-9 shows the design used in the previous experiments. The gas from the flowtube is pumped by the Varian SD-700 rotary vane pump, but a small portion expands through the

pinhole into the chemical ionization region where it meets the chemical ionization flow. This combined flow is pumped by a second rotary vane pump. This design creates a pressure drop between the two regions. The lower pressure in the chemical ionization region was useful for more efficient ion production and dilution of the high concentrations of reactants in the methane oxidation studies. The pinhole was removed so that the entire flow from the flow tube mixed with the chemical ionization flow and was pumped by the Varian SD-700 rotary vane pump. The pressure in the chemical ionization region and flow tube was now 100 Torr. This modification limited the number of gas collisions with the walls in the chemical ionization region due to the higher pressures and this hopefully reduced or eliminated the wall loss of OH.

Figure 4-10 shows OH profiles for the two chemical ionization region designs. The OH profile as a function of time is shown for each case after the toluene is introduced into the flow tube. The OH profile for the new design decayed with a different time constant and the OH signal did not decay to zero at long times, however the asymptotic value was still well below the value expected based on the known rate constant, toluene concentration, and reaction time. Eliminating the expansion region appears to have reduced the wall loss effect on OH concentration, however even at high pressures wall reactions of OH seem to play a significant role in the measured profiles..

4.2.5 Conclusions

This unknown time dependent loss process for OH prevented precise measurements of the toluene-OH rate constant, however this reaction rate is well known and was being studied as a first step in the oxidation of toluene. The problem of product condensation has not been solved and remains a large unknown in this flow tube study of the oxidation of toluene.

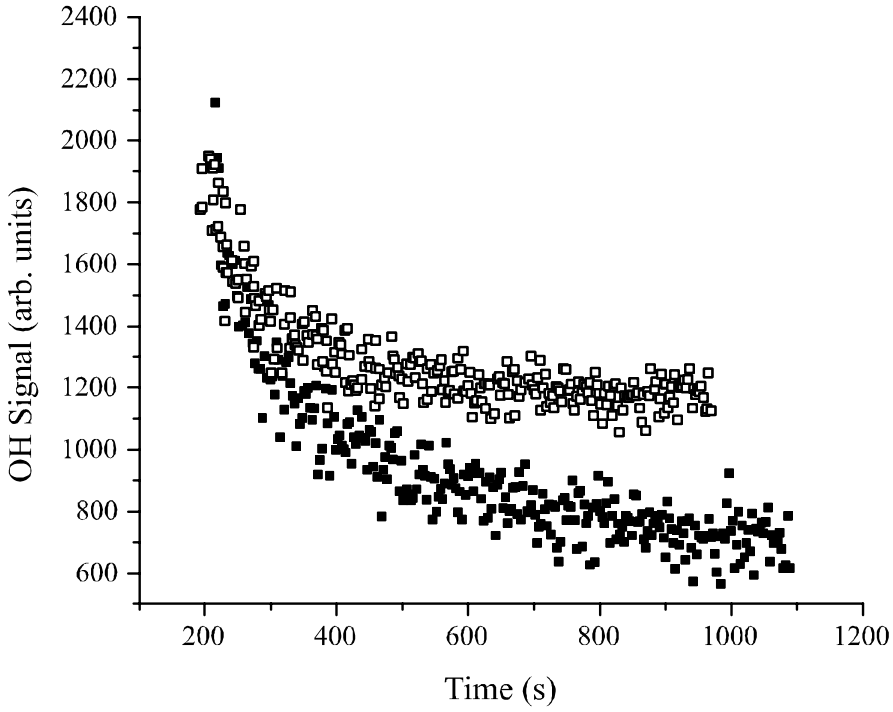

Figure 4-10: OH profiles as a function of time for the two CI region designs. The beginning of each set of data corresponds to the introduction of toluene. (■) - expansion design, (□) - new design. Signals have been normalized for comparison.

4.3 Detection and Kinetics of the Toluene-OH Adduct

4.3.1 Introduction

As discussed in the previous sections, the reversible reaction of toluene with OH produces four isomers of the methylhydroxycyclohexadienyl radical (MHCHD), or the toluene-OH adduct. The reaction to form the adduct is shown in Figure 4-11. Based on simple organic chemistry principles, the ortho-MHCHD and para-MHCHD radicals should be favored due to inductive effects by the methyl group. This has been shown to be the case experimentally by analyzing the product yield of the cresols formed from the reactions of the adducts [*Kenley et al.*, 1978]. Recent theoretical studies have shown that the ipso-MHCHD is energetically possible, even

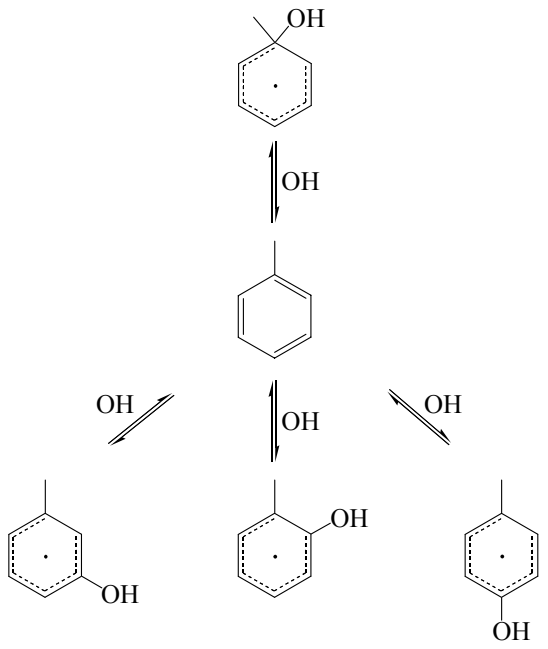

Figure 4-11: The reaction of toluene to form the four toluene-OH adducts (ortho-, meta-, para-, and ipso-).

favored [*Uc et al.*, 2000; *Zhang*, 2001]. This discrepancy could be explained by a 1,2 shift of the hydoxyl group on the ipso-adduct to form ortho-cresol. The experimental and theoretical yields for the various isomers are summarized in Table 4.1.

Isomer	**Experiment**[a]	**Theory**[b]	**Theory**[c]
ipso	—	56.8%	3%
ortho	80.6%	40.3%	52%
para	14.3%	1.2%	34%
meta	5.1%	1.6%	11%

Table 4.1: Distribution of adduct isomers from various studies. [a][*Kenley et al.*, 1978]. [b][*Uc et al.*, 2000]. [c][*Zhang*, 2001].

As seen in Table 4.1, there is very little agreement between experiments and theory at this time as to the relative importance of the various reaction channels.

Kinetic studies of the adducts have been performed by a variety of methods [*Knispel et*

al., 1990; *Bohn et al.*, 2001; *Volkamer et al.*, 2001]. Bohn used the technique of ultraviolet absorption to directly detect the adduct. The OH radicals were detected on the $Q_1(2)$ rotational line of the OH-($A^2\Sigma^+ \longleftarrow X^2\Pi$)-transition at 307.995 nm in air. The adduct was detected -0.045 nm off the OH line [*Bohn et al.*, 2001]. The spectrum of the adduct is a broad continuum on which the OH lines appear [*Markert & Pagsberg*, 1993]. The adduct signal was then monitored under a variety of conditions. The strength of this technique is that the adduct is directly detected, however the detection is not unique as other radical intermediates or final products may also have broadband absorptions at this wavelength. The peroxy radical formed from the reaction of the adduct with O_2 is thought to have a weak absorption at this wavelength which complicates the data analysis [*Bohn et al.*, 2001].

The study of Knispel also uses the technique of ultraviolet absorption of the $Q_1(2)$ line of OH, however the kinetics of the adduct are inferred from the multi-exponential decays of OH in the presence of toluene and NO, NO_2, and O_2 [*Knispel et al.*, 1990]. The OH signals must still be corrected in these experiments for the underlying absorption of the adduct and other products. Extracting the rate constants from OH decays is also difficult, as shown by Figure 4-12. In the case where O_2 is used as the scavenger, the OH signal would be insensitive to the fast equilibrium with oxygen to form the peroxy radical proposed by Bohn, but the irreversible losses of the peroxy radical and the adduct would be seen in the OH decay profiles. This technique is useful in determining overall loss rates of the adduct in the presence of various scavengers, but does not directly detect the adduct or other radical intermediates in the oxidation of toluene. This limits the effectiveness of this technique in elucidating the details of the mechanism.

Table 4.2 is a summary of the current rate coefficient measurements for the toluene-OH adduct.

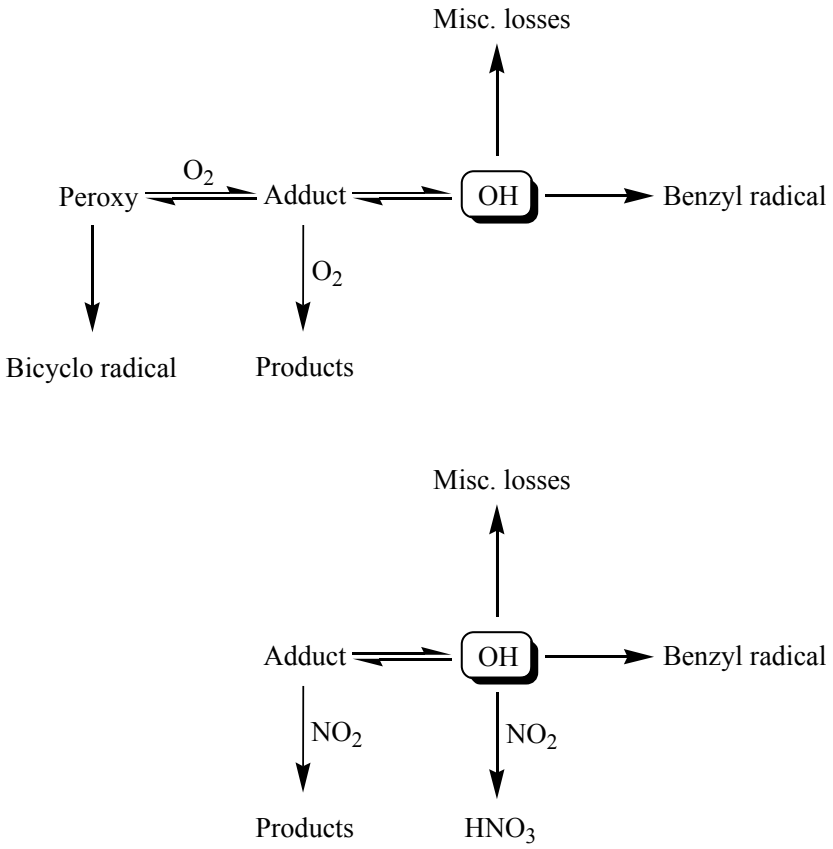

Figure 4-12: Processes governing the OH decays in the experiments of Knispel et al. The upper diagram is for production of the adduct in the presence of oxygen and the lower case is in the presence of NO_2.

Detection of the adduct and other oxidation products via mass spectrometry has the potential to uniquely identify the various products for each step in the oxidation process and directly measure the kinetics of these products. Isomers can not be distinguished by basic mass spectrometry techniques, however as mentioned earlier, some information on branching ratios is already available.

	NO [a]	**NO_2**	**O_2** [b]	**HO_2**	**Adduct**
Bohn, 2001	—	—	6.0×10^{-16}	1.8×10^{-10}	4.7×10^{-11}
Knispel et al., 1990	$<3 \times 10^{-14}$	3.6×10^{-11}	5.4×10^{-16}	—	—

Table 4.2: Rate coefficients for the reaction of the adduct with various molecules of interest. Rate coefficients are given for 300 K and in units of cm^3 $molecule^{-1}$ s^{-1}. [a]Rate coefficient is given for 333 K. [b]Rate is for the irreversible loss of the adduct with O_2. Bohn gives an equilibrium constant for the reversible peroxy-adduct formation of 3.25×10^{-19} cm^3.

4.3.2 Chemical ionization

The ionization energy of aromatic hydrocarbons is below that of many other hydrocarbons [*Harrison*, 1992]. Toluene has an ionization energy of 8.5 eV and is easily ionized by reagents such as O_2^+ and NO^+ which have ionization energies of 12.1 eV and 9.3 eV respectively. The cresols have ionization energies in the 8.5 eV range, and the deuterium atom-toluene adduct ionization potential has been measured to be 7.6 eV [*Sloane & Brudzynski*, 1980], so the ionization energy of the toluene-OH adduct likely does not differ markedly from these values. The ionization reactions used to detect the adduct were therefore

$$C_7H_8OH + O_2^+ \longrightarrow C_7H_8OH^+ + O_2 \tag{4.20}$$

$$C_7H_8OH + NO^+ \longrightarrow C_7H_8OH^+ + NO \tag{4.21}$$

with $k_{4.20} = 9.6 \times 10^{-10}$ cm^3 $molecule^{-1}$ s^{-1} [*Molina et al.*, 1999].

The detection of other intermediate products was attempted using a variety of chemical ionization reagents. The electron affinities of various organic peroxy radicals have been measured and are universally higher than that of O_2. The electron affinities of HO_2, CH_3O_2, $CH_3CH_2O_2$, and $(CH_3)_3CO_2$ are 1.09 eV, 1.16 eV, 1.19 eV, and 1.20 eV respectively [*Clifford et al.*, 1998; *Blanksby et al.*, 2001]. These electron affinities are all higher than those of both O_2 (0.45 eV)

and SF_6 (1.05 eV) [*Lide*, 1990]. This suggests that negative ion charge transfer reactions could be used to detect the aromatic peroxy radicals. O_2^- has been used to detect organic peroxy radicals previously [*Eberhard et al.*, 1996], however, despite the apparent electron affinity difference, SF_6^- has not been successfully used to detect organic peroxy radicals in the past. This may suggest that literature value for the electron affinity of SF_6 is low. F^- has also been used to detect organic peroxy radicals (Section 3.3.3), however F^- usually reacts via proton abstraction or formation of a fluorinated organic compound such as CH_3F. For both HO_2 and CH_3O_2, the ion detected via ionization with F^- was O_2^-, therefore F^- may not uniquely ionize the different peroxy radicals formed in the oxidation of toluene. Positive ions such as O_2^+ have also been used to detect peroxy radicals [*Villalta et al.*, 1995], so there a number of possible chemical ionization schemes available to detect the radical intermediates.

4.3.3 Experimental setup

The initial setup used for the detection of the toluene-OH adduct is described in detail in Section 3.2.3 and in Figure 4-5. The corona discharge operated at a voltage of +4 kV and the trace species used in the ionization flow were O_2 or NO to produce the positive ion of interest, O_2^+ and NO^+. The setup used to detect other reaction intermediates and measure the kinetics of the adduct is shown in Figure 4-13. The adduct was formed in the sidearm via a two step reaction. The fluorine atoms produced in the microwave discharge reacted with water vapor via Reaction 4.19. The OH radicals formed in this reaction then reacted with toluene via Reaction 4.9 to form the adduct. The carrier gas in the flow tube was UHP N_2 (40 STP L min^{-1}). The total flow through the injector was held constant (10 STP L min^{-1}) and was a variable mixture of UHP He and UHP O_2. In this way the O_2 concentration in the flow tube

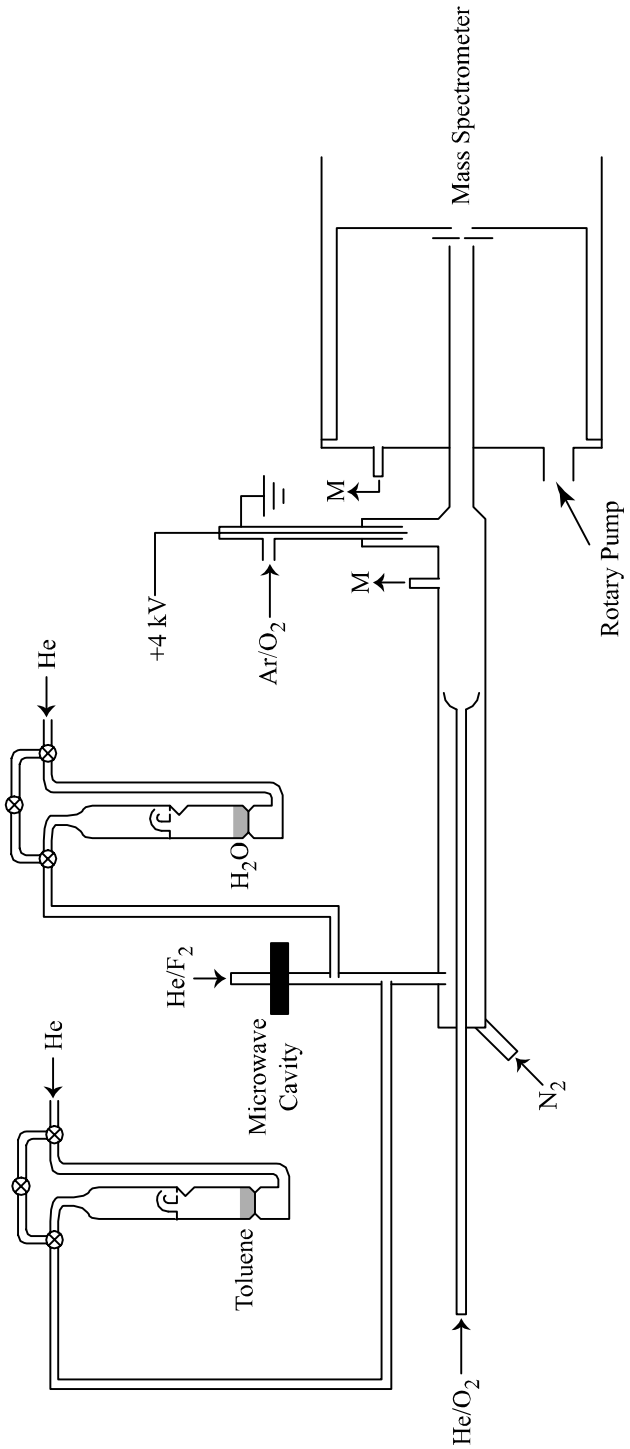

Figure 4-13: Experimental setup for the detection of intermediates in the oxidation of toluene. M = capacitance manometer.

could be varied from 0-1 $\times$ 10^{18} molecules cm^{-3} without perturbing the flow dynamics in the flow tube. For the reaction of the adduct with NO_2, a mixture of UHP He (2 STP L min^{-1}) and 1% NO_2/N_2 (1 STP cm^3 min^{-1}) was introduced through the injector and the UHP N_2 carrier flow was increased (50 STP L min^{-1}). The negative ions SF_6^- and F^- were generated by reversing the polarity of the corona discharge and adding SF_6 or NF_3 to the Ar flow over the needle.

4.3.4 Results and discussion

The toluene-OH adduct was detected using both O_2^+ and NO^+ as chemical ionization reagents. For both chemical ionization schemes, the dominant adduct peak was *m/e* 109 which corresponds to $C_7H_8OH^+$. Figures 4-14 and 4-15 give sample spectra for the adduct under various conditions. Figure 4-14 is a spectrum of the adduct with the F + H_2O radical source and toluene present in the flow tube. The signal was dependent on both the presence of toluene and OH in the flow tube. O_2^+ was used as the ionization reagent for this spectrum. Figure 4-15 shows a spectrum of the adduct using NO^+ as the ionization reagent. The OH source was also changed for this experiment. The reaction

$$H + O_3 \longrightarrow OH + O_2 \tag{4.22}$$

with $k_{4.22} = 2.9 \times 10^{-11}$ cm^3 $molecule^{-1}$ s^{-1} [*DeMore et al.*, 1997] was used to produce OH. Hydrogen replaced the F_2 normally passed through the microwave discharge and an excess of O_3 was introduced through the water vapor port in the sidearm. The dominant peak was once again *m/e* 109. There were a number of satellite peaks in both spectra, however the number

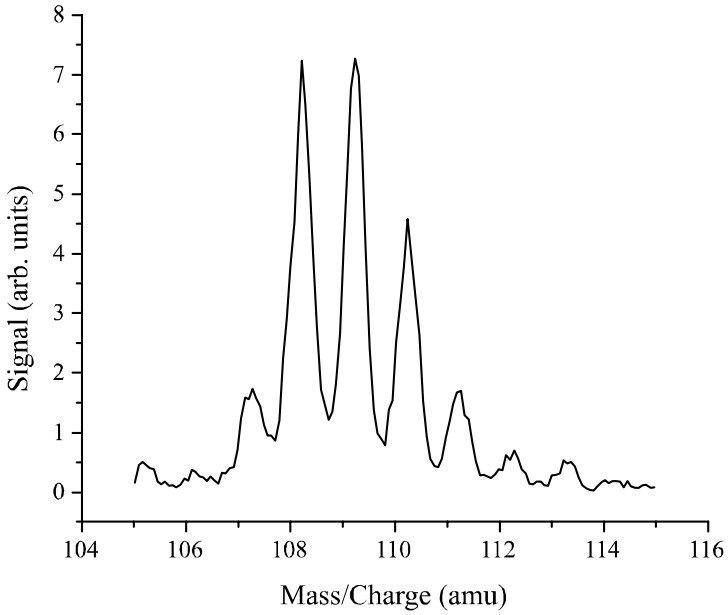

Figure 4-14: Toluene-OH adduct spectrum using O_2^+ as the ionization reagent. OH was produced by the reaction of fluorine atoms with H_2O.

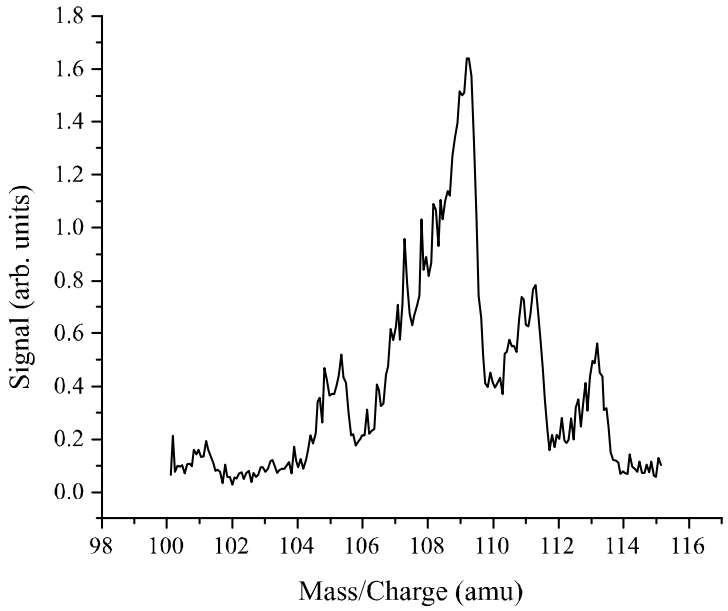

Figure 4-15: Toluene-OH adduct spectrum using NO^+ as the ionization reagent. OH was produced by the reaction of hydrogen atoms with O_3.

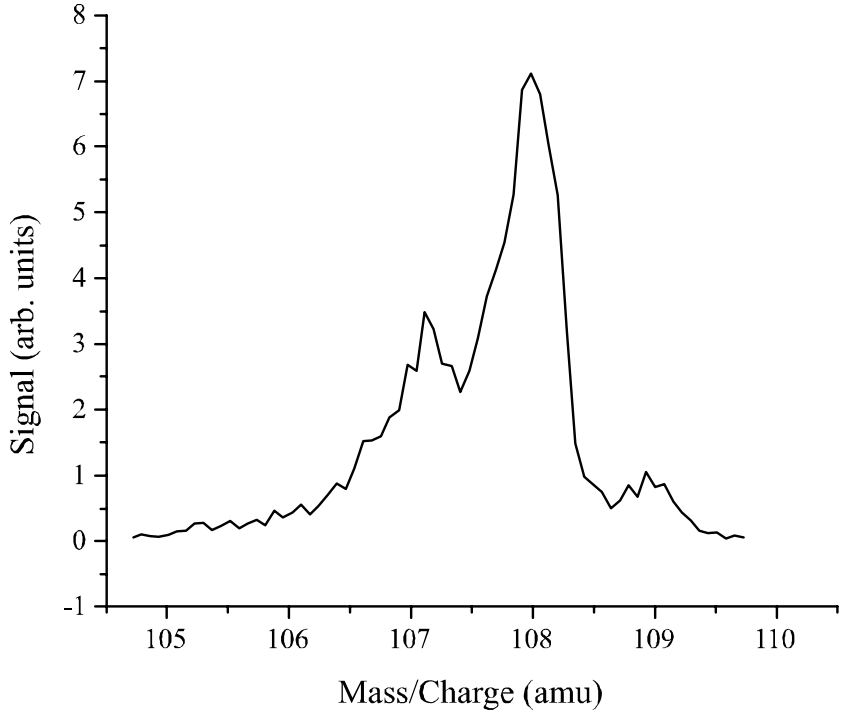

Figure 4-16: Spectrum of *o*-cresol using O_2^+ as the ionization reagent.

and intensity of the peaks changed between the two experiments. The satellite peaks at *m/e* 107, 108, 110, 111, 112, and 113 in Figure 4-14 could be attributed to a number of species. The peak at *m/e* 108 could be due to a product such as ortho-, para-, or meta-cresol. The peaks at *m/e* 110 and 111 could be due to fluorotoluene and the F-toluene adduct, respectively. Both of these products are known to form in the reaction of F atoms with toluene. An excess of H_2O vapor was used to completely scavenge the F atoms, however side reactions in the flow tube could produce small amounts of F atoms. The high concentration of H_2O vapor could also lead to ion-water clusters such as $C_7H_8^+ \cdot H_2O$ at *m/e* 110. The spectrum of *o*-cresol using O_2^+ as the ionization reagent is shown in Figure 4-16. The dominant peak is at *m/e* 108, so the cresols are likely not the source of the peak at *m/e* 109. Elucidation of the identities of

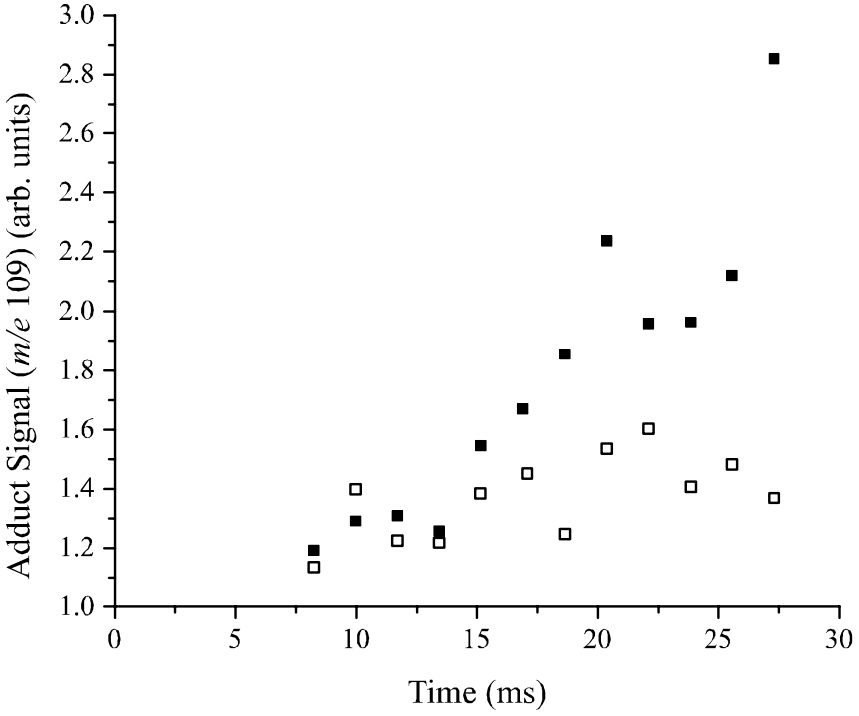

Figure 4-17: Plot of the adduct signal as a function of time for the toluene-OH reaction. $[OH]_0 = 5 \times 10^{10}$ molecules cm^{-3} and $[C_7H_8] = 4 \times 10^{12}$ molecules cm^{-3} for both sets of data.

the peaks around m/e 109 was very difficult, but the entire cluster of peaks was dependent on both toluene in the flow tube and the radical source operating.

The next step was to monitor the cluster of peaks around m/e 109 as a function of reaction time between toluene and OH. The toluene was introduced through the moveable injector as described earlier. Figure 4-17 shows a plot of the adduct signal at m/e 109 as a function of time for $[OH]_0 = 5 \times 10^{10}$ molecules cm^{-3} and $[C_7H_8] = 4 \times 10^{12}$ molecules cm^{-3}. This adduct signal behavior was not reproducible from run to run, even within the same day. The open squares in Figure 4-17 are data collected two hours after the filled squares, under the same conditions. The adduct signal remained flat as a function of time within the noise for the second run. The apparent rate of adduct formation appears to decrease over the course of

the day, however this result was also not reproducible from day to day.

The reaction of the adduct with O_2 and NO_2 was also examined. The adduct was produced in the sidearm as described in the previous section (Section 4.3.3). The adduct signal was monitored as a function of O_2 concentration in the flow tube for a constant reaction time (30 ms), however no decay in the adduct signal was measured for O_2 concentrations up to 7×10^{17} molecules cm^{-3}, putting an upper limit of $\sim 2 \times 10^{-18}$ cm^3 $molecule^{-1}$ s^{-1} on the rate coefficient of the adduct with O_2. The adduct signal was then monitored as a function of NO_2 concentration in the flow tube. The addition of NO_2 to the flow tube through the moveable injector increased the adduct signal by as much as a factor of 2 for NO_2 concentrations as high as 1×10^{13} molecules cm^{-3}. There was, however, no response of this adduct signal to changes in reaction time between the adduct and NO_2. Sample data for NO_2 is plotted in Figure 4-18.

There are a number of possible explanations for the behavior of the adduct in the presence of O_2 and NO_2. In the case of O_2, the reaction of the adduct may be slow enough so that we can not measure decays on the time scale available in the flow tube, even at high oxygen concentrations. This is contradictory to evidence in the literature of a rate constant near 5×10^{-16} cm^3 $molecule^{-1}$ s^{-1}. This rate has been measured directly [*Bohn*, 2001; *Knispel et al.*, 1990] and the agreement in the literature values is quite good. Another possible explanation is that the peroxy radical formed in the reaction of the adduct with O_2 is ionized in a reaction with O_2^+.

$$Peroxyadduct + O_2^+ \longrightarrow Adduct^+ + 2O_2 \tag{4.23}$$

This reaction is similar to the reaction of CH_3O_2 with O_2^+ described earlier. If the major product of the reaction of the adduct with O_2 was the peroxy adduct, then this ion-molecule

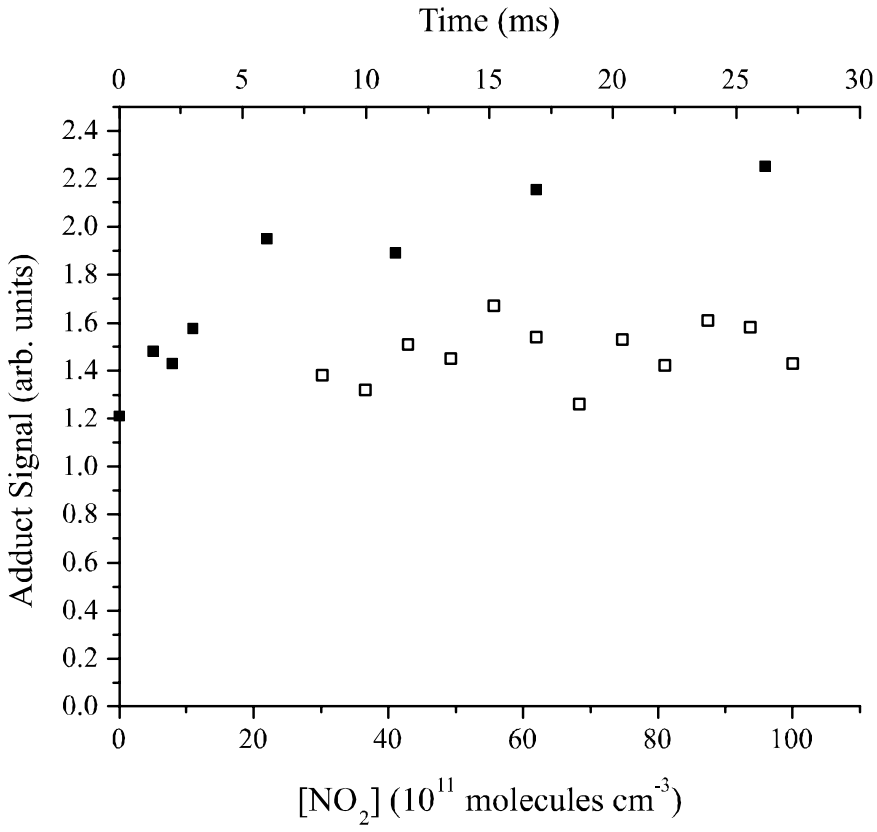

Figure 4-18: Adduct signal as a function of both reaction time with NO_2 and NO_2 concentration. (■) represent adduct signal for various NO_2 concentrations and a fixed reaction time (28 ms). (□) represent adduct signal as a function of reaction time for $[NO_2] = 5 \times 10^{11}$ molecules cm^{-3}.

reaction would interfere with the measurement of adduct decays. A third possible explanation is that the peak at m/e 109 is not the adduct, but a stable product produced by homogeneous or heterogeneous reactions of toluene and OH in our flow tube. This product is unlikely to be a cresol as has been shown, but may be another stable product. The evidence of organic material on the walls of the flow tube found in earlier experiments may also support the formation of unknown stable organic species.

The increase of the adduct signal in the presence of NO_2 is most likely due to ion-molecule

interference. The NO_2 in the flow tube is ionized to form NO_2^+ via a reaction with O_2^+. The fact that the adduct signal levels off at high NO_2 concentrations supports this interpretation since at these high concentrations, most of the O_2^+ has been converted to NO_2^+. The hypothesis that the peak at *m/e* 109 is an unknown stable product is also supported by the lack of a measurable decay in the adduct signal as the reaction time between the adduct and NO_2 is varied. There was no apparent decay in the adduct signal even at high NO_2 concentrations. This result is also contradictory to the literature value for the rate of reaction of the adduct with NO_2 [*Knispel et al.*, 1990].

Recently, the reaction of the adduct with itself has been proposed [*Bohn*, 2001]

$$Adduct + Adduct \longrightarrow Products \tag{4.24}$$

($k_{4.24} = 4.7 \times 10^{-11}$ cm^3 molecule^{-1} s^{-1}). This reaction could also explain the peaks observed as products of the adduct self-reaction. If this rate constant is valid, this reaction becomes important for moderate reactant initial concentrations as shown in Figure 4-19. For the initial concentrations shown, the concentration of the products of the self-reaction of the adduct has reached 2×10^9 molecules cm^{-3} at 50 ms of reaction time. This reaction becomes more significant for higher reactant concentrations and longer reaction times.

It is difficult to determine based on these experiments the identity of the peak at *m/e* 109. The peak is dependent on the presence of toluene and OH in the flow tube, and corresponds to the M^+ peak of the toluene-OH adduct, however the behavior of this peak in the presence of O_2 and NO_2 suggests that it may correspond to an unknown product of the reaction of toluene with OH. A collaborator at Texas A&M, Renyi Zhang, had success in detecting the adduct

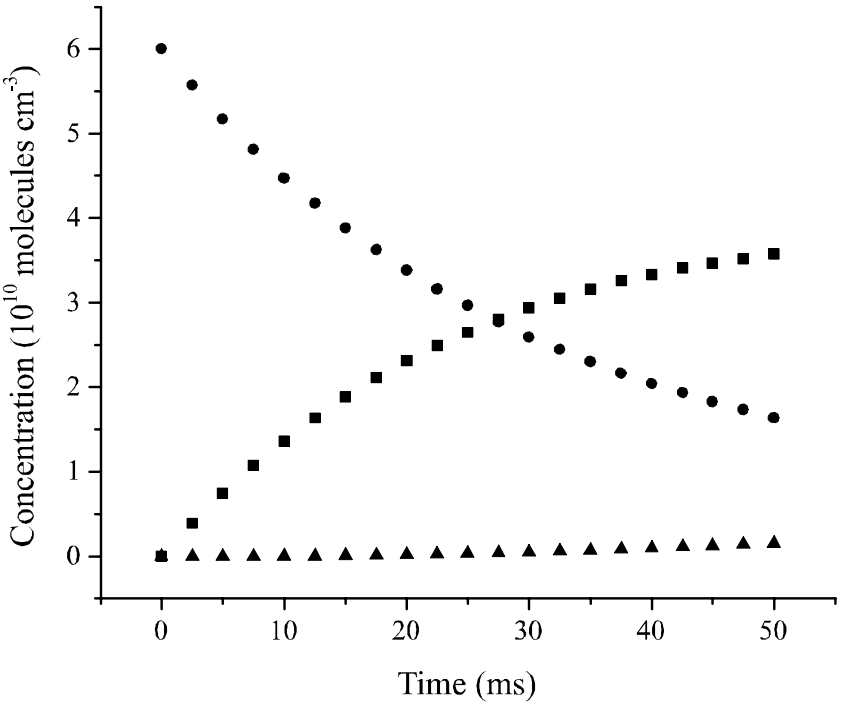

Figure 4-19: Model results for the reaction of toluene with OH including the self-reaction of the adduct. $[OH]_0 = 6 \times 10^{10}$ molecules cm^{-3}, $[C_7H_8]_0 = 5 \times 10^{12}$ molecules cm^{-3}. (■) - adduct, (●) - OH, and (▲) - self-reaction products.

at *m/e* 109 with O_2^+ and was able to measure a formation rate which corresponded fairly well with the literature value for the formation of the adduct [*Molina et al.*, 1999]. He carried out the experiments under different pressure and concentration conditions, so perhaps he did not encounter the same difficulties.

Experiments were also carried out to detect products of the reaction of the adduct with O_2. The molecules of interest in the proposed oxidation mechanism of toluene are shown in Figure 4-20. SF_6^-, F^-, and O_2^- were used as chemical ionization reagents to detect the various radical intermediates with O_2 concentrations in the flow tube as high as 1×10^{18} molecules cm^{-3}. No peaks were observed corresponding to any of the products of interest for the conditions used

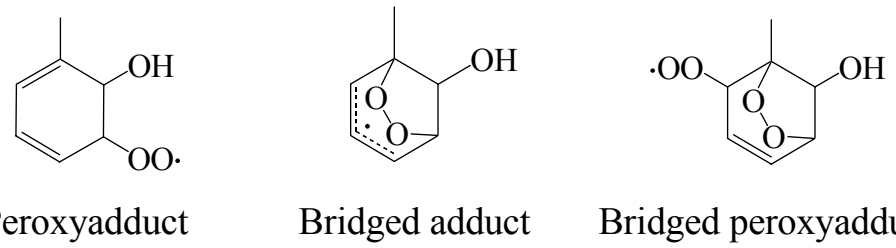

Figure 4-20: Proposed products for the reaction of the toluene-OH adduct with O_2. Not all the possible products are shown.

in these experiments. Our collaborator, Renyi Zhang, was able to detect a peak at m/e 141 using SF_6^- and this peak was assigned to the peroxy adduct [*Molina et al.*, 1999]. This peak assignment has been called into question recently by Bohn [*Bohn*, 2001]. His experiments have shown that the reaction to form the peroxyadduct is reversible

$$Adduct + O_2 \overset{M}{\leftrightarrows} Peroxyadduct \tag{4.25}$$

with $k_{4.25} = 3 \times 10^{-15}$ cm^3 molecule^{-1} s^{-1} and an equilibrium constant of $K_{eq} = 3.25 \times 10^{-19}$ cm^3 at 1 atm and 298 K. The peroxy adduct would be too short lived to be detected on the time scales of the flow tube experiments. He suggests the possibility that the peak corresponds instead to the bridged bicyclo-adduct or another product of the adduct-O_2 reaction.

4.4 Conclusions

While the flow tube-CIMS technique holds promise for the detection of organic radical intermediates, the toluene reactions proved to be a difficult starting point in establishing this technique for the elucidation of the oxidation mechanisms of VOCs. The technique has been shown to be

viable for the investigation of small organic molecules such as methane and ethane, but many problems need to be addressed in the case of a larger, more complex molecule such as toluene. The triple quadrupole mass spectrometer recently acquired by this laboratory also holds some promise for identification of specific isomers in organic oxidation mechanisms.

References for Chapter 4

Atkinson, R., Gas-phase tropospheric chemistry of organic compounds, *Journal of Physical and Chemical Reference Data Monograph No. 2*, 1994.

Atkinson, R. and S.M. Aschmann, Products of the gas-phase reactions of aromatic hydrocarbons: effect of NO_2 concentration, *Int. J. Chem. Kinet.*, **26**, 929-944, 1994.

Atkinson, R., S.M. Aschmann, J. Arey, and W.P.L. Carter, Formation of ring-retaining products from the OH radical-initiated reactions of benzene and toluene, *Int. J. Chem. Kinet.*, **21**, 801-827, 1989.

Baulch, D.L., C.J. Cobos, R.A. Cox, C. Esser, P. Frank, Th. Just, J.A. Kerr, M.J. Pilling, J. Troe, R.W. Walker, and J. Warnatz, Evaluated kinetic data for combustion modelling, *J. Phys. Chem. Ref. Data*, **21**, 411-429, 1992.

Blanksby, S.J., T.M. Ramond, G.E. Davico, M.R. Nimlos, S. Kato, V.M. Bierbaum, W.C. Lineberger, G.B. Ellison, and M. Okumura, Negative-ion photoelectron spectroscopy, gas-phase acidity, and thermochemistry of the peroxyl radicals CH_3OO and CH_3CH_2OO, *J. Am. Chem. Soc.*, **123**, 9585-9596, 2001.

Bohn, B., Formation of peroxy radicals from OH-toluene adducts and O_2, *J. Phys. Chem. A.,* **105**, 6092-6101, 2001.

Clifford, E.P., P.G. Wenthold, R. Gareyev, W.C. Lineberger, C.H. DePuy, V.M. Bierbaum, and G.B. Ellison, Photoelectron spectroscopy, gas phase acidity, and thermochemistry of tert-butyl hydroperoxide: Mechanisms for the rearrangement of peroxyl radicals, *J. Chem. Phys.*, **109**, 10293-10310, 1998.

DeMore, W.B., S.P. Sander, C.J. Howard, A.R. Ravishankara, D.M. Golden, C.E. Kolb, R.F. Hampson, M.J. Kurylo, and M.J. Molina, *Chemical Kinetics and Photochemical Data for Use in Stratospheric Modeling*, JPL Publication 97-4, Jet Propulsion Laboratory, Pasadena, CA, 1997.

Eberhard, J, P.W. Villalta, and C.J. Howard, Reaction of Isopropyl peroxy radicals with NO over the temperature range 201-401 K, *J. Phys. Chem.,* **100**, 993-997, 1996.

Harrison, A.G., *Chemical Ionization Mass Spectrometry*, CRC Press, Boca Raton, 1992, pp. 86-87, 120-124.

Hurley, M.D., O. Sokolov, T.J. Wallington, H. Takekawa, M. Karasawa, B. Klotz, I. Barnes, and K.H. Becker, Organic aerosol formation during the atmospheric degradation of toluene, *Environ. Sci. Technol.*, **35**, 1358-1366, 2001.

Jing, L.H., S.M. Steinberg, and B.J. Johnson, Aldehyde and monocyclic aromatic hydrocarbon mixing ratios at an urban site in Las Vegas, Nevada, *Journal of the Air & Waste*

Management Association, **51**, 1359-1366, 2001.

Karl T., R. Fall, P.J. Crutzen, A. Jordan, and W. Lindinger, High concentrations of reactive biogenic VOCs at a high altitude site in late autumn, *Geophys. Res. Lett.*, **28**, 507-510, 2001.

Kenley, R.A., J.E. Davenport, and D.G. Hendry, Hydroxyl radical reactions in the gas phase. Products and pathways for the reaction of OH with toluene, *J. Phys. Chem.*, **82**, 1095-1096, 1978.

Klotz, B., I. Barnes, B.T. Golding, and K.-H. Becker, Atmospheric chemistry of toluene-1,2-oxide/2-methyloxepin, *Phys. Chem. Chem. Phys.*, **2**, 227-235, 2000.

Knispel, R., R. Koch, M. Siese, and C. Zetzsch, Adduct formation of OH radicals with benzene, toluene, and phenol and consecutive reactions of the adducts with NO_x and O_2, *Ber. Bunsenges. Phys. Chem.*, **94**, 1375-1379, 1990.

Lipson, J.B., T.W. Beiderhase, L.T. Molina, M.J. Molina, and M. Olzmann, Production of HCl in the OH plus ClO reaction: laboratory measurements and statistical rate theory calculations, *J. Phys. Chem. A*, **103**, 6540-6551, 1999.

Markert, F., and P. Pagsberg, UV spectra and kinetics of radicals produced in the gas-phase reactions of Cl, F, and OH with toluene, *Chem. Phys. Lett.*, **209**, 445-454, 1993.

Molina, M.J., R. Zhang, K. Broekhuizen, W. Lei, R. Navarro, and L.T. Molina, Experimental study of intermediates from OH-initiated reactions of toluene, *J. Am. Chem. Soc.*, **121**, 10225-10226, 1999.

Lide, D.R., *CRC Handbook of Chemistry and Physics*, 71st Ed., CRC Press, Boca Raton, 1990.

Sloane, T.M. and R.J. Brudzynski, The effect of internal energy on the addition of hydroxyl radicals and deuterium atoms to aromatic hydrocarbons, *J. Chem. Phys.,* **72**, 4394-4400, 1980.

Tuazon, E.C., H. MacLeod, R. Atkinson, and W.P.L. Carter, α-Dicarbonyl yields from the NO_x-air photooxidations of a series of aromatic hydrocarbons in air, *Environ. Sci. Technol.*, **20**, 383-387, 1986.

Uc, V.H., I. García-Cruz, A. Hernández-Laguna, and A. Vivier-Bunge, New channels in the reaction mechanism of the atmospheric oxidation of toluene, *J. Phys. Chem. A.,* **104**, 7847-7855, 2000.

Villalta, P.W., L.G. Huey, and C.J. Howard, A temperature-dependent kinetics study of the CH_3O_2 + NO reaction using chemical ionization mass spectrometry, *J. Phys. Chem.*, **99**, 12829-12834, 1995.

Volkamer, R., U. Platt, and K. Wirtz, Primary and secondary glyoxal formation from aromatics: experimental evidence for the bicycloalkyl-radical pathway from benzene, toluene, and *p*-xylene, *J. Phys. Chem. A.,* **105**, 7865-7874, 2001.

Zhang, R., private communication, 2001.

Zielinska, B. and E.. Fujita, The composition and concentration of hydrocarbons in the range of C_2 to C_{20} in downtown Los Angeles, CA, *Res. Chem. Intermed.*, **20**, 321-334, 1994.

Chapter 5

Propene Oxidation Reactions

5.1 Introduction

A very important class of VOCs in the atmosphere is the alkenes. There are a wide variety of alkene sources in the atmosphere including anthropogenic sources such as fossil fuel combustion and biomass burning [*Finlayson-Pitts & Pitts*, 2001]. The largest source of alkenes to the atmosphere, however, is biogenic production of species such as isoprene and other terpenes [*Finlayson-Pitts & Pitts*, 2001]. These biogenic compounds are often complex in structure with multiple unsaturated C-C bonds. A number of commonly produced biogenic VOCs were shown previously (Figure 1-1).

The complexity of biogenic VOCs was a deterrent to the initial study of these molecules. Many have been shown to form low-volatility oxidation products which can form secondary organic aerosols similar to those formed in the oxidation of toluene [*Kavouras et al.*, 1999]. The initial study of alkene oxidation chemistry, therefore, focused on a lighter, more simple alkene, propene (C_3H_6). Propene is an important hydrocarbon in urban air due to its relatively

high concentrations (up to 50 ppb) and its high ozone forming potential [*Carter*, 1991]. The dominant source of propene in the atmosphere is incomplete combustion of fossil fuels, however biomass burning is also a source. There is a small oceanic source of propene as well, so it could also play a role in remote marine boundary layer chemistry [*Plassdulmer et al.*, 1995].

Propene is of particular interest because there has been very little study of the oxidation chemistry of hydrocarbons which form OH-adducts in the gas-phase such as the aromatics, alkenes and alkynes. The initial steps in the oxidation of these molecules are usually known, but the subsequent oxidation reactions and reaction rates have not been measured in most cases.

The initial oxidation of propene occurs by a variety of molecules:

$$C_3H_6 + OH \xrightarrow{M} C_3H_6OH \tag{5.1}$$

$$C_3H_6 + NO_3 \xrightarrow{M} C_3H_6ONO_2 \tag{5.2}$$

$$C_3H_6 + O_3 \longrightarrow Products \tag{5.3}$$

with rate constants $k_{5.1} = 2.63 \times 10^{-11}$ cm^3 molecule^{-1} s^{-1}, $k_{5.2} = 9.49 \times 10^{-15}$ cm^3 molecule^{-1} s^{-1}, $k_{5.3} = 1.01 \times 10^{-17}$ cm^3 molecule^{-1} s^{-1} at 298 K and 760 Torr total pressure [*Atkinson*, 1994]. Despite the differences in reaction rates, these loss processes will all be competitive in the troposphere. For an OH concentration of 1×10^6 molecules cm^3, an O_3 concentration of 2.6×10^{12} molecules cm^3 (100 ppb), and an NO_3 concentration of 2.8×10^9 molecules cm^3 (110 ppt) the lifetime of propene with respect to each of these oxidants is about 10 hours. The reaction of propene with NO_3 will be important at night when the NO_3 concentrations reach the ppt level, and the reaction with O_3 will be important in polluted areas with high O_3

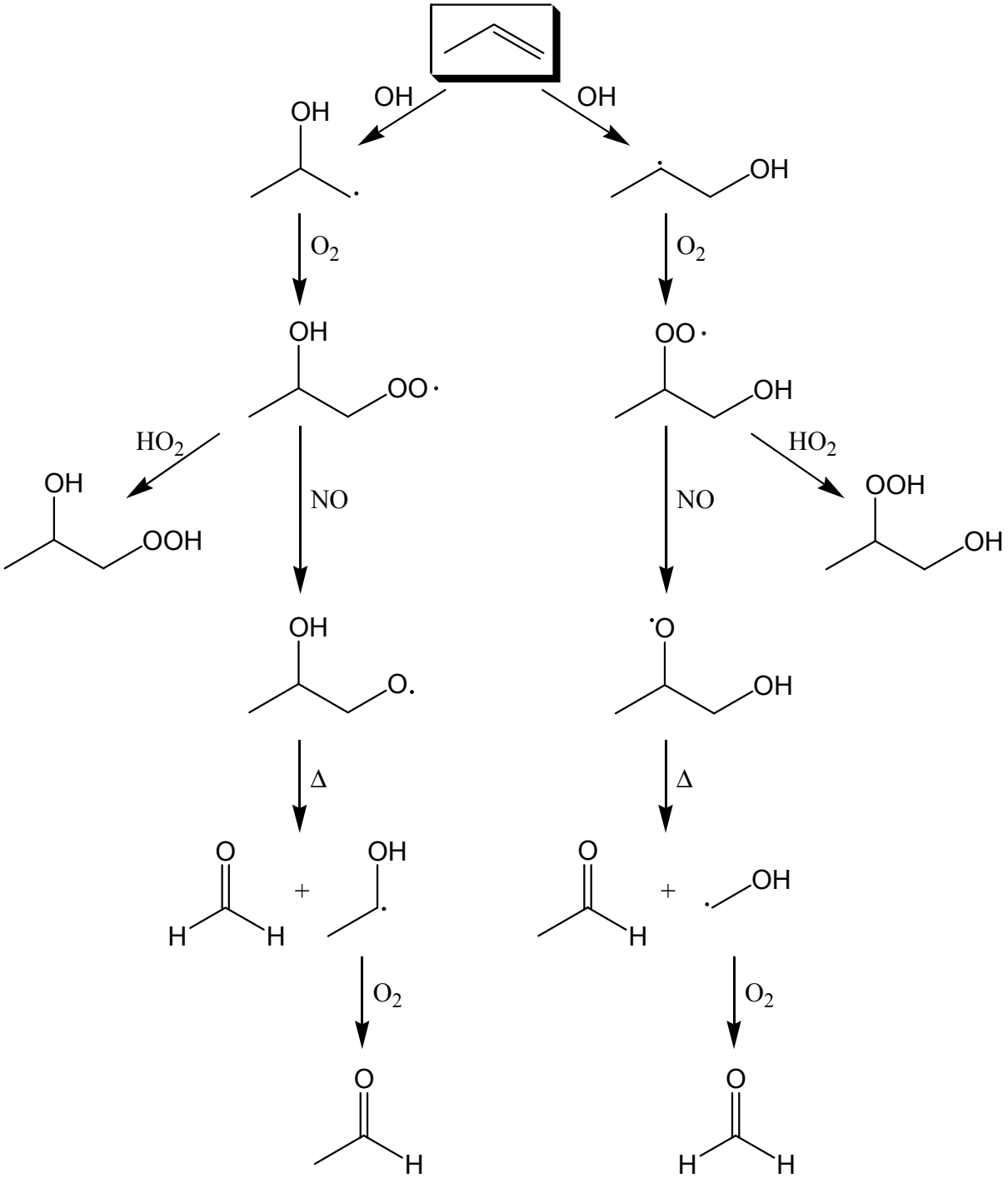

Figure 5-1: Proposed OH-initiated atmospheric oxidation mechanism of propene. Minor pathways have been omitted for simplicity. Propene has been highlighted at the top of the figure.

concentrations, however the reaction with OH is the dominant loss process under most daytime conditions.

The proposed mechanism for the OH-initiated oxidation of propene is shown in Figure 5-1. The reaction of propene with OH proceeds almost exclusively via OH addition to the double bond with H-atom abstraction accounting for <5% of the total reaction [*Atkinson*, 1994]. A summary of the studies to date of the reaction of OH with propene is given in Table 5.1.

Reference	$\mathbf{k}_{5.1}$	**Temp. range studied** (K)	**Method**[a]
Atkinson & Pitts, 1975[b]	2.51×10^{-11}	297-425	FP-RF
Zellner & Lorenz, 1984[c]	2.99×10^{-11}	298	FP-RF
Schmidt et al., 1985[d]	2.2×10^{-11}	295	FP-LIF
Nip & Paraskevopoulos, 1979[e]	2.46×10^{-11}	297	FP-RF
Tully & Goldsmith, 1985[f]	2.71×10^{-11}	293-896	FP-LIF
Ravishankara et al., 1978[g]	2.63×10^{-11}	298	FP-RF

Table 5.1: Comparison of room temperature rate constant values for the C_3H_6 + OH reaction. Rate constants are given in units of cm^3 $molecule^{-1}$ s^{-1}. [a]FP=flash photolysis, RP=resonance fluorescence, LIF=laser induced fluorescence. $k_{5.1}$ is given for [b]297 K and 100 Torr, [c]298 K and 96 Torr, [d]295 K and 760 Torr, [e]297 K and 55 Torr, [f]293 K and 200-400 Torr, [g]298 K and 200 Torr.

This reaction is also pressure dependent and exhibits fall-off behavior which can be described by the equation:

$$k_{5.1}(298\ K, M) = \left(\frac{k_0[M]}{1 + (k_0[M]/k_\infty)}\right) F^{\{1+[log(k_0[M]/k_\infty)]^2\}^{-1}} \tag{5.4}$$

where $k_0(298\ K) = 8.2 \times 10^{-27}$ cm^3 $molecule^{-1}$ s^{-1}, $k_\infty(298\ K) = 3.0 \times 10^{-11}$ cm^3 $molecule^{-1}$ s^{-1}, and F = 0.5[*Atkinson*, 1997]. The falloff curve at 298 K is shown in Figure 5-2. As shown in the figure, the reaction rate for propene + OH at 100 Torr is within 3% of the value at atmospheric pressure.

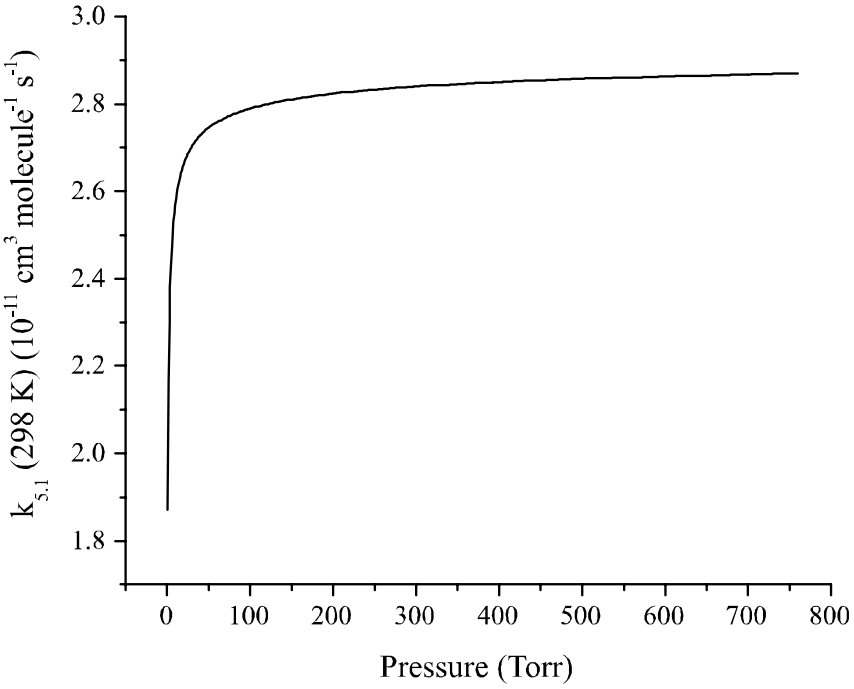

Figure 5-2: Pressure dependent falloff curve for the reaction of OH with propene.

The OH addition results in the formation of two β-hydroxypropyl radicals. These OH-propene adducts react quickly with O_2 to form two β-hydroxypropylperoxy radicals via Reaction 5.5:

$$C_3H_6OH + O_2 \xrightarrow{M} C_3H_6OHO_2 \tag{5.5}$$

with $k_{5.5} = 1.15 \times 10^{-11}$ cm^3 molecule^{-1} s^{-1} for the 1-hydroxypropyl radical at 296 K and 5 Torr and $k_{5.5} = 3.82 \times 10^{-12}$ cm^3 molecule^{-1} s^{-1} for the 2-hydroxypropyl radical at 296 K and 5 Torr [*Miyoshi et al.*, 1990]. These reactions appear to be at their high-pressure limits at 5 Torr total pressure [*Miyoshi et al.*, 1990].

There is very little experimental work done beyond this point in the oxidation mechanism of propene. The peroxy radicals formed by Reaction 5.5 are assumed to react with HO_2 under

low NO_x conditions and NO under high NO_x conditions.

$$C_3H_6OHO_2 + NO \longrightarrow C_3H_6(OH)O + NO_2 \quad (5.6)$$

$$C_3H_6OHO_2 + HO_2 \longrightarrow C_3H_6(OH)OOH + O_2 \quad (5.7)$$

The suggested rate coefficient for the reaction of the peroxy radicals with NO is 9×10^{-12} cm^3 $molecule^{-1}$ s^{-1} based on an estimate for the rate of the hydroxyethylperoxy radical ($HOCH_2CH_2OO$) + NO [*Becker et al.*, 1991] and the recommendation for the $\geq C_2$ alkylperoxy radical reactions with NO [*Atkinson*, 1994]. There is no recommendation for the rate of Reaction 5.7.

The β-hydroxypropoxy radicals formed in Reaction 5.6 have not been experimentally observed, but the "prompt" dissociation rate of the 1-hydroxy-2-propoxy radical has been theoretically determined to be 3.6×10^{12} exp(-7.05 kcal mol^{-1}/(RT)) s^{-1} at 1 atm giving a value of 2.4×10^7 s^{-1} for 298 K. The fate of the thermalized radicals is also expected to be dissociation. Due to these high dissociation rates, the fate of these radicals in the atmosphere is expected to be dissociation under all conditions [*Vereecken et al.*, 1999].

The dissociation of the two β-hydroxypropoxy radicals yields an aldehyde and an α-hydroxyalkyl radical for both isomers. The two α-hydroxyalkyl radicals react with O_2:

$$CH_2OH + O_2 \longrightarrow HCHO + HO_2 \quad (5.8)$$

$$CH_3CHOH + O_2 \longrightarrow CH_3CHO + HO_2 \quad (5.9)$$

with rate constants $k_{5.8} = 1.17 \times 10^{-11}$ cm^3 $molecule^{-1}$ s^{-1} and $k_{5.9} = 2.8 \times 10^{-11}$ cm^3

molecule^{-1} s^{-1} [*Miyoshi et al.*, 1990; *Miyoshi et al.*, 1989]. For both β-hydroxypropoxy radicals, therefore, the final aldehydes formed are acetaldehyde and formaldehyde in the presence of O_2. A number of studies have indeed found a unity production of both aldehydes for the propene-OH-NO_x-O_2 reaction system [*Niki et al.*, 1978; *Vereecken et al.*, 1999].

A number of steps in the oxidation mechanism of propene have been studied, however many intermediate species have not been directly detected and the kinetics of the reactions of these species have not been measured. There are very few experimental studies in general of the reactions of multifunctional organic radicals such as α- or β-hydroxyalkyl or peroxy radicals, so there is a need to expand the base of knowledge concerning the reactions of these species.

5.2 Temperature Dependence of the Reaction of Propene with OH

5.2.1 Introduction

The rate for the reaction of propene with OH has been studied over a variety of pressures and temperatures as was described in the previous section. However, the measurements have not been extended into atmospherically relevant temperatures. This reaction was therefore studied as a test to insure that the reaction of propene with OH did not produce the same behavior observed in the toluene experiments and to extend the current temperature range of the measurements to atmospherically relevant temperatures.

5.2.2 Experimental setup

Due to the problems encountered in the experimental studies of the reactions of toluene (Chapter 4) and the somewhat limited sensitivity of the UTI 100C instrument, the propene experiments were performed on an ABB mass spectrometer (Extrel Merlin). The mass spectrometer has been described in detail elsewhere [*Smith*, 2000], however modifications made for this experiment are described below.

The experimental setup consisted of a 48" long, 1" i.d. jacketed pyrex flow tube coated with halocarbon wax (Halocarbon Products, Inc.). The reaction time in the flow tube was varied with a 5' long, $\frac{1}{4}$" o.d. pyrex moveable injector also coated with halocarbon wax. The rear of the flow tube had a sidearm for radical generation and two ports for the introduction of other gases. The injector was housed in $\frac{3}{8}$" o.d. flexible teflon tubing which was sealed from the atmosphere, but open to the flow tube. This design allowed the injector to be easily moved without the danger of laboratory air leaking into the flow tube. The flow tube was connected to the mass spectrometer via a pyrex adapter through a 90° bend. Ions were created using a radioactive ^{210}Po ionization source Nuclecel P-2031). Ions were introduced into the chemical ionization region via a $\frac{1}{4}$" o.d. stainless steel tube. The 90° configuration allowed the ion-molecule reaction time to be changed in the middle of an experiment simply by inserting the stainless steel tube closer to the mass spectrometer, therefore reducing the ion-molecule reaction distance. The ion-molecule region was also coated with halocarbon wax.

The main carrier gas was injected at the rear of the flow tube and was a 50 STP L min^{-1} flow of UHP N_2 (BOC 99.999%). A 2 STP L min^{-1} flow of UHP He (BOC 99.997%) was added to the injector as a sweep gas and a 1-10 STP cm^3 min^{-1} flow of a 0.3% mixture of propene

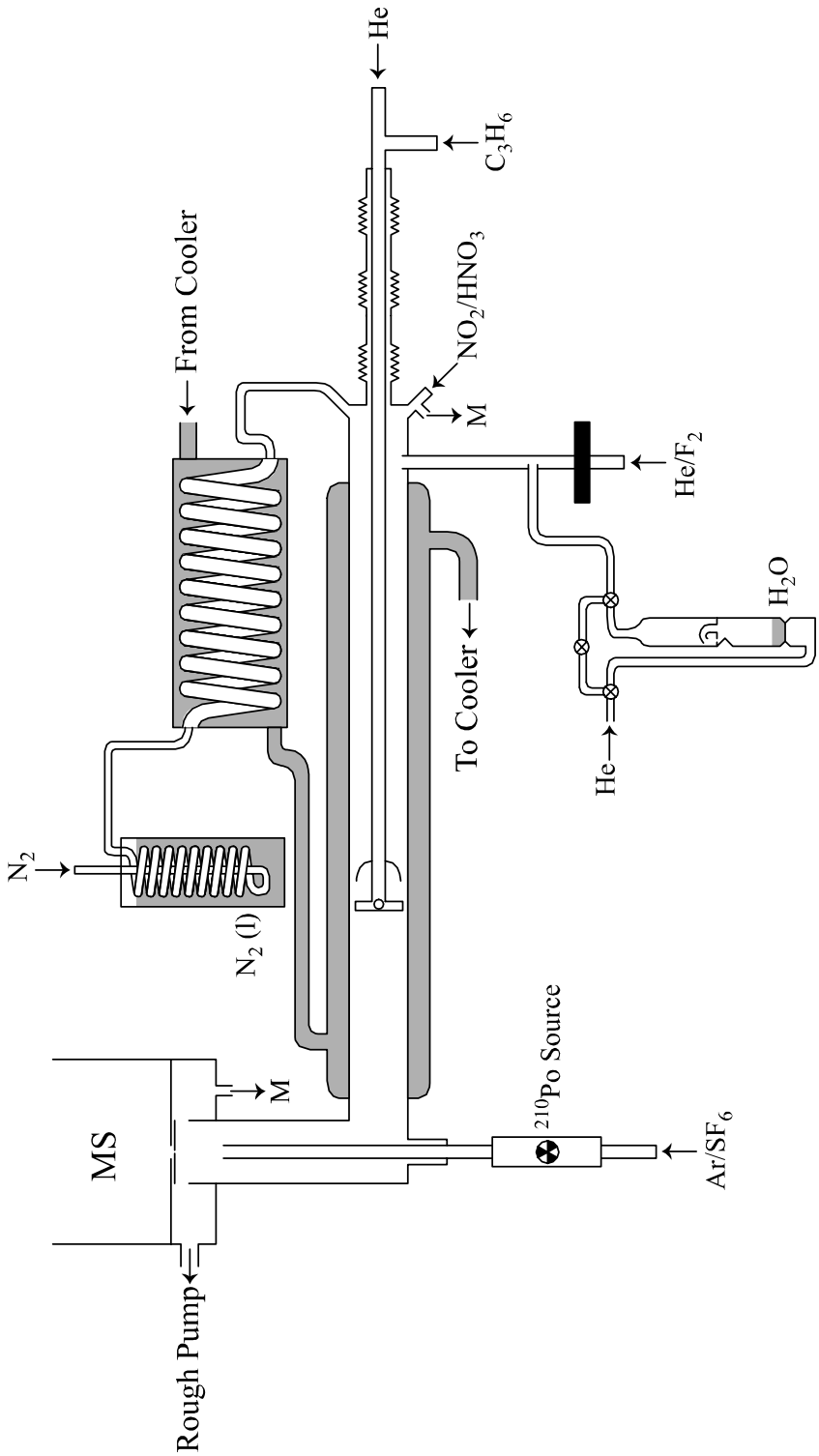

Figure 5-3: Experimental setup for the measurement of the temperature dependent rate coefficient of the reaction of propene and OH.

(BOC 99%) and UHP N_2 was also added to the injector. OH was produced in the side arm via the reaction of F + H_2O (Reaction 4.19). A 3 STP L min^{-1} flow of UHP He was mixed with a 0.2 STP cm^3 min^{-1} flow of an F_2 mixture (Matheson 2.0% in He) and was passed through the microwave discharge cavity operating a 2.45 GHz and 12 W. A 5 STP cm^3 min^{-1} flow of UHP He was passed through a fritted bubbler containing H_2O held at 0°C and this saturated flow was introduced downstream of the microwave discharge.

The chemical ionization scheme utilized SF_6^- to detect OH (Reaction 4.18), NO_2, and HNO_3. O_2^+ was used for the detection of propene:

$$C_3H_6 + O_2^+ \longrightarrow C_3H_6^+ + O_2 \tag{5.10}$$

$$SF_6^- + NO_2 \longrightarrow SF_6 + NO_2^- \tag{5.11}$$

$$SF_6^- + HNO_3 \longrightarrow [HNO_3 \cdot F]^- + Products \tag{5.12}$$

SF_6^- ions were produced by adding a 5 STP L min^{-1} flow of UHP Ar (BOC 99.998%) and a 0.1 STP cm^3 min^{-1} flow of SF_6 (Matheson 99.99%) to the polonium source. The O_2^+ ion were produced by passing a 5 STP L min^{-1} flow of UHP Ar through a molecular sieve trap at 77 K to remove water and then adding the dry Ar flow to the polonium source All flows were measured with calibrated mass flow meters (Tylan 360).

The pressure in the flow tube and ionization region was maintained at 100 Torr under flow conditions by a Varian SD-700 rotary vane pump. Pressures were measured at the front and rear of the flow tube by a capacitance manometer (MKS Baratron). The front aperture of the mass spectrometer chamber was 50 μm and the pressure in the quadrupole chamber was 9 $\times$ 10^{-6} Torr under flow conditions.

The low temperature measurements were performed by cooling the main 50 STP L min^{-1} N_2 flow in a copper cooling coil immersed in liquid nitrogen at 77 K. A Neslab (LT-50) cooler cycled cooling fluid (Dow Syltherm XLT) through a gas heat-exchanger and then through the jacketed flow tube. The N_2 from the copper cooling coil was equilibrated with the flow tube temperature in the gas heat-exchanger and then entered the flow tube. A type-T thermocouple was mounted to the end of the moveable injector in the center of the flow tube to measure the gas temperature. The temperature over the length of the flow tube was stable to ±1 K. The entire cooling system including coolant transfer lines, flow tube, chemical ionization region, heat exchanger and N_2 gas lines was insulated to prevent heat loss and temperature gradients. A schematic of the experimental setup is shown in Figure 5-3.

5.2.3 Experiments and results

The experiments were performed under pseudo-first order conditions with [propene]>>[OH]. This condition was verified by two methods. First, the propene signal was monitored with O_2^+ as a function of reaction time with OH for the lowest propene concentration used in the experiments, 3×10^{11} molecules cm^{-3}. The $C_3H_6^+$ signal remained constant to within 10% for all reaction times. Therefore, the OH concentration was assumed to be $\leq 3 \times 10^{10}$ molecules cm^{-3}. The OH was also titrated completely with NO_2 to form HNO_3 via Reaction 5.13:

$$OH + NO_2 \xrightarrow{M} HNO_3 \tag{5.13}$$

with $k_{5.13} = 3.4 \times 10^{-12}$ cm^3 $molecule^{-1}$ s^{-1} at 100 Torr and 298 K. The HNO_3 signal was then calibrated by passing 1-10 STP cm^3 min^{-1} UHP N_2 through a fritted bubbler containing

a 48.6% wt. HNO_3/H_2O solution at 0°C. This solution had an HNO_3 vapor pressure of 0.036 Torr at 0°C. Both the NO_2 and the HNO_3 were introduced in the back of the flow tube as shown in Figure 5-3. This titration method confirmed that the OH concentration ranged from 1-5 $\times$ 10^{10} molecules cm^{-3} for all experiments.

The OH signal at m/e 17 was monitored as a function of reaction time for a variety of propene concentrations. A simple exponential decay $y = ae^{-bx}$ was fit to the data and the resulting pseudo-first order decay rates, k_{1st}, were plotted as a function of [propene]. The second order rate coefficient was the slope of the linear least-squares fit to -k_{1st} vs. [propene]. This procedure was repeated for a variety of temperatures ranging from 237-303 K. The plots for 296 K are given in Figure 5-4 and 5-5. The results for the temperature dependent studies are given in Table 5.2. The current recommendation for the temperature dependent rate coefficient for the reaction of propene with OH at 760 Torr is

$$k(T) = Ae^{-B/T} \qquad T \leq 425\ K \tag{5.14}$$

where A = $(4.85^{+0.65}_{-0.58})$ $\times$ 10^{-12} cm^3 $molecule^{-1}$ s^{-1} and B = (-504±45) K [*Atkinson*, 1985]. These values are based on the fit of Equation 5.14 to the temperature dependent data given previously in Table 5.1. The data given in Table 5.2 was plotted in Figure 5-6 and the Arrhenius expression derived from the linear least-squares fit to the data was k(T) = (3.1 ± 1.2) $\times$ 10^{-12} $e^{((624\pm100)/T)}$ cm^3 $molecule^{-1}$ s^{-1}. The error in these values represents the two standard deviation statistical error in the data and does not take systematic error into account. These experimental values agree very well with the recommended values within the error limits. The updated recommendation for the Arrhenius expression based on the linear least-squares

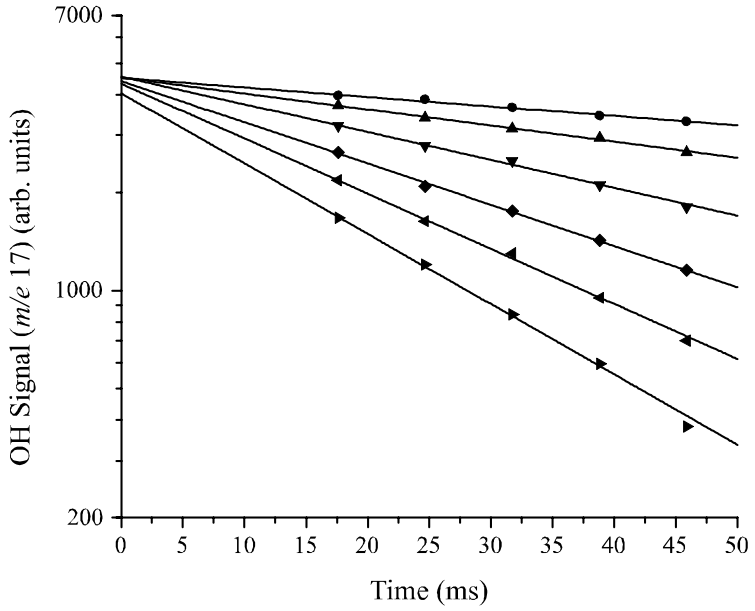

Figure 5-4: Pseudo-first order decays of OH as a function of reaction time with propene. Lines represent non-linear least-squares fits to the data. Propene concentrations range from (●) 3.0 $\times$ 10^{11} molecules cm^{-3} to (▶) 2.1 $\times$ 10^{12} molecules cm^{-3}.

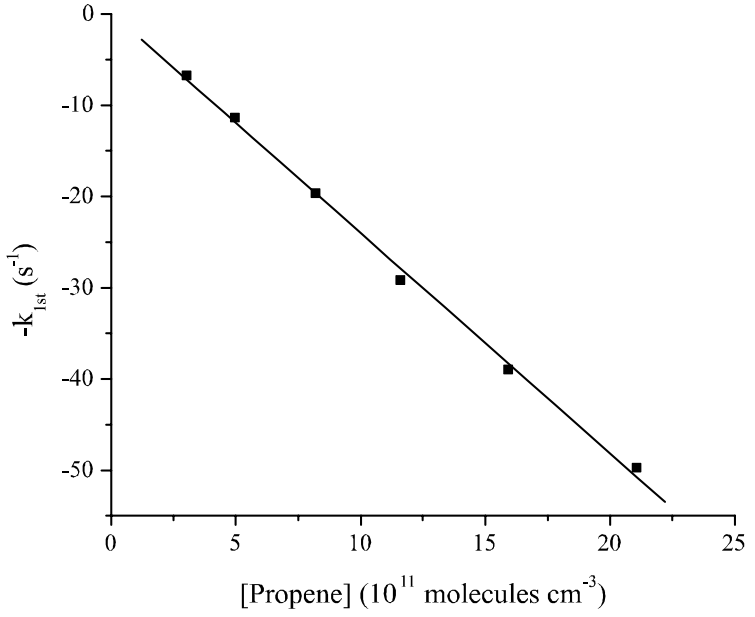

Figure 5-5: Pseudo-first order decay rates, k_{1st}, vs. [propene]. The second order decay rate is the slope of the linear least-squares fit (m = 2.60 $\times$ 10^{-11} cm^3 $molecule^{-1}$ s^{-1}.

T (K)[a]	**P (Torr)**[b]	$\mathbf{k}_{5.1} \pm 2\sigma$ [c]
237	100	$(4.49 \pm 1.12) \times 10^{-11}$
246	99.7	$(3.83 \pm 1.01) \times 10^{-11}$
257	99.9	$(3.38 \pm 0.96) \times 10^{-11}$
264	100.2	$(3.33 \pm 0.96) \times 10^{-11}$
271	100	$(3.02 \pm 0.84) \times 10^{-11}$
277	99.8	$(2.82 \pm 0.75) \times 10^{-11}$
281	100.1	$(2.99 \pm 0.78) \times 10^{-11}$
284	100.2	$(2.74 \pm 0.72) \times 10^{-11}$
287	99.8	$(2.71 \pm 0.69) \times 10^{-11}$
295	100	$(2.56 \pm 0.65) \times 10^{-11}$
296	100	$(2.60 \pm 0.59) \times 10^{-11}$
298	99.7	$(2.55 \pm 0.73) \times 10^{-11}$
303	100.1	$(2.40 \pm 0.54) \times 10^{-11}$

Table 5.2: Summary of the experimental conditions and rate constants measured for the C_3H_6 + OH reaction. [a]Temperatures are ±1 K. [b]Pressures are ±1 Torr. [c]Rate constants are given in units of cm^3 $molecule^{-1}$ s^{-1}. The error represents the two standard deviation statistical error in the data and is not an estimate of systematic error.

fit to the entire data set shown in Figure 5-7 is $k(T) = (4.40^{+0.31}_{-0.30}) \times 10^{-12}$ $e^{((527\pm22)/T)}$ cm^3 $molecule^{-1}$ s^{-1}. This does not represent a significant change in the Arrhenius expression for this reaction and the recommended rate coefficient at 298 K would only change from 2.63×10^{-11} cm^3 $molecule^{-1}$ s^{-1} to 2.58×10^{-11} cm^3 $molecule^{-1}$ s^{-1}.

This initial study was successful in extending the measurements for the propene-OH reaction to tropospherically relevant temperatures and also encouraged further studies into the mechanism of the atmospheric oxidation of propene.

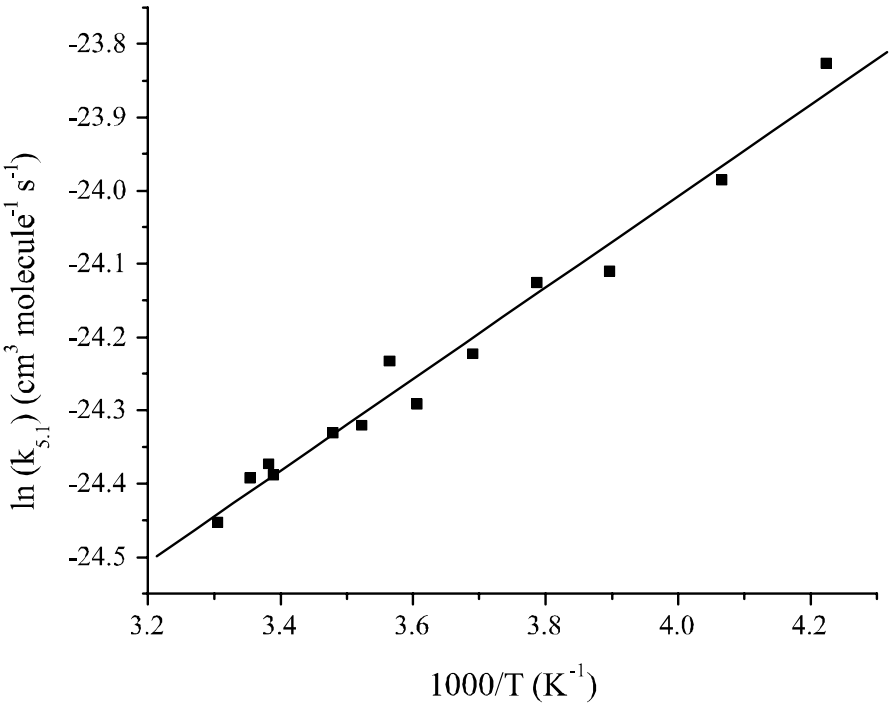

Figure 5-6: Arrhenius plot for the measured rate coefficients for the reaction of propene + OH. The line is a linear least-squares fit to the data.

5.3 Temperature Dependence of the β-Hydroxypropylperoxy Radical + NO

5.3.1 Introduction

The reaction of the propene-OH adduct with O_2 proceeds very rapidly at 100 Torr ($>3 \times 10^{-12}$ cm^3 molecule^{-1} s^{-1}) for both isomers [*Miyoshi et al.*, 1990]. The oxygen impurity in the UHP N_2 carrier gas is nominally 1 ppm, so for 100 Torr of UHP N_2, the ambient O_2 concentration in the flow tube was $\sim 4 \times 10^{12}$ molecules cm^{-3}. This O_2 concentration results in decay rates of >15 s^{-1} for both isomers in the presence of O_2. It was therefore difficult to detect and measure the kinetics of the propene-OH adduct without costly purification of a 50 STP L min^{-1} flow of

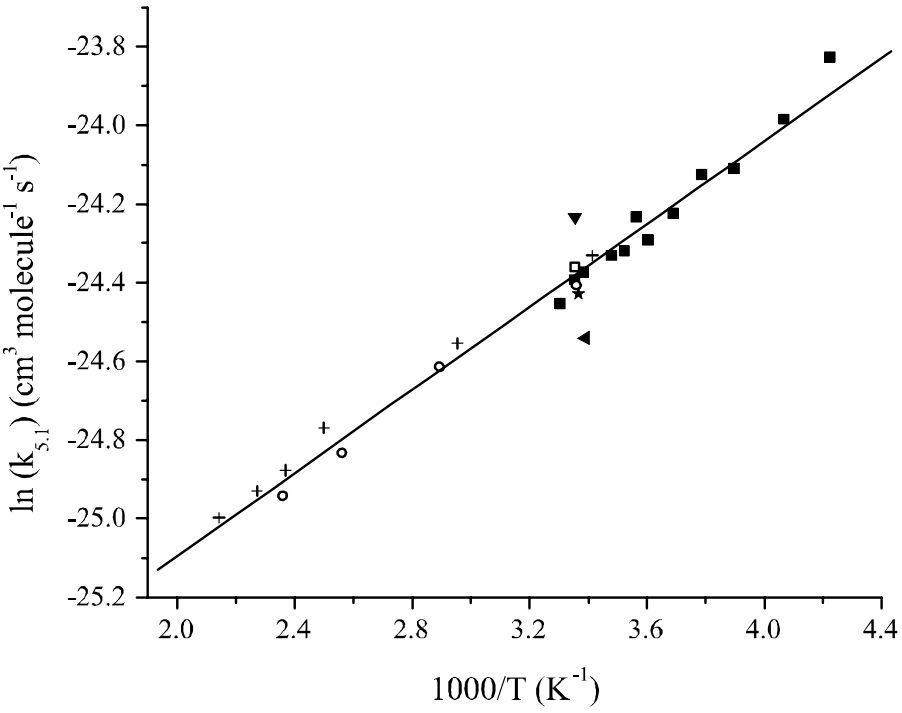

Figure 5-7: Arrhenius plot of the temperature dependent rate coefficients for the propene reaction with OH. (■) This work, (◄) Schmidt et al., (▼) Zellner & Lorenz, (○) Atkinson & Pitts, (★) Nip & Paraskevopoulos, (+) Tully & Goldsmith, (□) Ravishankara et al.

UHP N_2. With these reaction rates, however, the only fate of the adducts in the atmosphere is reaction with O_2, therefore the next species of interest in the oxidation mechanism are the β-hydroxypropylperoxy radicals.

Figure 5-8: The two β-hydroxypropylperoxy radicals formed in the atmospheric oxidation of propene.

The kinetics of the reactions of these radicals with NO, NO_2, HO_2, and RO_2 have not been measured. There are few if any measurements of the kinetics of any β-hydroxyperoxy radicals

including the important radicals formed in the oxidation of biogenic VOCs such as isoprene. The likely fate of these radicals in a polluted atmosphere is reaction with NO, however the reaction with RO_2 and HO_2 may become important under low NO_x conditions.

5.3.2 Experimental setup

The experimental setup was described in detail in Section 5.2.2, however some modifications were made. The peroxy radicals were produced in the sidearm via the reaction of OH with a mixture of C_3H_6 and O_2 (Reaction 5.1 and 5.5). A 3 STP L min^{-1} flow of UHP He was mixed with 0.05 STP cm^3 min^{-1} of a 2% mixture of F_2 in He. This flow was passed through the microwave discharge cavity operating at 2.45 GHz and 8 W. A 5 STP cm^3 min^{-1} flow of UHP He saturated in water vapor was introduced downstream of the microwave cavity. the water vapor concentration was large enough in the sidearm to titrate >99.9% of the F atoms to OH in 1 ms of reaction time. Approximately 2 ms downstream of the water vapor injection port, a 6% mixture of C_3H_6 (BOC 99%) in UHP N_2 (1.5 STP cm^3 min^{-1}) and a 30 STP cm^3 min^{-1} flow of UHP O_2 were injected into the sidearm. The OH was converted (>99%) into the peroxy radicals of interest in the 3 ms of reaction time before they entered the flow tube. The OH was titrated as described in Section 5.2.2 with NO_2. The OH concentration was kept below 5 $\times$ 10^{10} molecules cm^{-3} in the flow tube to minimize self-reactions of the peroxy radicals in the flow tube and sidearm. A schematic of the experimental setup is shown in Figure 5-9.

NO was purified as described in Section 3.2.1 and a 2.5% mixture of purified NO in UHP N_2 (1-10 STP cm^3 min^{-1}) was mixed with 2 STP L min^{-1} of UHP He and introduced through the moveable injector. An OH scavenger could be introduced through the injection port at the rear of the flow tube. A 20% mixture of isoprene (C_5H_8) (Aldrich 99%) in UHP N_2 was

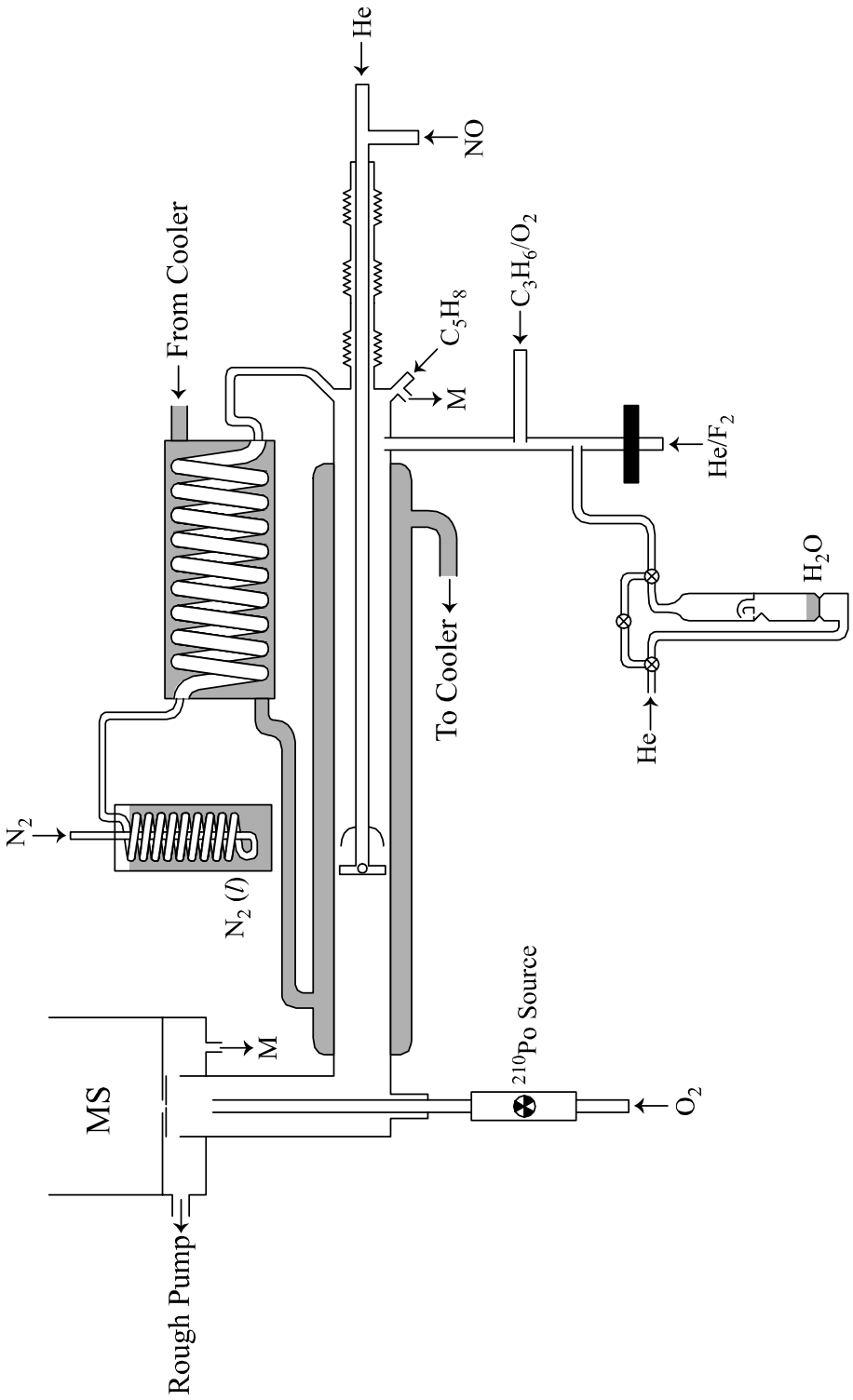

Figure 5-9: Experimental setup for measuring the kinetics of the reaction of the β-hydroxypropylperoxy radicals with NO.

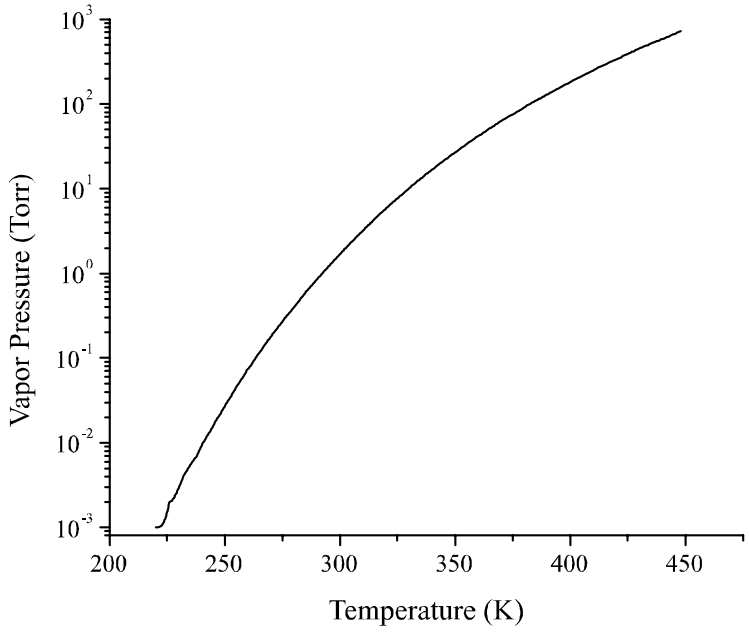

Figure 5-10: Plot of the vapor-pressure of α-terpinene as a function of temperature [*Yaws*, 1994].

introduced (10 STP cm^3 min^{-1}) through the port. Also, a 20 STP cm^3 min^{-1} flow of UHP N_2 was passed through a fritted bubbler containing α-terpinene ($C_{10}H_{16}$) (Aldrich 85+%) at 25°C. The vapor pressure of α-terpinene as a function of temperature is shown in Figure 5-10. The vapor pressure of α-terpinene at 25°C is 1.5 Torr which is sufficient for these experiments.

The chemical ionization scheme utilized the reactions of O_2^- for the detection of the species of interest. O_2^- has been previously used to detect peroxy radicals [*Eberhard et al.*, 1996]. The

chemical ionization reactions of interest were:

$$O_2^- + OH \longrightarrow OH^- + O_2 \tag{5.15}$$

$$O_2^- + NO \longrightarrow NO_3^- \tag{5.16}$$

$$O_2^- + NO_2 \longrightarrow NO_2^- + O_2 \tag{5.17}$$

$$O_2^- + HNO_3 \longrightarrow [O_2 \cdot HNO_3]^- \tag{5.18}$$

$$O_2^- + C_3H_6OHO_2 \longrightarrow C_3H_6OHO_2^- + O_2 \tag{5.19}$$

The O_2^- was formed by passing 5 STP L min^{-1} UHP O_2 through a molecular sieve trap at 77 K to remove traces of H_2O and then through the radioactive polonium ion source. The dominant peak observed was at m/e 50 under experimental conditions due to the water vapor used in the OH radical source. The peak at m/e 50 corresponds to $O_2^- \cdot H_2O$. This did not affect the ionization scheme detailed above, however.

The flow tube chemistry was modeled and a complication was discovered. The OH radical initiator, and therefore the peroxy radical of interest, is recycled quickly in the flow tube according to the reaction pathway shown in Figure 5-11. Only one isomer is shown in the figure for simplicity. This phenomenon has been seen before in the reaction cycles of isoprene and ethene and the measurement of the rate of OH propagation has even been used to estimate rate constants in the cycle [*Stevens et al.*, 1999; *Becker et al.*, 1991]. The OH propagation chain in the flow tube was modeled using the reactions in Table 5.3.

The β-hydroxypropylperoxy radical profiles as a function of time were modeled under typical experimental conditions and for a variety of NO conditions. An OH radical scavenger such as isoprene was then added to the model. It was assumed that the β-hydroxypropylperoxy

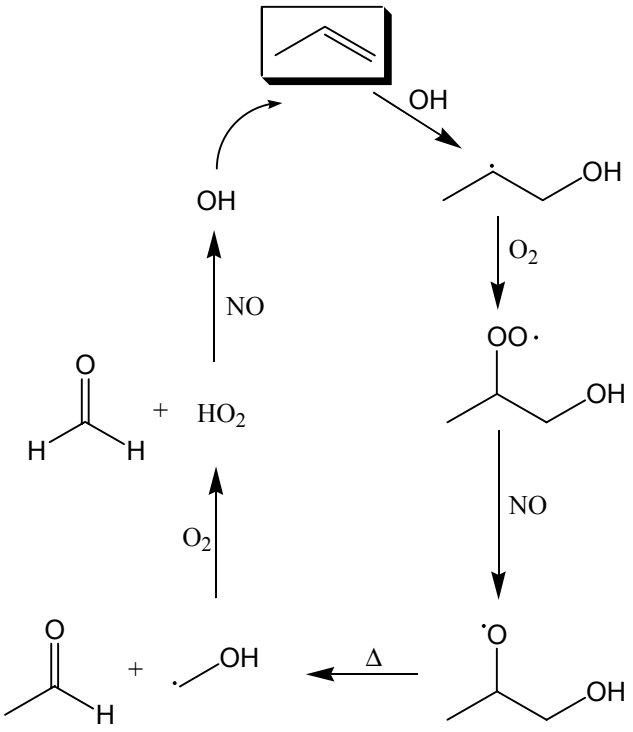

Figure 5-11: OH radical propagation chain in the propene-OH-O_2-NO system.

radicals were not formed in the reactions of isoprene, which is a reasonable assumption based on the proposed oxidation mechanism of isoprene. The β-hydroxypropylperoxy radical profiles as a function of time were again modeled under the same conditions used in the previous model. The results are plotted in Figures 5-12 and 5-13. The decays in Figure 5-12 are very non-linear on a semi-log scale and the chemistry would have to be modeled to extract a rate constant for this reaction. The decays in Figure 5-13, however, are linear on a semi-log plot and follow pseudo-first order conditions if $[NO] >> [C_3H_6OHO_2]$.

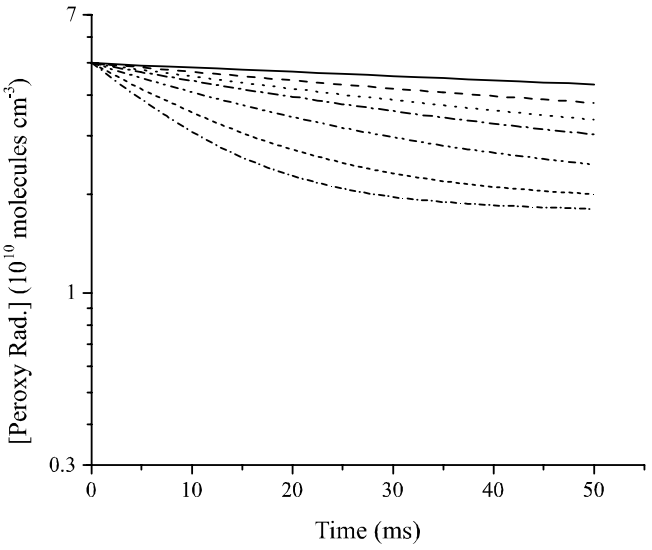

Figure 5-12: β-hydroxypropylperoxy radical decays as a function of time for various NO concentrations ranging from (—) 3×10^{11} molecules cm^{-3} to (–·–) 5×10^{12} molecules cm^{-3}. Initial concentrations used in the model were $[C_3H_6]_0 = 5.6 \times 10^{12}$ molecules cm^{-3}, $[O_2]_0 = 2 \times 10^{15}$ molecules cm^{-3}, and $[C_3H_6OHO_2]_0 = 5 \times 10^{10}$ molecules cm^{-3}.

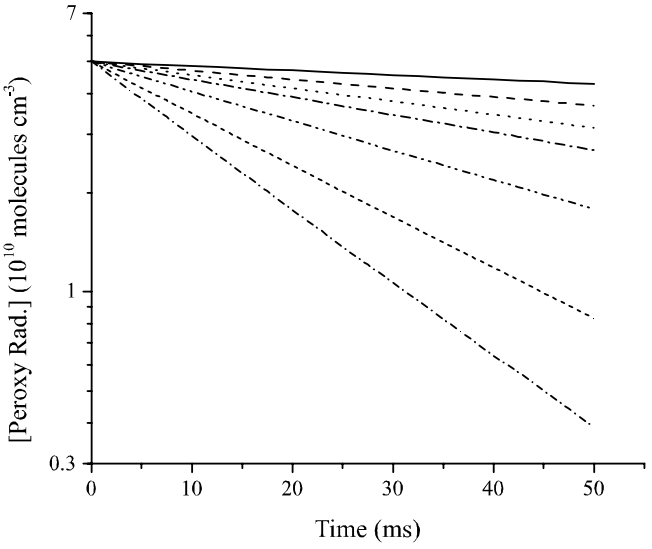

Figure 5-13: β-hydroxypropylperoxy radical decays in the presence of an OH scavenger as a function of time for various NO concentrations ranging from (—) 3×10^{11} molecules cm^{-3} to (–·–) 5×10^{12} molecules cm^{-3}. Initial concentrations used in the model were the same as Figure 5-12 with $[C_5H_8]_0 = 8 \times 10^{13}$ molecules cm^{-3}.

Reaction	**Rate**[a]
$C_3H_6 + OH \xrightarrow{M} CH_3CH(OH)CH_2$	9.45×10^{-12}
$C_3H_6 + OH \xrightarrow{M} CH_3CHCH_2OH$	1.76×10^{-11}
$CH_3CH(OH)CH_2 + O_2 \xrightarrow{M} CH_3CH(OH)CH_2OO$	3.82×10^{-12}
$CH_3CHCH_2OH + O_2 \xrightarrow{M} CH_3CH(OO)CH_2OH$	1.16×10^{-11}
$CH_3CH(OH)CH_2OO + NO \rightarrow CH_3CHOH + HCHO + NO_2$	1.0×10^{-11}
$CH_3CH(OO)CH_2OH + NO \rightarrow CH_3CHO + CH_2OH + NO_2$	1.0×10^{-11}
$CH_2OH + O_2 \rightarrow HCHO + HO_2$	9.4×10^{-12}
$CH_3CHOH + O_2 \rightarrow CH_3CHO + HO_2$	1.9×10^{-11}
$HO_2 + NO \rightarrow OH + NO_2$	8.1×10^{-12}
$OH + NO \xrightarrow{M} HONO$	1.7×10^{-12}
$OH + NO_2 \xrightarrow{M} HNO_3$	3.4×10^{-12}
$OH + HCHO \rightarrow H_2O + HCO$	1.0×10^{-11}
$OH + CH_3CHO \rightarrow H_2O + CH_3CO$	1.4×10^{-11}
$HCO + O_2 \rightarrow CO + HO_2$	5.5×10^{-12}
$CH_3CO + O_2 \xrightarrow{M} CH_3C(O)OO$	3.0×10^{-12}
$CH_3C(O)OO + NO \rightarrow CH_3 + CO_2 + NO_2$	1.8×10^{-11}
$CH_3 + O_2 \xrightarrow{M} CH_3O_2$	4.8×10^{-13}
$CH_3O_2 + NO \xrightarrow{M} CH_3O + NO_2$	7.7×10^{-12}

Table 5.3: Chemical reactions used in kinetic modeling. Rate constants are given for 100 Torr and 298 K and are in units of cm^3 $molecule^{-1}$ s^{-1}. [a][*Atkinson*, 1994], [*DeMore et al.*, 1997].

5.3.3 Experiments and results

The peak at *m/e* 91 present when the OH radical source was operating and the propene and O_2 were added to the side arm was attributed to the peroxy radical of interest. Confirmation of this assignment was desired, however, so experiments were performed using the setup described previously in Section 5.2.2. The OH was produced in the sidearm and the propene was introduced through the injector. A large excess of O_2 (10^{15} molecules cm^{-3}) was injected in the flow tube so that the propene-OH reaction was the rate limiting step in the formation of the peroxy radical. Using O_2^- as the ionization reagent, the OH^- and $C_3H_6OHO_2^-$ peaks were simultaneously monitored as a function of reaction time for various propene concentrations. The OH decays were correlated to a rise in the signal at *m/e* 91. The results of these

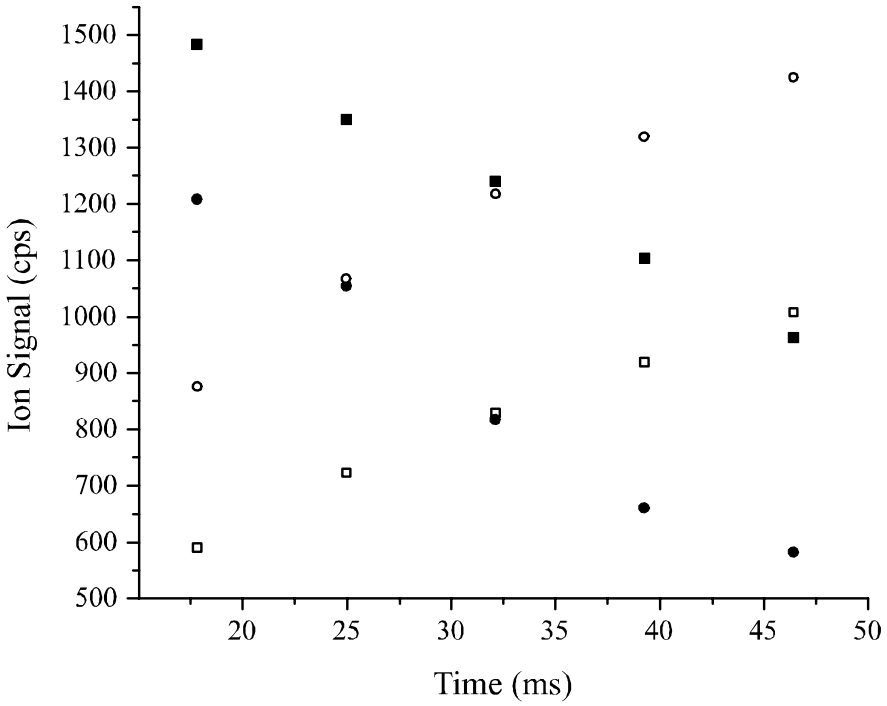

Figure 5-14: OH signal decay and peroxy radical signal rise as a function of time for two propene concentrations. The filled symbols (■,●) represent the OH signals and the corresponding open symbols (□,○) represent the m/e 91 signals.

experiments for two propene concentrations are shown in Figure 5-14. The OH decays and corresponding rise in the m/e 91 peak were very well correlated and this was the confirmation that was needed to proceed to the measurements of the peroxy radical decays.

The reaction setup was changed to that described in the previous section (Section 5.3.2) in order to measure the kinetics of the reaction of the peroxy radicals with NO. The first experiments were performed to determine if the choice of OH scavenger had an effect on the chemistry in the flow tube and the detection of the propene peroxy radicals at m/e 91. Two OH scavengers were used, the first being isoprene (C_5H_8) and the second being α-terpinene ($C_{10}H_{16}$) (Figure 1-1). These two molecules were chosen because of their fast reaction rate

with OH:

$$C_5H_8 + OH \xrightarrow{M} C_5H_8OH \tag{5.20}$$

$$C_{10}H_{16} + OH \xrightarrow{M} C_{10}H_{16}OH \tag{5.21}$$

($k_{5.20} = 1.01 \times 10^{-10}$ cm^3 molecule^{-1} s^{-1}, $k_{5.21} = 3.63 \times 10^{-10}$ cm^3 molecule^{-1} s^{-1} at 1 atm and 298 K) [*Atkinson*, 1994]. The decay of the β-hydroxypropylperoxy radical signal as a function of time was measured for various NO concentrations in the presence of both isoprene and α-terpinene at 293 K. The decay profiles are given in Figures 5-15 and 5-16.

The decay profiles are similar for both OH scavengers used. In both cases the OH loss rate in the flow tube with respect to the scavenger was 50 times higher than the OH loss rate with respect to propene. The pseudo-first order decays were linear on a semi-log plot which implies that the scavengers were successful in preventing the OH radical propagation from regenerating the propene peroxy radicals. This also suggests that within experimental error, both peroxy isomers react with NO at the same rate (within 10%). The observed decays would be bi-exponential if the two isomers reacted with very different rates. This result is not surprising since the structures of the two isomers are very similar.

The pseudo-first order decay rates from Figures 5-15 and 5-16 were determined from a non-linear least-squares fit to the data ($y = ae^{bx}$). The pseudo-first order decay rates in the presence of both scavengers were plotted as a function of NO concentration in Figure 5-17. The results are very similar for the two scavengers. Linear least-squares fits to the data yielded the second order decay rates: $k_{5.6}$ (isoprene scavenger) = $(1.05 \pm 0.18) \times 10^{-11}$ cm^3 molecule^{-1} s^{-1} and $k_{5.6}$ (terpinene scavenger) = $(9.95 \pm 0.17) \times 10^{-12}$ cm^3 molecule^{-1} s^{-1}. These values are

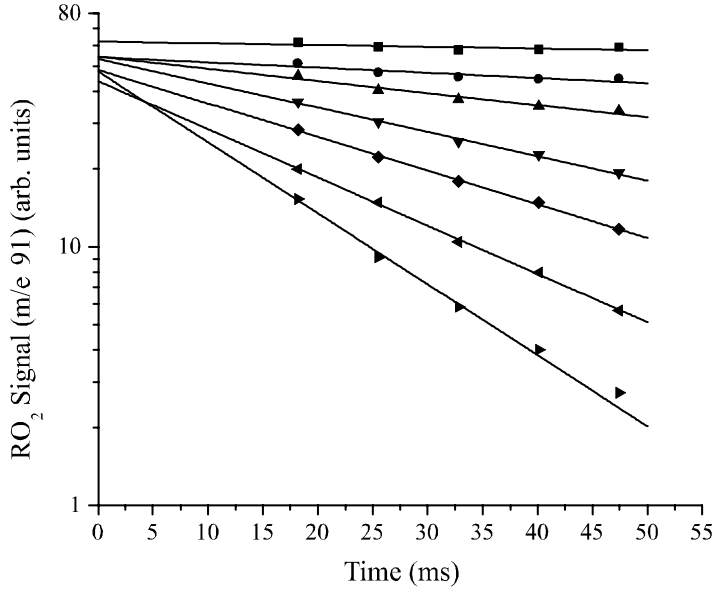

Figure 5-15: Pseudo-first order decays of the β-hydroxypropylperoxy radical as a function of time for various NO concentrations ranging from (•) 3.2×10^{11} molecules cm^{-3} to (►) 6.0×10^{12} molecules cm^{-3}. Isoprene was the OH scavenger for this experiment.

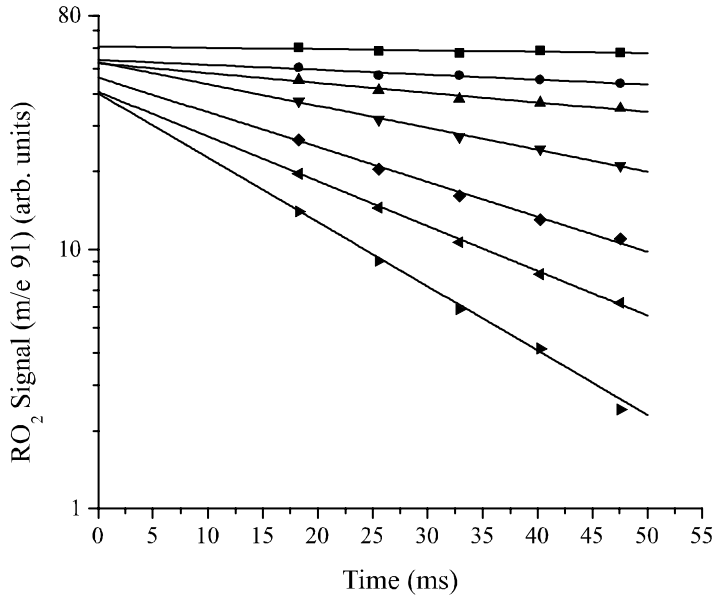

Figure 5-16: Pseudo-first order decays of the β-hydroxypropylperoxy radical as a function of time for various NO concentrations ranging from (•) 2.5×10^{11} molecules cm^{-3} to (►) 6.1×10^{12} molecules cm^{-3}. α-Terpinene was the OH scavenger for this experiment.

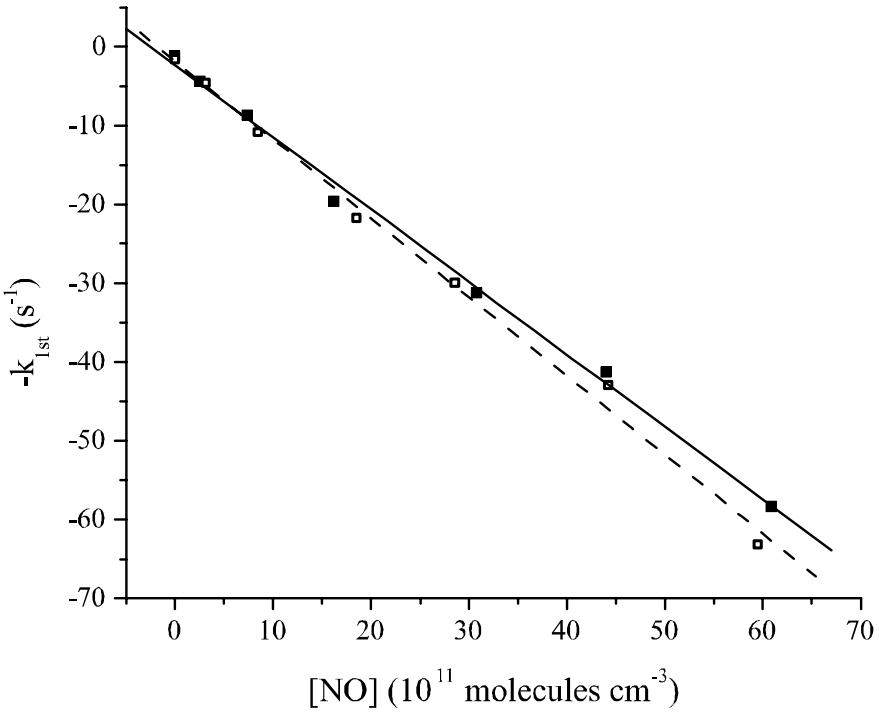

Figure 5-17: Plot of the pseudo-first order decay rates vs. NO concentration for the two OH scavengers. (■)-α-terpinene scavenger, (□)-isoprene scavenger.

within experimental error of each other. The error represents two standard deviations of the statistical error in the data and does not include systemic errors.

The experiments were repeated for a variety of temperatures to determine the temperature dependence of this reaction. For the temperature dependent studies, only α-terpinene was used as an OH scavenger. The results of the temperature studies are given in Table 5.4. An Arrhenius plot of the rate constants is given in Figure 5-18. The temperature dependence of the rate coefficient is small, however a linear least-squares fit to the data yields a temperature dependent rate expression of $k_{5.6}$ (T) = $(5.96^{+0.45}_{-0.42}) \times 10^{-12}$ $e^{((160\pm40)/T)}$ cm^3 molecule^{-1} s^{-1}. This expression yields a recommendation of $k_{5.6} = 1.02 \times 10^{-11}$ cm^3 molecule^{-1} s^{-1} at 298 K. This is almost 15% higher than the current recommendation by Atkinson of 9×10^{-12} cm^3 molecule^{-1}

T (K)[a]	P (Torr)[b]	Scavenger	$k_{5.6} \pm 2\sigma$ [c]
238	100	α-terpinene	$(1.16 \pm 1.21) \times 10^{-11}$
243	99.9	α-terpinene	$(1.17 \pm 1.21) \times 10^{-11}$
250	100.1	α-terpinene	$(1.10 \pm 0.23) \times 10^{-11}$
258	99.8	α-terpinene	$(1.08 \pm 0.21) \times 10^{-11}$
269	99.8	α-terpinene	$(1.09 \pm 0.19) \times 10^{-11}$
283	99.9	α-terpinene	$(1.05 \pm 0.22) \times 10^{-11}$
293	100.2	α-terpinene	$(9.95 \pm 0.19) \times 10^{-12}$
293	100	isoprene	$(1.05 \pm 0.20) \times 10^{-11}$
298	99.9	α-terpinene	$(1.03 \pm 0.18) \times 10^{-11}$
311	100.1	α-terpinene	$(9.79 \pm 0.17) \times 10^{-12}$

Table 5.4: Summary of the experimental conditions and rate constants measured for the $C_3H_6OHO_2$ + NO reaction. [a]Temperatures are ±1 K. [b]Pressures are ±1 Torr. [c]Rate constants are given in units of cm^3 $molecule^{-1}$ s^{-1}. The error represents the two standard deviation statistical error in the data and is not an estimate of systematic error.

s^{-1} [*Atkinson*, 1994]. This is the first direct measurement of the rate of a β-hydroxyalkylperoxy radical reaction with NO, so there are no other rates available for comparison. The recommendation of Atkinson is based on the measured values for small alkylperoxy radicals, so this value should supersede that recommendation for other hydroxyalkylperoxy radicals.

The Arrhenius parameters measured for this reaction can be compared to the recommendations for a number of peroxy radical-NO temperature dependent parameters. The Arrhenius parameter recommendations are available for CH_3O_2, $C_2H_5O_2$, $CH_3C(O)O_2$, and $CH_3C(O)CH_2O_2$ [*Tyndall et al.*, 2001] and are summarized in Table 5.5 along with the recommendations from this work. The values from this work are very reasonable when compared to other peroxy radical reactions. The activation energy is smaller than for the other peroxy radicals shown here, however again there are no β-hydroxyalkylperoxy radicals with which to compare the values from this work.

5.3.4 Conclusions

This is one of the few measurements of the temperature dependent rate of a multi-functional peroxy radical reaction with NO. These results should help our understanding of the effect of other functional groups on the reactions of peroxy radicals. The branching ratio of this reaction to form the stable peroxy nitrate ($RONO_2$) could also potentially be studied for this reaction. This is an important channel for this reaction in the atmosphere since it is a radical sink for both RO_2 and NO_x. This branching ratio for propene has been estimated in smog chamber studies to be 1.5% of the total reaction [*Shepson et al.*, 1985; *O'Brien et al.*, 1998], however a direct study would confirm these results. The individual reaction rates of the different isomers could be potentially studied with the triple quadrupole mass spectrometer recently acquired by this laboratory.

The peroxy radical corresponding to the isoprene-OH adducts and α-terpinene-OH adducts were also detected with O_2^- at m/e 117 and m/e 185 respectively, suggesting that the oxidation mechanisms of many important biogenic VOCs could be studied using this technique.

Molecule	**A**	**B**	**k** (298K)
	cm^3 $molecule^{-1}$ s^{-1}	K	cm^3 $molecule^{-1}$ s^{-1}
CH_3O_2	2.8×10^{-12}	300±100	7.7×10^{-12}
$C_2H_5O_2$	2.7×10^{-12}	350±50	8.9×10^{-12}
$CH_3C(O)O_2$	8.1×10^{-12}	270±100	2.0×10^{-11}
$CH_3C(O)CH_2O_2$	2.8×10^{-12}	300±200	8.0×10^{-12}
$C_3H_6OHO_2$	5.96×10^{-12}	160±40	1.02×10^{-11}

Table 5.5: Arrhenius parameters for the reactions of peroxy radicals with NO. The parameters given are for the equation $k(T) = Ae^{B/T}$.

5.4 Mass Balance Experiments

5.4.1 Introduction

The oxidation mechanism of propene in the presence of NO and O_2 yields formaldehyde and acetaldehyde regardless of the propene-OH isomer formed in the initial reaction of propene with OH (Figure 5-1). If a significant reaction channel leading to different products is not accounted for in the mechanism, then the aldehyde yields will be less than unity. The relationship between Δ[Propene] and Δ[Aldehyde] been measured by a number of laboratories [*Niki et al.*, 1978; *Vereecken et al.*, 1999]. Niki et al. measured a Δ[Propene] to Δ[Aldehyde] ratio of $\simeq$1 for both formaldehyde and acetaldehyde. More recently, Vereecken et al. also found these ratios to be equal to unity within experimental uncertainty.

This measurement was attempted to further determine the ability of the CIMS flow tube system in the elucidation of organic oxidation mechanisms and to validate the previous studies of this mechanism.

5.4.2 Experimental setup

The experimental setup used was similar to that used in the previous experiments. The OH was generated in the sidearm using the F + H_2O reaction (Section 5.3.2). The propene/oxygen mixture could either be injected in the rear of the flow tube or directly into the sidearm producing the peroxy radicals of interest. NO was introduced through the moveable injector.

The calibration samples of acetaldehyde and formaldehyde were introduced through the rear of the flow tube. Formaldehyde was prepared by heating a sample of paraformaldehyde (Aldrich 95%) under vacuum to approximately 150°C with a heat gun. Formaldehyde (b.p.

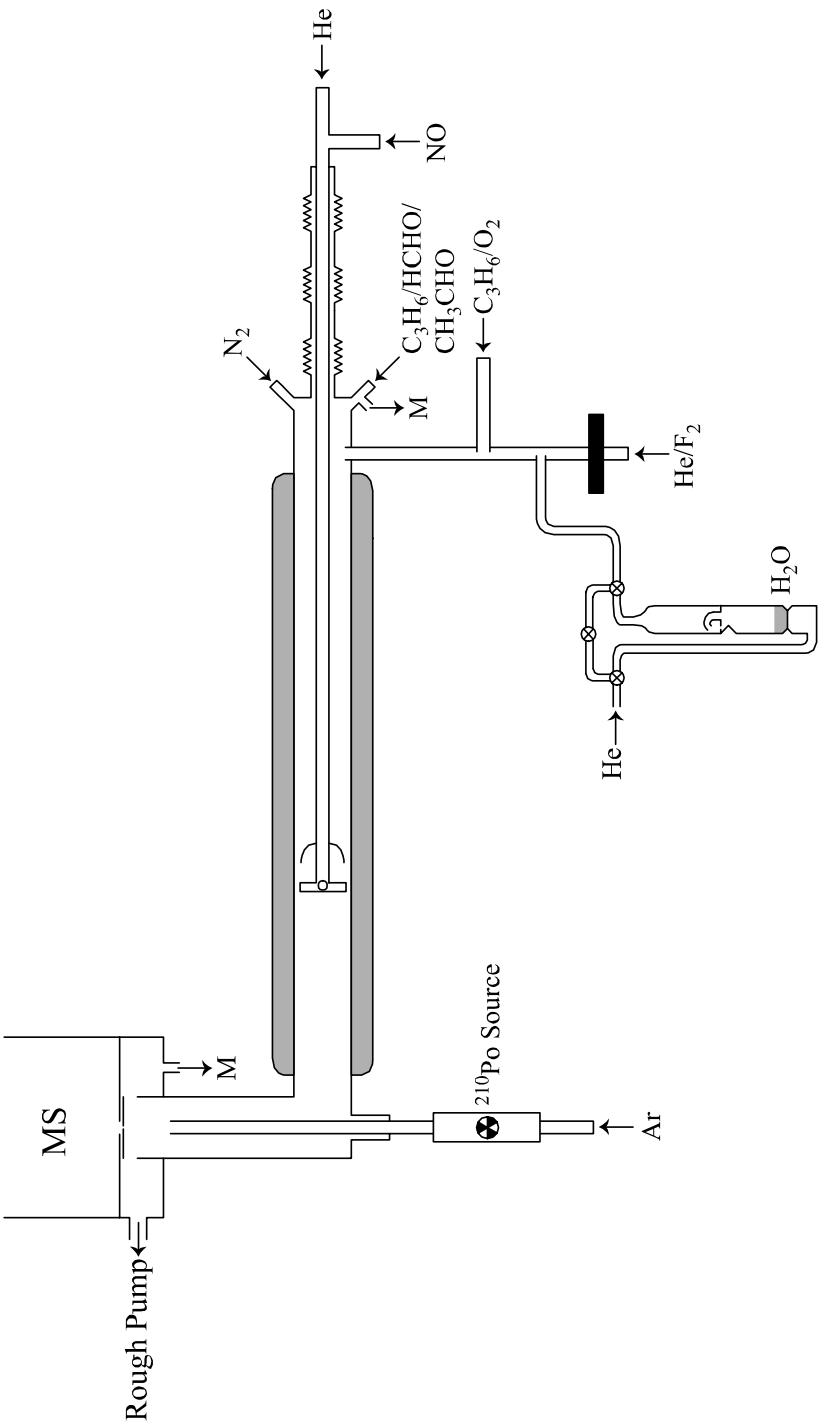

Figure 5-18: Experimental setup for the mass balance experiments.

-21°C) was liberated and collected in a cold finger at -80°C in a dry-ice/isopropanol bath. The formaldehyde sample was then pumped for approximately 5 minutes to remove any non-condensible impurities. A 0.05% mixture was made in a clean, dry 3 L pyrex bulb with UHP N_2. The sample was used within 2 days of preparation. The low concentration mixture in the bulb and the immediate use of the sample was necessary due to the formation of paraformaldehyde on the walls of the bulb. A 1% mixture of formaldehyde in N_2 had a white coating on the walls of the bulb within a few days. The acetaldehyde was drawn from a liquid sample (Aldrich 99.5%) (b.p. 21°C) and placed in a cold finger. The cold finger was cycled through several freeze-pump-thaw cycles at 77 K to remove any non-condensible gases. A 0.1% mixture was then prepared in a 3 L pyrex bulb with UHP N_2.

The OH concentration was increased to promote significant reaction with propene. The OH concentrations used were in the range of 1-5 $\times$ 10^{11} molecules cm^{-3}. The NO concentration used was also large (1×10^{13} molecules cm^{-3}) to promote conversion of the peroxy radicals formed to the corresponding alkoxy radicals.

The chemical ionization scheme used a combination of positive ion reagents. A 5.0 STP L min^{-1} flow of UHP Ar (BOC 99.998%) was passed through a molecular sieve trap at 77 K and then passed through the polonium ionization source. At 100 Torr, this produced almost equal amounts of the parent ions O_2^+ and $H_3O^+ \cdot (H_2O)_n$. In this way, the species of interest could be simultaneously measured via the reactions:

$$O_2^+ + C_3H_6 \longrightarrow C_3H_6^+ + O_2 \tag{5.22}$$

$$H_3O^+ \cdot (H_2O)_n + CH_3CHO \longrightarrow CH_3CHOH^+ \cdot (H_2O)_{n-1} + H_2O \tag{5.23}$$

$$H_3O^+ \cdot (H_2O)_n + HCHO \longrightarrow HCHOH^+ \cdot (H_2O)_{n-1} + H_2O \tag{5.24}$$

The reaction setup is shown in Figure 5-18.

5.4.3 Experiments and results

The propene signal and the corresponding formaldehyde and acetaldehyde signal were measured with the OH source on and off for various initial propene concentrations. The difference in the propene signal with the OH discharge on and off corresponded to a mass of propene reacted. The difference in the aldehyde signals corresponded to a mass of aldehyde produced. The signal changes observed were calibrated with the sample bulbs described in the previous section.

The difficulties with these experiments were numerous. The initial propene concentrations used were low (10^{10}-10^{11} molecules cm^{-3}) so that changes in the signal could be detected, however at these low concentrations, the reaction with OH is slow. The OH concentration was increased to compensate, however, the OH then begins to react with the aldehydes and with itself to form O atoms which react with propene. There is also the problem of short reaction times. The reaction time was varied between 50-100 ms, but at these short times, there are significant concentrations of intermediate species such as the peroxy radicals in the flow tube. This decreases the apparent aldehyde yield since carbon is sequestered in the radical intermediate species. The O_2 and NO concentrations can be increased to quickly convert the intermediate species to the aldehydes, however as described in the previous section, this regenerates OH more quickly and the OH re-enters the propene chemistry cycle. Organic OH scavengers such as isoprene also produce formaldehyde as a product of their oxidation mechanisms, so a scavenger is not the solution to this problem.

Measured acetaldehyde and formaldehyde yields ranged from 25% to 80% depending on the conditions in the flow tube. Results from a sample experiment are given in Figure 5-19. The

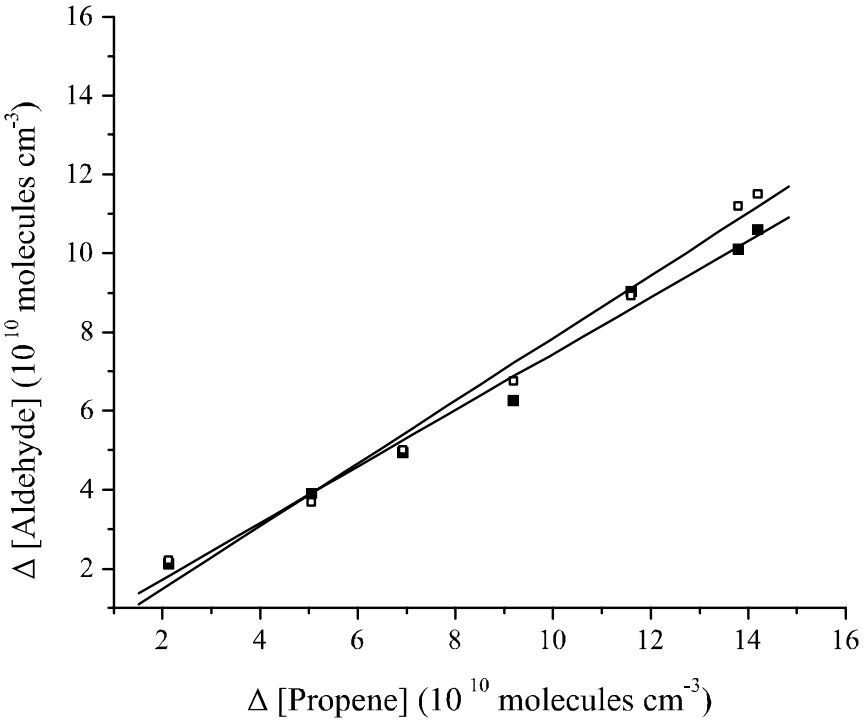

Figure 5-19: Mass balance experimental results showing the rise in aldehyde concentration vs. the loss of propene. (□)-acetaldehyde, (■)-formaldehyde

yield for both aldehydes in this experiment was approximately 75%.

5.4.4 Conclusions

This experimental technique does not appear to be well suited to product studies. The reaction time is much shorter than in the smog chambers which have been used to successfully perform these experiments. The changes in the propene signal and aldehyde signals were small and a significant percent of the carbon was found in the intermediate species and was not detected as a product. A slow flow reactor or static chamber coupled to a chemical ionization mass spectrometer must be developed to successfully perform these experiments and determine product yields.

5.5 Conclusions and Future Work

The CIMS technique has been shown to be successful in measuring the kinetics of the elementary steps in the atmospheric oxidation mechanisms of alkenes. This technique holds great promise for the elucidation of the oxidation mechanisms of important biogenic VOCs such as isoprene or α-pinene. It has been shown that even large cyclic radicals produced in the oxidation of α-terpinene can be detected with this technique.

The reactions of the peroxy radicals formed in the oxidation of propene will undergo reaction with HO_2 in a low NO_x environment. This reaction could potentially be studied using this technique as well as the branching ratio of the RO_2 + NO reaction to form $RONO_2$. A different reactor would have to be developed to perform detailed product studies of these mechanisms, however.

References for Chapter 5

Atkinson, R. and J.N. Pitts, Jr., Rate constants for the reaction of OH radicals with propylene and the butenes over the temperature range 297-425 K, *J. Chem. Phys.*, **63**, 3591-3595, 1975.

Atkinson, R., Gas-phase reactions of the hydroxyl radical, *Chemical Reviews*, **85**, 121-201, 1985.

Atkinson, R., Gas-phase tropospheric chemistry of organic compounds, *Journal of Physical and Chemical Reference Data Monograph No. 2*, 1994.

Atkinson, R., D.L. Baulch, R.A. Cox, R.F. Hampson, J.A. Kerr, M.J. Rossi, and J. Troe, Evaluated kinetic and photochemical data for atmospheric chemistry: Supplement VI-IUPAC subcommittee on gas kinetic data evaluation for atmospheric chemistry, *Journal of Physical and Chemical Reference Data*, **26**, 1329-1499, 1994.

Becker, K.H., H. Geiger, and P. Wiesen, Kinetic study of the OH radical chain in the reaction system OH+C_2H_4+NO+air, *Chem. Phys. Lett.*, **184**, 256-261, 1991.

Carter, W.P.L., Development of ozone reactivity scales for volatile organic compounds, EPA-600/3-91/050, 1991.

DeMore, W.B., S.P. Sander, C.J. Howard, A.R. Ravishankara, D.M. Golden, C.E. Kolb, R.F. Hampson, M.J. Kurylo, and M.J. Molina, *Chemical Kinetics and Photochemical Data for Use in Stratospheric Modeling*, JPL Publication 97-4, Jet Propulsion Laboratory, Pasadena, CA, 1997.

Eberhard, J, P.W. Villalta, and C.J. Howard, Reaction of Isopropyl peroxy radicals with NO over the temperature range 201-401 K, *J. Phys. Chem.,* **100**, 993-997, 1996.

Finlayson-Pitts, B.J. and J.N. Pitts, Jr., *Chemistry of the Upper and Lower Atmosphere*, Academic Press, San Diego, 2000, pp. 17-19, 225-227.

Kavouras, I.G., N. Mihalopoulos, and E.G. Stephanou, Secondary organic aerosol formation vs primary organic aerosol emission: in situ evidence for the chemical coupling between monoterpene acidic photooxidation products and new particle formation over forests, *Environ. Sci. Technol.*, **33**, 1028-1037, 1999.

Miyoshi, A., H. Matsui, and N. Washida, Reactions of hydroxyethyl radicals with oxygen and nitric oxide, *Chem. Phys. Lett.*, **160**, 291-294, 1989.

Miyoshi, A., H. Matsui, and N. Washida, Rates of reaction of hydroxyalkyl radicals with molecular oxygen, *J. Phys. Chem.*, **94**, 3016-3019, 1990.

Niki, H., P.D. Maker, C.M. Savage, and L.P. Breitenbach, Mechanism for hydroxyl radical

initiated oxidation of olefin-nitric oxide mixtures in parts per million concentrations, *J. Phys. Chem.*, **82**, 135-137, 1978.

Nip, W.S. and G. Paraskevopoulos, Rates of OH radical reactions. VI. Reactions with C_3H_6, 1-C_4H_8 and 1-C_5H_{10} at 297 K, *J. Chem. Phys.*, **71**, 2170-2174, 1979.

O'Brien, J.M., E. Czuba, D.R. Hastie, J.S. Francisco, and P.B. Shepson, Determination of the hydroxy nitrate yields from the reaction of C_2-C_6 alkenes with OH in the presence of NO, *J. Phys. Chem. A.,* **102**, 8903-8908, 1998.

Plassdulmer, C. R. Koppmann, M. Ratte, and J. Rudolph, Light nonmethane hydrocarbons in seawater, *Global Biogeochemical Cycles*, **9**, 79-100, 1995.

Ravishankara, A.R., S. Wagner, S. Fischer, G. Smith, R. Schiff, R.T. Watson, G. Tesi, and D.D. Davis, A kinetics study of the reactions of OH with several aromatic and olefinic compounds, *Int. J. Chem. Kinet.*, **10**, 783-804, 1978.

Schmidt, V., G.Y. Zhu, K.H. Becker, and E.H. Fink, Study of OH reactions at high pressures by excimer laser photolysis - dye laser fluorescence, *Ber. Bunsenges. Phys. Chem.*, **89**, 321-322, 1985.

Shepson, P.B., E.O. Edney, T.E. Kleindienst, J.H. Pittman, G.R. Namle, and L.T. Cupitt, The production of organic nitrates from hydroxyl and nitrate radical reaction with propylene, *Environ. Sci. Technol.*, **19**, 849-853, 1985.

Smith, G.D., *Experimental Studies of Photolytic Reactions of Atmospheric Significance Using Chemical Ionization Mass Spectrometry*, Ph.D. Thesis, Massachusetts Institute of Technology, 2000.

Stevens, P., D. L'Esperance, B. Chuong, and G. Martin, Measurements of the kinetics of the OH-initiated oxidation of isoprene: radical propagation in the OH +isoprene+O_2+ NO reaction system, *Int. J. Chem. Kinet.*, **31**, 637-643, 1999.

Tully, F.P. and J.E.M. Goldsmith, Kinetic study of the hydroxyl radical-propene reaction, *Chem. Phys. Lett.*, **116**, 345-352, 1989.

Tyndall, G.S., R.A. Cox, C. Granier, R. Lesclaux, G.K. Moortgat, M.J. Pilling, A.R. Ravishankara, and T.J. Wallington, Atmospheric chemistry of small organic peroxy radicals, *J. Geophys. Res.*, **106**, 12157-12182, 2001.

Vereecken, L., J. Peeters, J.J. Orlando, G.S. Tyndall, and C. Ferronato, Decomposition of β-hydroxypropoxy radicals in the OH-initiated oxidation of propene. A theoretical and experimental study, *J. Phys. Chem. A.,* **103**, 4693-4702, 1999.

Yaws, C.L., *Handbook of Vapor Pressure Volume 3: C_8 to C_{28} Compounds*, Gulf Publishing Co., Houston, TX, 1994.

Zellner, R., and K. Lorenz, Laser photolysis/resonance fluorescence study of the rate constants for the reactions of OH radicals with C_2H_4 and C_3H_6, *J. Phys. Chem.,* **88**, 984-989, 1984.

Chapter 6

Isoprene Oxidation Reactions

6.1 Introduction

Isoprene is one of the most important VOCs in the atmosphere. Global emission rates of isoprene are estimated to be equal to all other VOC emission rates combined. The estimated total global emission rate of isoprene is 500 Tg yr^{-1} [*Finlayson-Pitts & Pitts*, 2001]. The high emission rates coupled with the rapid reaction of isoprene with OH and O_3 emphasize the importance of isoprene chemistry in the troposphere. The reactions of isoprene with OH and O_3 are similar to those of other alkenes (Chapter 5):

$$Isoprene + OH \longrightarrow Isoprene\text{-}OH \tag{6.1}$$

$$Isoprene + O_3 \longrightarrow Products \tag{6.2}$$

with $k_{6.1} = 1.01 \times 10^{-10}$ cm^3 $molecule^{-1}$ s^{-1} and $k_{6.2} = 1.28 \times 10^{-17}$ cm^3 $molecule^{-1}$ s^{-1} [*Atkinson*, 1994].

Isoprene oxidation reactions have been studied both experimentally and theoretically [*Zhang et al.*, 2001; *Zhang et al.*, 2000; *Lei et al.*, 2000], however, like most hydrocarbons, many of the intermediate steps have not been studied. The oxidation mechanism of isoprene is complicated by the fact that isoprene is a non-symmetrical diene with conjugated double bonds. The OH radical has four unique sites of addition to the isoprene molecule. The OH adducts then undergo addition of O_2 to form the corresponding peroxy radicals. For the terminal OH addition products, however, resonance structures allow for two sites of O_2 addition for each OH-isoprene adduct. This results in a total of 6 peroxy radicals formed in the oxidation mechanism of isoprene, 2 δ-hydroxyperoxy radicals and 4 β-hydroxy peroxy radicals. These first two steps in the mechanism are shown in Figure 6-1. The reaction mechanism becomes too complex after this point to be included in Figure 6-1.

An important reaction in this mechanism is the reaction of the peroxy radical with NO.

$$C_5H_8OHO_2 + NO \longrightarrow C_5H_8(OH)O + NO_2 \tag{6.3}$$

The emissions of isoprene are predominantly centered in suburban and rural areas where vegetation is abundant. The NO_x sources are generally low in these areas compared to urban areas, however levels of ambient pollutants such as NO_x and O_3 appear to be rising in rural areas due to increased pollution levels on a global scale [*Finlayson-Pitts & Pitts*, 2001]. If the NO_x concentration is low near the source of the isoprene then the reaction of these peroxy radicals with HO_2 may compete with the reaction of these radicals with NO. It is important, therefore, to know the rates of these reactions.

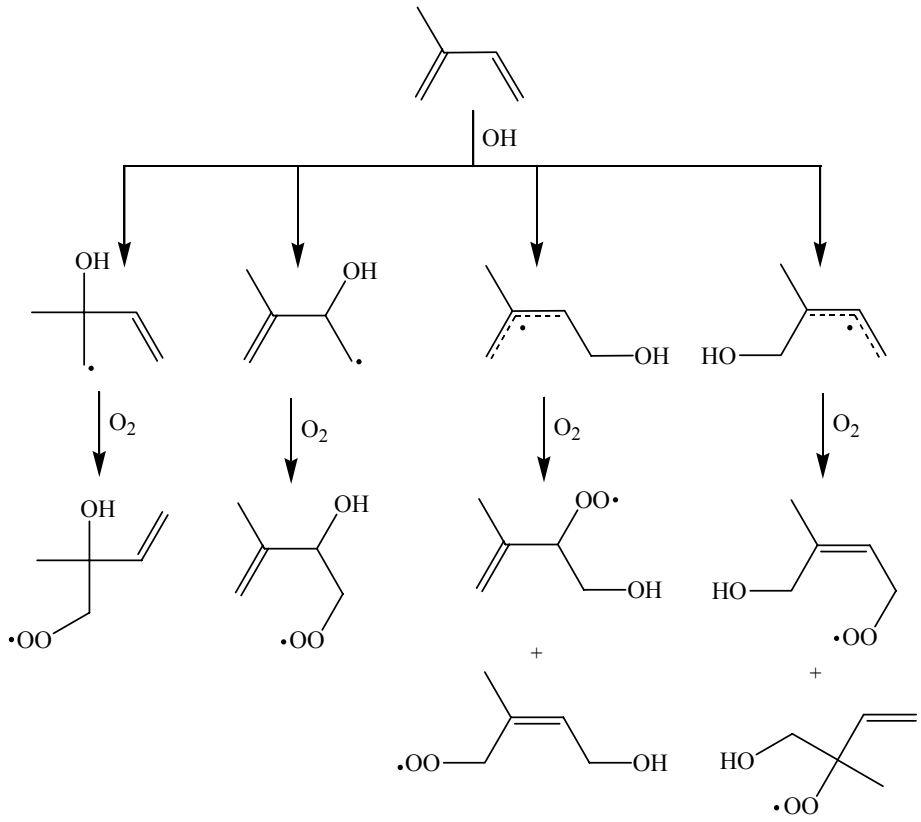

Figure 6-1: OH initiated oxidation mechanism of isoprene showing the 4 OH adducts formed via the isoprene-OH reaction and the 6 peroxy radical isomers formed via the addition of O_2.

6.2 Reaction of NO With the Peroxy Radicals Formed in the OH-Initiated Oxidation of Isoprene

6.2.1 Introduction

The same difficulties are encountered in the study of this reaction as were encountered in the reaction of propene (Chapter 5). The OH propagation chain is fast in the presence of NO and O_2 [*Stevens et al.*, 1999]. This measurement of this reaction is further complicated by the presence of 6 peroxy radical isomers, some of which have very different structures and potential

chemical reactivities. There is a significant probability that the observed pseudo-first order decays in the presence of NO will be multi-exponential due to the fact that the signal decay is a sum of the individual decays of the 6 isomers.

The OH propagation problem was solved in the same manner as in Chapter 5 for the reaction of propene. An OH scavenger was introduced in the flow tube so that the OH radicals would preferentially react with the scavenger as opposed to isoprene. This would prevent the regeneration of the peroxy radicals in the flow tube.

6.2.2 Experimental setup

The experimental setup was very similar to that used in Section 5.3.2. The isoprene peroxy radicals were produced in the sidearm via the reaction of OH with a mixture of isoprene and O_2. The OH radical source and flow conditions in the sidearm were identical to those used in Section 5.3.2. The propene mixture was substituted with a 1.5% mixture of isoprene (Aldrich 99%) in UHP N_2 in a 3 L passivated pyrex bulb.

The OH scavenger used in this experiment was α-terpinene. A 30 STP cm^3 min^{-1} flow of UHP N_2 was passed through a fritted bubbler containing α-terpinene at 25°C. This flow then entered through the rear of the flow tube. This high flow was needed in order to introduce sufficient amounts of the scavenger into the flow tube to compete with the OH-isoprene reaction. No other scavenger was used due to the difficulty in finding a scavenger that would compete with isoprene, however as shown in the propene experiments (Chapter 5), the scavenger does not appear to influence the flow tube chemistry.

The chemical ionization scheme was identical to that used previously (Section 5.3.2). O_2^-

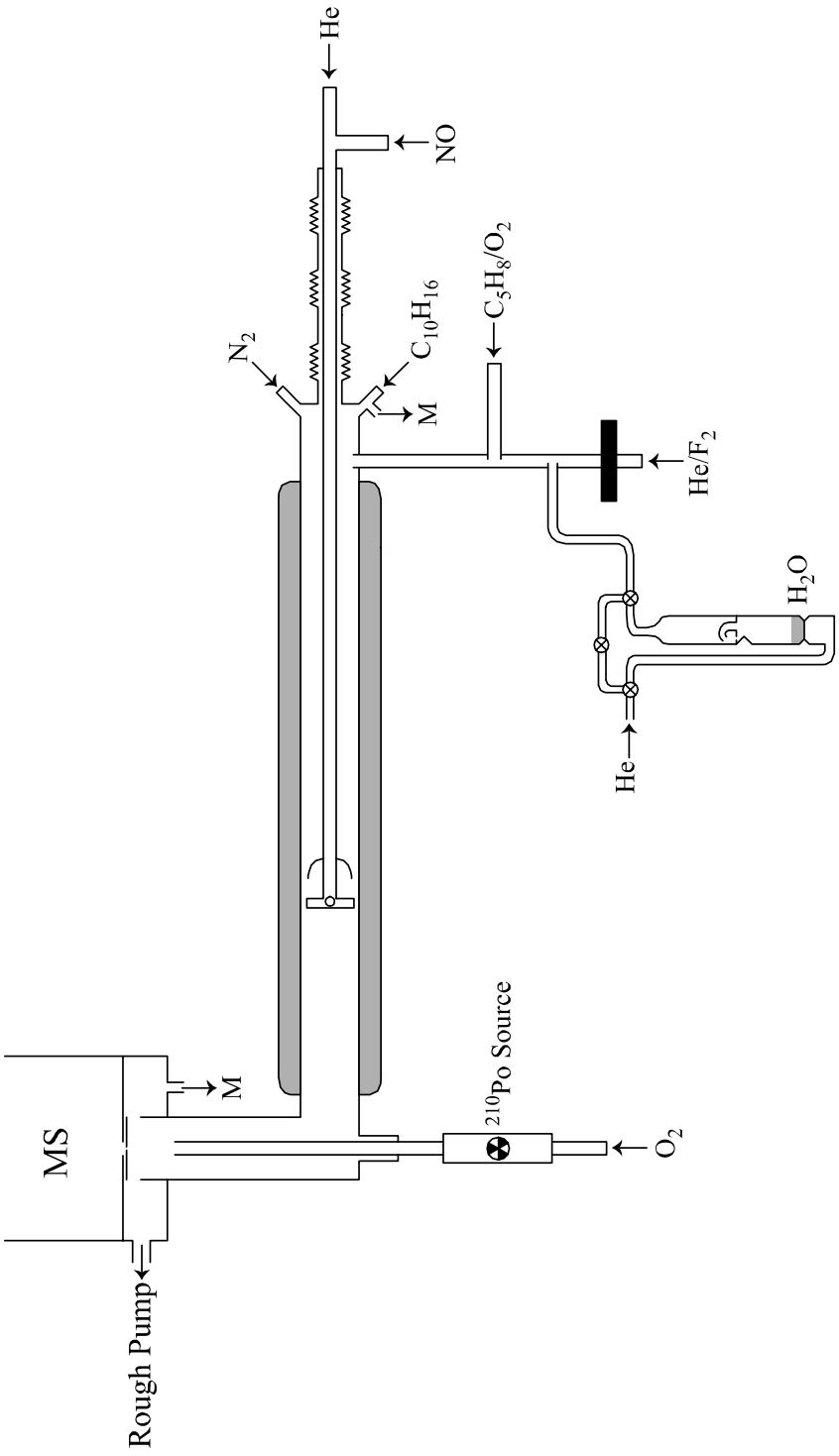

Figure 6-2: Experimental setup for the reaction of the isoprene peroxy radicals with NO.

was used to detect the peroxy radicals formed in the flow tube.

$$O_2^- + C_5H_8OHO_2 \longrightarrow C_5H_8OHO_2^- + O_2 \quad (6.4)$$

$$O_2^- + C_{10}H_{16}OHO_2 \longrightarrow C_{10}H_{16}OHO_2^- + O_2 \quad (6.5)$$

The peroxy radicals formed from the reactions of isoprene and α-terpinene were detected at m/e 117 and m/e 185, respectively. A schematic of the experimental setup is shown in Figure 6-2.

6.2.3 Room temperature experiments and discussion

The pseudo-first order decays of the isoprene peroxy radicals as a function of time were measured for a variety of NO concentrations at 298 K. The OH loss rate with respect to α-terpinene was a factor of 50 higher than the OH loss rate with respect to isoprene for all the measurements. The pseudo-first order decays are shown in Figure 6-3. The decays appear to be very linear on the semi-log plot within the experimental scatter suggesting that the reactivities of the 6 isomers are very similar with respect to NO. This was not surprising in the case of propene where the 2 β-hydroxypropylperoxy radicals had very similar structures, however in the case of isoprene the isomers are more dissimilar. The proximity of the hydroxyl group to the peroxy group on the carbon chain may not have a significant effect on the reaction rate with NO. It has been shown that the reaction of NO with highly substituted peroxy radicals such as $(CH_3)_3CO_2$ is slower than the rate for terminal peroxy radicals [*Peeters et al.*, 1992]. The reaction rate of the t-butylperoxy radical with NO is 4×10^{-12} cm^3 molecule^{-1} s^{-1} compared to 8.9×10^{-12} cm^3 molecule^{-1} s^{-1} for the ethylperoxy radical [*Atkinson*, 1994]. The isoprene peroxy radical

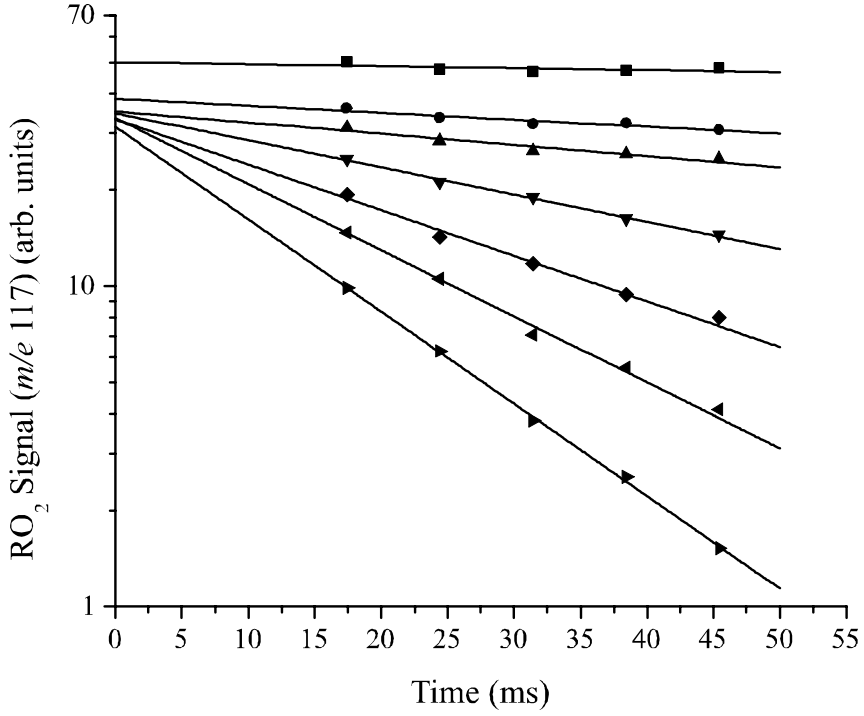

Figure 6-3: Pseudo-first order decays of the β- and δ-hydroxyperoxy radicals formed from the OH-initiated oxidation of isoprene in the presence of NO. NO concentrations range from (•) 2.6×10^{11} molecules cm^{-3} to (▶) 6.0×10^{12} molecules cm^{-3}. Lines represent a non-linear least-squares fit to the data using a single exponential decay ($y = ae^{bx}$).

isomers include both terminal and highly substituted peroxy radicals, however this also does not seem to play a role in their reaction rates with NO.

Another possibility is that the O_2^- detection scheme is only sensitive to a select number of the 6 isomers. The observed decays would only be a measurement of the decays of those isomers and would not be sensitive to the decay rates of the other isomers. This seems unlikely due to the apparent versatility of O_2^- in detecting organic peroxy radicals.

A plot of the pseudo-first order decay rates from Figure 6-3 as a function of NO concentration is shown in Figure 6-4. The second order rate coefficient ($k_{6.3} = (1.09 \pm 0.17) \times 10^{-11}$ cm^3 molecule^{-1} s^{-1}) is very similar to the rate determined for the propene peroxy radicals. This

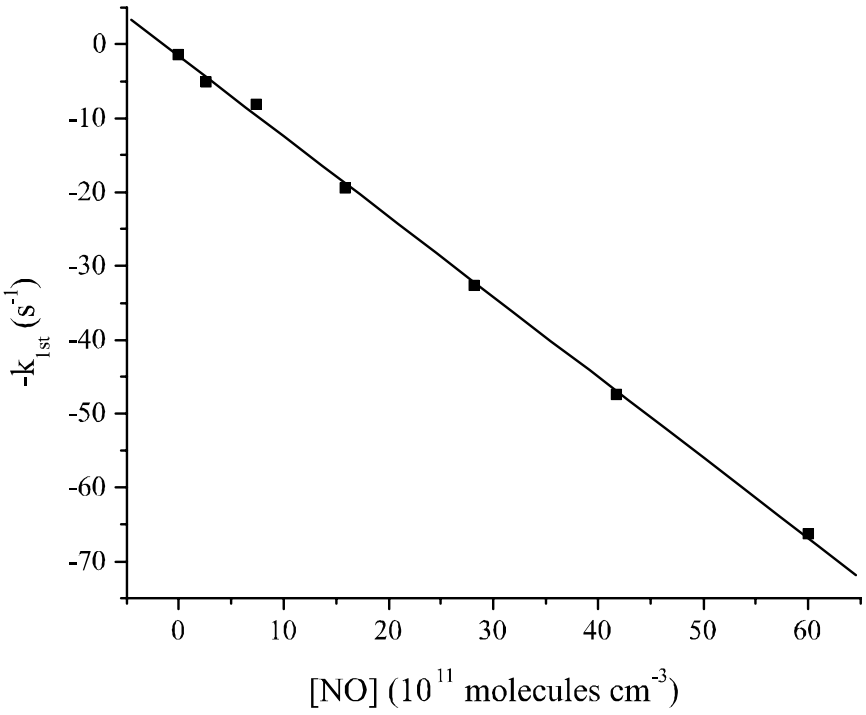

Figure 6-4: Pseudo-first order decay rates, k_{1st}, vs. NO concentration. The line is a linear least-squares fit to the data and the slope yields the second order rate coefficient of 1.09 $\times$ 10^{-11} cm^3 molecule^{-1} s^{-1} at 298 K.

value for $k_{6.3}$ is similar to an unpublished rate for this reaction determined through indirect methods by Renyi Zhang [*Zhang*, 2001].

The reaction rates of hydroxyalkylperoxy radicals with NO appear to be faster than the current recommendation of Atkinson by 10-20%. These reactions have only been measured for two hydrocarbons, propene and isoprene, so any extrapolation beyond C_5 hydrocarbons is difficult.

This work is further evidence that this technique is well suited to the measurement of the kinetics of the intermediate steps in the oxidation mechanism of VOCs.

6.2.4 Future work

The temperature dependence of $k_{6.3}$ could be measured to determine the Arrhenius parameters for this reaction for comparison to other RO_2 + NO parameters. The reaction of these peroxy radicals with HO_2 could also be examined as a function of temperature since no data is available for this reaction either. The branching ratio of the reaction of these peroxy radicals with NO could also be examined, although the large number of isomers makes this measurement difficult. The organic nitrates would also have to be synthesized.

The most exciting possibility is the use of collision-induced-dissociation (CID) of the peroxy radical ions in the triple quadrupole system being developed in the lab. The peroxy radical ions would be selected and then fragmented in the CID chamber. The daughter ions would then be analyzed in the third quadrupole. Each isomer would theoretically have a unique daughter ion fingerprint and could be detected uniquely. A wealth of information could be available using this technique.

References for Chapter 6

Atkinson, R., Gas-phase tropospheric chemistry of organic compounds, *Journal of Physical and Chemical Reference Data Monograph No. 2*, 1994.

Finlayson-Pitts, B.J. and J.N. Pitts, Jr., *Chemistry of the Upper and Lower Atmosphere*, Academic Press, San Diego, 2000, pp. 225-227, 780.

Lei, W.F., A. Derecskei-Kovacs, and R.Y. Zhang, Ab initio study of OH addition reaction to isoprene, *J. Chem. Phys.*, **113**, 5354-5360, 2000.

Peeters, J., J. Vertommen, and I. Langhans, Rate constants of the reactions of CF_3O_2, i-$C_3H_7O_2$ and t-$C_4H_9O_2$ with NO, *Ber. Bunsenges. Phys. Chem.*, **96**, 431-426, 1992.

Stevens, P., D. L'Esperance, B. Chuong, and G. Martin, Measurements of the kinetics of the OH-initiated oxidation of isoprene: radical propagation in the OH +isoprene+O_2+ NO reaction system, *Int. J. Chem. Kinet.*, **31**, 637-643, 1999.

Zhang, D., R.Y. Zhang, C. Church, and S.W. North, Experimental study of hydroxyalkyl peroxy radicals from OH-initiated reactions of isoprene, *Chem. Phys. Lett.*, **343**, 49-54, 2001.

Zhang, R.Y., I. Suh, W. Lei, A.D. Clinkenbeard, and S.W. North, Kinetic studies of OH-initiated reactions of isoprene, *J. Geophys. Res.*, **105**, 24627-24635, 2000.